Analysis of Iron Precursor Assisted Emission Reduction in Counterflow Methane Diffusion Flame

by

Abhishek Raj

A thesis

presented to the University of Waterloo

in fulfillment of the

thesis requirement for the degree of

Doctor of Philosophy

in

Mechanical and Mechatronics Engineering

Waterloo, Ontario, Canada, 2017

© Abhishek Raj 2017

Examination Committee Membership

The following served on the Examining Committee for this thesis. The decision of the Examining Committee is by majority vote.

External Examiner	Dr. Fengshan Liu Senior Research Officer, National Research Council, Canada
Supervisor(s)	Dr. John Wen Associate Professor, Department of Mechanical and Mechatronics Engineering, University of Waterloo
Supervisor(s)	Dr. Eric Croiset Professor, Department of Chemical Engineering, University of Waterloo
Internal Member	Dr. Zhongchao Tan Professor, Department of Mechanical and Mechatronics Engineering, University of Waterloo
Internal Member	Dr. Xianguo Li Professor, Department of Mechanical and Mechatronics Engineering, University of Waterloo
Internal-external Member	Dr. William Anderson Professor, Department of Chemical Engineering, University of Waterloo

Author's Declaration

This thesis consists of material all of which I authored or co-authored: see Statement of Contributions included in the thesis. This is a true copy of the thesis, including any required final revisions, as accepted by my examiners.

I understand that my thesis may be made electronically available to the public.

Statement of contributions

This dissertation is partially the product of collaborative research and co-authored publication as follows:

- **Chapter 3** as Abhishek Raj, Kang Pan, Huixiu Qi, Henry Zhu, John Z.Wen and Eric Croiset. Effects of an iron pentacarbonyl additive on counterflow natural gas and ethanol flames. Energy & Fuels, vol. 29, no. 8, pp. 5361-5371.

  I, Abhishek Raj, carried out the design of the experimental setup, followed by the experimental measurements and their analysis. Kang Pan assisted in the calibration of Gas Chromatographer and in developing the experimental methodology. Huixiu Qi assisted in the calibration of FT-IR spectroscope and in measuring NO. Henry Zhu assisted in developing the experimental setup. Dr. John Wen and Dr. Eric Croiset were my research supervisors.

Abstract

Addition of metallic precursors to flames draws interest due to their potential ability to catalyze hydrocarbon combustion by means of supplemental gas phase and surface reactions**.** A counterflow flame burner is utilized to spatially characterize and analyze the emissions from iron pentacarbonyl ($Fe(CO)_5$) borne methane and ethanol combustion. Samples of the flue gases are obtained from these laminar and planar flames and are quantified using gas chromatography (GC) and Fourier-transform infra-red (FT-IR) spectroscopy, while solid particles are examined through x-ray diffraction (XRD). Measurements from ethanol and methane flames are compared and analyzed, in order to investigate the role of iron species derived from iron pentacarbonyl.

Experimental data demonstrate a significant influence of the additive on combustion emissions, such as NO and soot precursors, in both flames. The addition of iron pentacarbonyl is found to be more effective in restricting soot precursors in methane flames (upto 90%) as compared to ethanol flames (90% in C_2H_2 while 10% in C_2H_6). The decline in NO is about 20%-30% under both the cases. An enhanced production of acetaldehyde in the ethanol flame is believed to result in changes of the emission profiles.

This is followed by the numerical analysis of the previous experiments to determine the concentration, distribution and reaction rates of iron species, not measured in the experiments. The Computational Fluid Dynamics (CFD) model comprises of i) the burner geometry with a suitable mesh size; ii) governing equations addressing the conservation of mass, momentum , energy, species and; iii) reaction mechanisms governing the methane combustion (GRI 3.0), iron pentacarbonyl decomposition, iron clustering and iron oxides and hydroxide formation. The model is verified through literature data and compared against the experimental results. Sensitivity analysis is carried out to understand the influence of input parameters, such as the iron pentacarbonyl concentration and the fuel fraction on flame profile. The simulation results demonstrate a proportional decline in most C_2 and NO species with increasing precursor concentration. The emission decline is found to demonstrate an initial increase with increasing fuel fraction, but is reversed beyond a certain value.

As the heterogeneous catalysis processes, occurring on the surface of in-flame synthesized particles, also contribute to emission reduction, the particle evolution process, which governs the particle size and consequently the available specific surface area for catalysis, needs further exploration. Using counterflow burner configuration effectively simplifies the complex underlying physics behind the particle evolution process and provides ease of sampling. The last component of this thesis analyzes the particle evolution processes in a counterflow iron pentacarbonyl assisted methane diffusion flame. This is achieved by developing the experimental methodology for particle sampling and by analyzing the particle sampling results, with and without the iron precursor. Particles are sampled from various axial and radial locations of the flame by means of an orifice and are analyzed for the geometric mean particle diameter, mean particle concentration and the particle size distribution using a GRIMM Scanning Mobility Particle Scanner (SMPS). Different sampling orifice diameters are utilized in order to explore any particle loss during the sampling process. The results highlight various regimes of particle evolution: inception, surface growth and agglomeration to be dominant at various locations within the flame. The addition of iron precursor is found to result in an enhanced particle concentration but effectively reduces the mean particle size indicating enhanced presence of smaller particles.

Acknowledgement

I would like to thank the Almighty for rewarding me with this opporunity to carry out my doctoral studies at University of Waterloo, infusing me with focused determination, dexterity and skills to succesfully undertake this venture and keeping me and my family in His benevolent care.

My sincerest gratitude to Dr. John Wen and Dr. Eric Croiset for providing me with this wonderful opportunity to work on this project with them and their guidance and support during the course of this program.

A special thanks is in order for Dr. Zhongchao Tan for allowing me to access to the Scanning Mobility Particle Scanning device for my research purposes as well as for his time and effort to be an examiner for this thesis. I would also like to express my gratitude to Dr. Fengshan Liu, Dr. William Anderson and Dr. Xianguo Li for their time and effort to be the examiners of this thesis.

I would also like to thanks Jason Benninger for the technical support and guidance and acknowledge Connect Canada and BioFuelNet Canada for their financial support and contribution towards my reserch project.

Words are insufficient to express my indebtness to my parents and my sister for being the wind under my wings and for their love, encouragement, care and support through all the thick and thin times. I would always cherish the moments spent in the lab with my colleagues and friends Sanam Atahin, Dong Zhu, Sannan Toor, Florin Saceleanu, Hongtao Sui, Kang Pan and Huixiu Qi. You people have really helped in making it possible.

Last but not in anyways the least, I owe a lot to my wife for her love, support and amazing depth of patience during this period.

Dedication

My parents, my sister, my wife

"..the wind beneath my wings"

&

The eternal memory of my beloved grandfather

Table of Contents

List of Figures

List of Tables

List of Abbreviations

Abbreviation	Explanation
IC	Internal Combustion
GRI	Gas research Institute
PAH	Polycyclic Aromatic Hydrocarbons
DFT	Density Functional Theory
QRRK method	Quantum Rice-Ramsperger-Kassel method
LII	Laser Induced Incandescence
XRD	X-Ray Diffraction
PIMS	Photo Ionization Mass Spectroscopy
SEM	Scanning Electron Microscopy
TEM	Tunneling Electron Microscopy
SMPS	Scanning Mobility Particle Sizer
GC	Gas Chromatographer
FT-IR	Fourier Transform-Infrared Spectroscopy
MFC	Mass Flow Controllers
I/O D	Internal/Outer Diameter
DMA	Differential Mobility Analyzer
HACA	Hydrogen-Addition-Carbon-Abstraction
EDAX	Energy Dispersive Analysis of X-Rays

SSA	Specific Surface Area
XRD	X-Ray Diffraction

Chapter 1

Introduction

1.1 Problem Statement

Addressing air pollutant emissions has always been an integral component of the regulations governing the development of automobiles and power plants. These emissions include unburnt particles of carbon known as soot as well as Nitric Oxide (NO). Soot is known to extend its detrimental impact on human health by aggravating pulmonary and cardiac problems [1], as well as has a significant global warming potential [2] , while NO has been responsible for the depletion of the ozone layer [3] and plays a major role in the formation of photochemical smog and acid rain [4]. Emission regulations have consistently demonstrated a trend towards increasing stringency, which is expected to continue in the near future. Oil and natural gas are currently the primary sources of energy contributing to around 60% of the global energy consumption while renewable sources, nuclear and hydro together contribute less than 18% to the total consumption [5]. These renewable sources also include biofuels which are produced by biological sources through the process of carbon fixation like bio-ethanol. Thus, the hydrocarbons (both conventional and liquid biofuels) would continue to dominate the primary energy mix in the near future and consequently greater efforts directed towards restricting carbon intensity as well as emissions of hydrocarbons are required. Since cheap and consistent options on the supply side remain limited, it is the

demand side that needs to be effectively managed so as to curtail emissions as well as the energy requirements. Industrial, residential and transportation sector remain highly energy intensive and lead to the generation of significant quantities of unwanted by-products. Consequently, these sectors remain the key foci of all efforts towards developing more energy efficient technologies and treatment techniques of the emission products.

Catalysis process forms the bedrock of the global chemical industry by being incorporated within more than 75% of the chemical processes [6]. It greatly reduces the energy requirement for the initiation of many chemical processes while also enhancing selectivity towards the main product. Heterogeneous catalysis, in which the catalyst exists (generally solid) in a different phase than the reactants and products [6], is commonly utilized for after-treatment of the exhaust at the post-combustion stage. This treatment of flue gases, which is mainly manifested in the form of catalytic convertors, diesel particulate filters etc., makes the process cost inhibitive as these devices are required to be coated with expensive catalytic material. Moreover, the synthesis of catalysts itself involves energy consumption. A highly energy-intensive catalyst synthesis process might offset the advantage of energy savings due to catalysts. Hence, the focus is directed towards developing catalysts in an energy efficient and easy-to-scale technique capable of achieving results on par with the conventional processes.

Using metallic precursor as fuel additive provides a unique opportunity to leverage the low-cost, energy efficient aerosol flame synthesis process [7] to achieve cleaner combustion as a result of reduced emissions over flame produced catalyst particles. A key drawback in the use of this method is the increase in the metal concentration in the exhaust, which constitutes a health hazard and induces a constraint in the form of requirement of some kind of filter for this method, although it can be used without any filter as well at the cost of environment. Using a diesel particulate filter addresses this concern, since it captures the metal/metal oxide coated soot particles while the metallic nanoparticles assists in its regeneration as it enhances soot oxidation by reducing the activation energy and decreasing ignition temperatures [8].

Iron compounds, as fuel additives, are of particular interest due to their ability to retain multiple oxidation states, while being principally non-toxic and abundantly available, thus having an advantage over other metals as potential catalyst material [9]. This has led to iron being used as a dopant along with cerium and platinum in diesel fuel [10] in various off and on-road applications in places around the world except in United States where on-road use is restricted [11]. Iron nanoparticles are characterized by their high affinity towards oxygen and are known to be pyrophoric due to their high surface area and high surface energies [12]. This qualifies them to be a good catalyst, albeit an unstable one in the presence of oxygen. Iron nanoparticles, in the presence of an oxidizing environment, form iron oxides, which are not harmful to the environment (present as rust). Various approaches exist for the introduction of iron catalyst to the flame. Generally, they involve the injection of vaporized or liquid iron compounds (precursors) into the flame. The description of one of them is given in the next section.

1.1.1 Aerosol flame synthesis

Aerosol flame synthesis presents itself as a cheap and effective catalyst synthesis method, that is easy to be scaled up [7]. This involves the injection of the precursors into a flame where the precursor decomposes to develop the catalyst particles. This process differs from the existing wet-methods like impregnation, sol-gel, precipitation etc. due to a much simplified synthesis process without the requirement for any subsequent treatment like separation and drying of the formed catalyst and any subsequent heat treatment [13]. Literature also reports the catalyst precursors to be undergoing high temperatures followed by a significant cooling gradient to form the catalyst particles. This results in the particles exhibiting lower degree of porosity, higher external surface areas and may also result in the evolution of catalyst in unique phases, whose formation under conventional processes is much more arduous to achieve [14] [15]. Depending upon the state of the injected precursor, aerosol flame synthesis is further classified into vapor-fed and liquid-fed aerosol flame synthesis, respectively. Another key distinguishing criterion among the derivatives of liquid-

fed aerosol flame synthesis is the source of energy for combustion [16]. While this energy is sourced through the combustion of an inflammable precursor in the flame spray pyrolysis process, the flame-assisted spray pyrolysis process utilizes the energy released from the combustion of a separately injected fuel [16].

1.2 Need for the present study

The synthesis of such catalysts results in significant reduction in the energy requirement especially when combustible precursors are used or when the catalyst synthesis is a supplementary part of another chemical process involving the use of fuels to generate energy. This renders this technique all the more suited to be used in power plants, furnaces etc. that mainly rely on combustion process for power generation and also need catalysts in order to curtail emissions. Thus, there is significant motivation for the development of cheap and novel catalysts that can successfully bring about simultaneous reduction in soot and NO_x as they are synthesized in-flame from iron additive doped fuel. Although much efforts have been directed towards the development of a variety of catalysts through the flame synthesis process as can be seen in the literature review section, most of the research on flame synthesis has focused either on studying the particle synthesis process from metal based precursor, or on assessing the emission reduction potency of the as-developed particles in the post-combustion zone. The collection and treatment of the synthesized particle sample, as done in post-combustion analysis, might lead to the agglomeration of the catalysts and reduction of their available catalytic sites, thus leading to an overall decline in activity. Analyzing the potential of such flame-produced particles in only post-combustion emission reduction perspective also undermines the influence of gas phase metallic species on the emission reduction process. Consequently, while the kinetics of iron precursor decomposition in flames and its flame inhibiting characteristics have been documented for premixed H_2/O_2 flames, a comprehensive understanding of their interdependency on fuel combustion kinetics along with the impact on emissions is lacking in the case of hydrocarbon fuels based diffusion flames.

Thus, considering the logistical challenges and cost of post-combustion emission treatment equipment, analyzing the implications of vapor phase iron precursor injection on hydrocarbon combustion in terms of achieving in-flame emission reduction process is worth investigating and is, therefore, the objective of the present work.

1.3 Research objectives

The injection of iron precursors in flames could result in significant reduction in the emissions as well as resource requirement, especially when the catalyst synthesis is a supplementary part of another chemical process involving the use of fuels. In order to achieve that, fundamental study is required to better assess the performance of iron precursor on emission reduction and the underlying physics. This fundamental study forms the primary objective of this doctoral thesis. This fundamental study is classified into various research projects. The specific goals of the project are as follows.

1. Investigation of the effect of iron precursor, in terms of emission reduction and underlying physics, on natural gas and ethanol emissions. This goal is achieved through the following approaches.[1]
    i) Development of suitable experimental infrastructure and methodology.
    ii) Mapping the concentration of reactants and key emission species to understand the underlying mechanisms and processes
2. Numerical analysis of iron pentacarbonyl loaded methane counterflow diffusion flame to identify key iron species, their reactions and associated kinetics with special focus on their contribution to emission reduction. This objective is attained through the following approaches.[2]

[1] This objective is achieved, as presented in Chapter 3.

[2] This objective is achieved, as presented in Chapter 4.

i) Development of a computational fluid dynamic model of the burner system incorporating all the underlying physics followed by its validation with experimental and literature results.

ii) Analyzing the impact of precursor concentration and fuel fraction on the emissions, iron species and key iron reaction kinetics.

3. Probe sampling and analysis of particle size and concentration under an iron pentacarbonyl precursor assisted methane counterflow diffusion flame. This is achieved through the following approach.[3]

    i) Development of experimental methodology for probe sampling from a counterflow methane flame ensuring minimal disturbance in the flow field.

    ii) Investigation of particle evolution process through analysis of particle size, number concentration and size distribution.

    iii) Verification of the results from the mobility analyzer and elemental analysis of iron through SEM Imaging/EDAX.

[3] This objective is achieved, as presented in Chapter 5.

Chapter 2

Literature Review

In this chapter, various reaction mechanisms involving the combustion of fuels are presented followed by the mechanisms responsible for NO_x and soot formation. Subsequently, previous findings related to the in-flame synthesis of iron and iron oxides and their catalytic potential to reduce emissions are discussed. It is followed by the analysis of previous attempts to utilize numerical techniques to model iron precursor assisted fuel combustion. The contribution of previous researchers in developing various aspects of the comprehensive gas phase iron pentacarbonyl decomposition and iron reaction mechanism is highlighted. In terms of experimental setup and methodology, the use of counterflow burner is justified in terms of its flexibility to impose temperature and concentration boundary conditions as well as due to its ability to simplify the underlying physics for better understanding. Existing literature focusing on particle sampling techniques from flames and subsequent analysis methodologies are explored to identify the most suited techniques for sampling flame synthesized particles and analyzing them. Lastly, the objectives of the present work are listed after identifying gaps in literature.

2.1 Fuel combustion chemistry

Since pollutant emissions are directly the outcome of fuel combustion chemistry, it is imperative to understand the underlying chemistry so as to be able to initiate measures for curtailing emissions. Methane remains the primary fuel of interest on account of its combustion being relatively cleaner than that of other fossil fuels, widespread use in gas turbines and automobiles and relatively less complex and well-studied mechanism. Though not the main objective of this thesis, limited analysis is also performed on using precursor laden ethanol combustion, since it is the most widely used biofuel and it remains more feasible over butanol on account of its larger lower heating value (LHV)/unit mass of input feed when produced from corn or switch grass using Acetone-Butanol-Ethanol fermentation [17].

2.1.1 Methane combustion chemistry

Due to its unique tetrahedral structure with large bond energies, methane combustion characteristics comprise of high ignition temperature, low flame speed and inertness with respect to photochemical smog [18]. As a result of the widespread use of natural gas, whose primary component is methane, a number of studies have been carried out analyzing methane combustion in gas turbines as well as in IC engines. The complete combustion of methane should result in the formation of CO_2 and water with the adiabatic temperature being 2226 K. However, the presence of many alternate pathways, sensitive to temperature, pressure and reactant concentrations, can lead to the formation of a number of products, some of which are the pollutant species. Puri et al. [19] and Khanna et al. [20] investigated CO and NO_x emissions from a counterflow and a premixed burner, respectively. The result demonstrated the presence of NO_x and CO to be around 30 ppm and 125 ppm, respectively, and a strong dependence on the equivalence ratio in case of premixed flame. Two key reaction pathways have been proposed for methane combustion depending on the temperature [18] [21] [22]. Figure 2.1 highlights the key reaction pathways under high temperature along with additional pathways which are activated under low temperature conditions [18].

1) High temperature reaction pathway (2200 K)

The main reaction pathway, shown in Figure 2.1, is initiated by O, OH and H radicals reacting with CH_4 to produce methyl radical (CH_3), which reacts with O to form formaldehyde (CH_2O). This formaldehyde also reacts with radicals to form formyl radical (HCO) which is further acted upon by the radicals to produce CO and ultimately CO_2 due to oxidation by OH. Apart from the direct pathway of methyl radical (CH_3) forming formaldehyde, two other pathways also lead to the formation of CH_2O. While one leads through the development of CH_2* to CH_2 and CH to form formaldehyde (CH_2O), the other less prominent pathway leads to the conversion of CH_3 to CH_2OH, which is ultimately converted to CH_2O. It is observed that most of the reactions in the high temperature regime are not reversible.

2) Low temperature reaction pathway

Temperatures less than 1500 K lead to additional reaction pathways, which were initially dormant at higher temperatures, getting activated. These pathways are highlighted in red color in Figure 2.1. Thus apart from most of the reaction pathways in the high temperature regime, some new pathways are added. They include the recombination of CH_3 back to CH_4; a new pathway converting CH_3 to methanol which ultimately gives CH_2O and formation of ethane (C_2H_6) due to recombination of methyl radicals. Some part of this C_2H_6 gets converted to CO and CH_2 through C_2H_4 and C_2H_2.

2.1.1.1 GRI 3.0 mechanism

Since the flame structure, which itself depends on many operating parameters, governs the temperature distribution within the flame, hence adopting the low or high temperature model could introduce significant error. Therefore, a unified approach towards the methane combustion mechanism is required that covers the complete operating range for the temperature. This is achieved through the GRI 3.0 mechanism that is optimized for the combustion of methane in the temperature range of 1000K to 2500 K ,with pressure ranging

from 10 torr to 10 atm and equivalence ratios varying from 0.1 to 5 for premixed systems [23] [24].

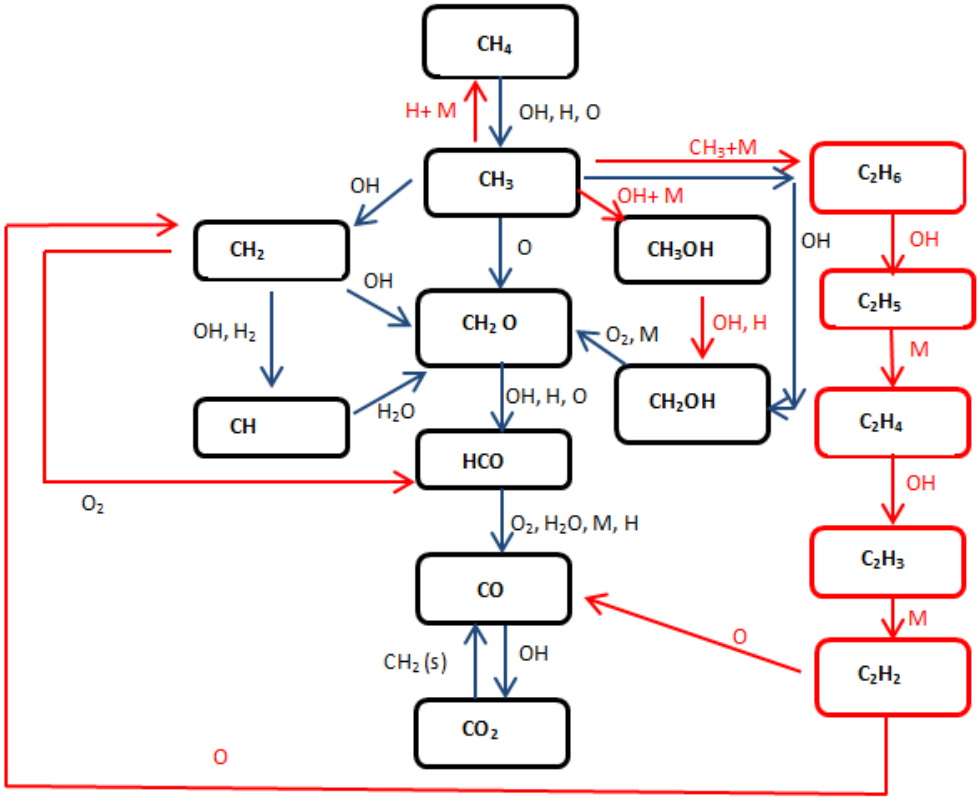

Figure 2.1: Methane-air combustion pathway in a well stirred reactor under high-temperature (2200 K) with additional pathways which get activated when combustion is at lower temperature (1345 K)

2.1.2 Ethanol combustion chemistry

The ethanol combustion mechanism, used in the present study, is an aggregation of mechanisms governing the combustion of hydrogen [25], carbon monoxide [25], ethane [26], ethylene [27], acetylene [28], propane [29], propene [29], propyne [29], allene [29], methanol [30] and methane [31] , which are linked to ethanol by incorporating the steps provided in the works of Li et al. [32] and has been used in the study of counterflow ethanol flame by Saxena et al. [33]. The mechanism is shown in Figure 2.2. This reaction mechanism consists of 55

reactions involving ethanol, acetaldehyde and their isomers. More than 20% of the fuel decomposition is achieved through the direct decomposition of the fuel to C_2H_4 in partial premixed flames while more than 50% is achieved in the case of diffusion flames. Apart from fuel decomposition, ethylene is also produced by the decomposition of some of the hydroxyl ethyl radicals formed from ethanol through H-abstraction. The other hydroxyl ethyl radicals produce significant amount of acetaldehyde (CH_3CHO), which generates significant quantity of CH_3 radicals. Ethoxy radicals also contribute to the formation of CH_3 as well as that of acetaldehyde (CH_3CHO). Both methane and ethane are produced as a result of these CH_3 radicals. The species and values on the arrows represent the agents causing the change. The fate of some minor species is not depicted as they were produced in insignificant quantities and did not contribute much to the mechanism.

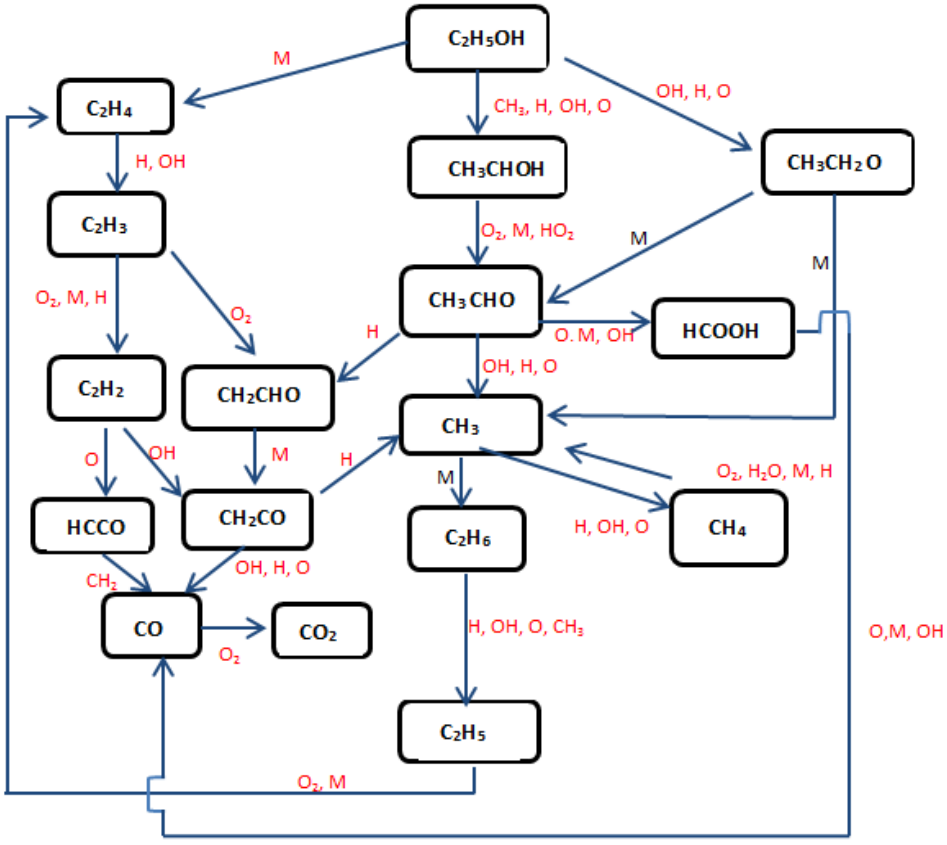

Figure 2.2: Ethanol combustion mechanism [33]

2.2 Pollutant species formation in combustion process

Soot and NO_x have been globally recognized among the key polluting species [34]. The conditions leading to the formation of either of them would, intuitively, seem to inhibit the inception of another. While soot is the unburnt carbon which could be an outcome of insufficient oxidizer or insufficient heat release during the combustion process, NO_x is primarily generated due to decomposition of N_2 at high flame temperature. However, the non-uniformity of combustion in the chamber may lead to localized areas having both the extremities leading to the evolution of both.

2.2.1 NO_x formation during combustion process

In nitrogen-free fuels, the NO inception is realized by the following three mechanisms utilizing the N_2 present in the air [18] [35] [36] [37]:

1) Zeldovich or thermal mechanism:

This mechanism is the most prominent source of NO at high temperature across a wide range of equivalence ratios. It chiefly comprises of three chain reactions (1)-(3) [18]:

$$O+N_2 \Leftrightarrow NO+N \qquad (1)$$

$$N+O_2 \Leftrightarrow NO+O \qquad (2)$$

$$N+OH \Leftrightarrow NO+H \qquad (3)$$

Due to the consumption as well as the production of species like O_2, O and OH, this mechanism gets linked to the fuel combustion chemistry in which these species also play an important role. Under the circumstances of full fuel combustion being achieved before the onset of NO inception can take place, the estimation of rate of NO formation becomes simplified and is only dependent on the equilibrium concentrations of N_2, OH, O and O_2 , although the actual NO rates could be much higher due to the super-equilibrium concentrations of O atom. Reaction (1) requires much higher activation energy compared to reactions (2) and (3) and consequently could only be initiated at temperatures higher than

1800 K. As a result, the chief contribution of this mechanism in terms of NO formation is mainly among the post-combustion flue gases due to its time scale being significantly higher than the fuel combustion mechanism.

2) N_2O-intermediate mechanism

This mechanism gains prominence especially under the fuel-lean regime ($\varphi<0.8$) like gas turbines and is, thus, actively being researched into. It consists of the following reactions (4)-(6) [18]:

$$O+N_2+M \Leftrightarrow N_2O+M \quad (4)$$

$$H+N_2O \Leftrightarrow NO+NH \quad (5)$$

$$O+N_2O \Leftrightarrow NO+NO \quad (6)$$

3) Fenimore mechanism (prompt NOx)

Fenimore et al. [38] observed the evolution of NO in premixed laminar flame at temperatures much insignificant for the production of NO through the thermal mechanism. They emphasized the close interaction between the fuel combustion chemistry and the nitrogen for this. The hydrocarbon radicals produced during fuel combustion react with nitrogen to form cyano compounds and amines which ultimately form NO through intermediate products. The mechanism is as follows (7)-(12) [18]:

$$CH+N_2 \Leftrightarrow HCN+N \quad (7)$$

$$C+N_2 \Leftrightarrow CN+N \quad (8)$$

For equivalence ratios less than 1.2, the reactions follow the following sequence

$$HCN+O \Leftrightarrow NCO+H \quad (9)$$

$$NCO+H \Leftrightarrow NH+CO \quad (10)$$

$$NH+H \Leftrightarrow N+H_2 \quad (11)$$

$$N+OH \Leftrightarrow NO+H \quad (12)$$

While at equivalence ratio greater than 1.2, NO production is hampered due to the conversion of NO to HCN [39]. In premixed combustion systems, it has been established that at higher equivalence ratios (fuel-rich mixtures), this mechanism dominates and produces as much as 95% of the total NO at the equivalence ratio of 1.32 [40].

2.2.2 Soot formation during combustion process

Soot comprises of carbon particles generated as a result of the incomplete combustion of a hydrocarbon fuel. Soot inception with polycylic aromatic hydrocarbons (PAH) species as the precursor has been the most widely accepted synthesis mechanism as compared with some other research works, which point to the presence of resonantly stabilized free radical species like propargyl, benzyl, cyclopentadienyl being an important factor in aromatic formation [41] [42] [43] [44] [45] [46]. The mechanism, shown in Figure 2.3, can be described as follows:

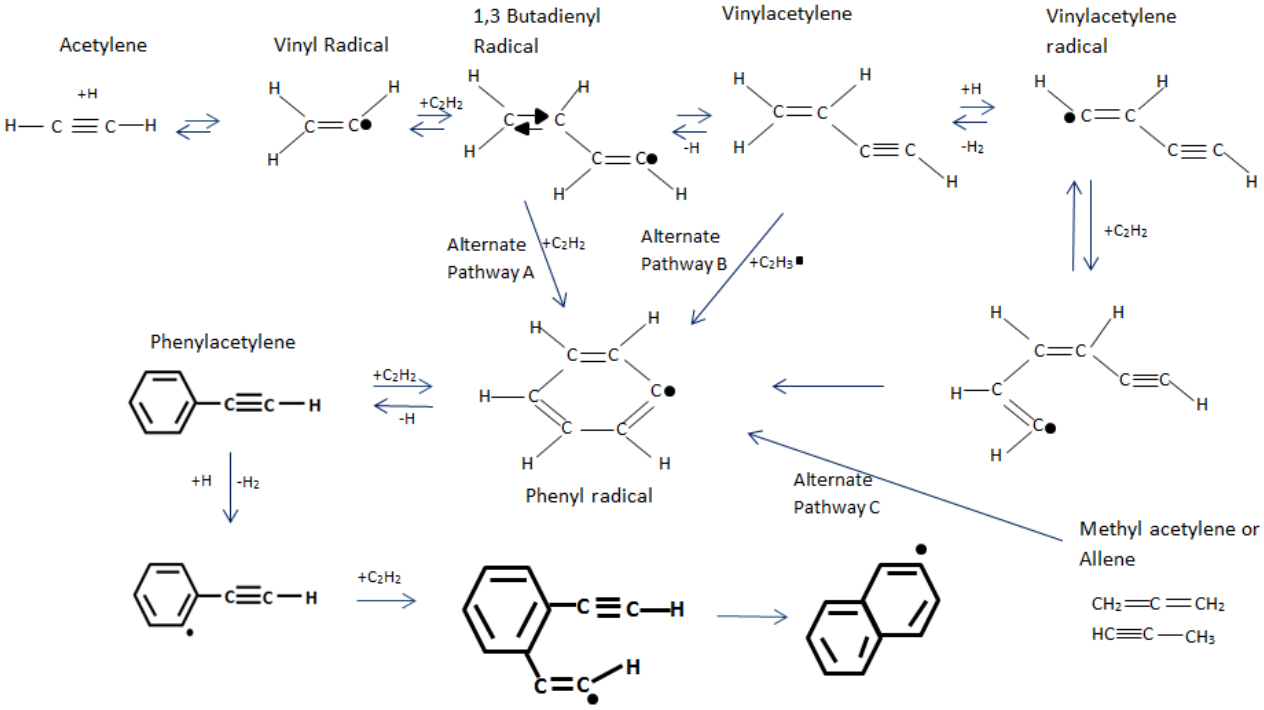

Figure 2.3: Hydrogen –Abstraction-Carbon-Addition (HACA) soot formation mechanism [44]

i) The decomposition of the hydrocarbon fuel molecules into smaller molecules as well as into radicals like CH, C_2H_2, C_2H_3 through various pathways at different temperatures.

ii) The produced C_2H_2 reacts with the smaller molecules or hydrocarbon radicals like vinylacetylene radical (C_4H_3) to form aromatic compounds, like benzene and phenyl radical C_6H_5, especially at higher temperature. Two alternate reaction pathways 'A' and 'B' as shown in Figure 2.3 are also proposed for the reaction of C_2H_2 to 1,3 butadienyl radical (C_4H_3) and vinylacetylene (C_4H_4) respectively. Methyl acetylene and allene undergo pyrolysis to form the ring structure of C_6H_5 through another pathway 'C' also depicted in the Figure 2.3. This particular step of aliphatic molecules to form the ring structure is considered as the rate determining step.

iii) C_2H_2 undergoes polymerization to form cyclic and aromatic species which undergo further polymerization and transforms into PAH through the addition of C_2H_2 and the abstraction of H. The other non-HACA mechanisms attribute the formation of first aromatic species to the reaction among resonantly stable aryl species. Beyond a critical size of these PAHs, the inception of first soot particles, having sizes around 1.5 nm, occurs [47] [48].

iv) These incipient smaller soot particles collide with each other and undergo structural transformation that depends on factors like primary particle size, temperature, residence time etc. [49]. The nascent soot particle behaves like a liquid droplet and merges together to form bigger particles. Mature soot particles, with a much smaller restructuring period, also lead to the formation of fractal aggregate-like structure [50] [51].

v) The surfaces of nascent soot particles have large concentration of hydrogenated sites. Soot growth is achieved by Hydrogen-Abstraction-Carbon-Addition (HACA) mechanism involving abstraction of H-atom from soot surface to form an aryl radical site, on which the gas phase C_2H_2 adds itself resulting in soot

diameter growth [47] [52]. This surface growth results in an increase in particle size while not impacting the particle concentration.

vi) Some amount of this soot is also oxidized by the oxygen and OH while the remaining is emitted as particulate matter.

2.3 Emission reduction

Emission reduction through the post-combustion catalytic treatment of product gases as well as the catalytic combustion of the fuel to reduce the formation of pollutant species in flame are the most prevalent approaches utilized to achieve clean combustion. Since the inception requirements of NO_x and soot differ drastically in terms of the operating parameters, any catalyst specifically designed to arrest emissions of either of the two might fare poorly in checking the other. Sufficient literature is available related to the development and functioning of such catalysts. Addition of metal precursors which leads to formation of metal or metal oxide particles in flames is found to result in enhanced combustion, lesser PM and unburnt carbons resulting in higher calorific values [53] [54] [55].

2.3.1 Emission reduction in methane and ethanol combustion

Marinov [56] compared PAH formation in premixed methane flame with that of ethane and propane. The results demonstrated that propane generated the most PAH and benzene levels while ethane forms the least. Methane flame also formed the least C_2H_2 and soot, as compared to the other fuels. Smyth et al. [57] utilized a co-flow methane diffusion flame to study soot formation and found consistency among the peak location of C_2H_2 and C_6H_6 with early soot particles, which corroborated the fact that C_2H_2 and C_6H_6 species are precursors for soot. Hahn et al. [58] analyzed methane combustion in a counterflow diffusion flame configuration, both experimentally and numerically, and verified the kinetic mechanism for NO_x through experimental results. Blevins et al. [59] simulated a partially premixed methane counterflow flame with low strain rates using GRI 2.11 mechanism. The results demonstrated strong correlation between CH_i species, NO evolution and the equivalence ratio. Beltrame et al. [60] and Dupont et al. [61] also explored soot and NO formation in a CH_4/O_2 enriched

counterflow diffusion flame, both numerically using GRI 2.1 and experimentally. Trends of C_2H_2, C_2H_4, C_2H_6 species were used to validate the numerical model for soot prediction. Studying the NO evolution in the flame underlined the importance of thermal and prompt mechanism.

Ethanol, along with cetane improvers, is expected to reduce particulate emissions in diesel engines [62]. The results of past studies with ethanol have been quite mixed. Ethanol-diesel blends with 10%-15% ethanol have been reported to reduce particulate emissions by 20%-41% [63], although NO_x and aldehyde emissions showed an increase [64] [65]. Hansdah et al. [66] injected bioethanol in the form of fumes in a direct injection diesel engine, which resulted in a decline in the NO and smoke emissions as compared to pure diesel fuel at full load conditions. Jamuwa et al. [67] analyzed the use of pure ethanol in a compression ignition engine, which resulted in a significant reduction in NO_x and CO_2 emissions but an increase in CO and particulate emissions. No previous analysis of the impact of iron precursor on ethanol emissions has been carried out to the best of our knowledge, although previous efforts have been carried out in exploring the impact of ceria additive in the oxidation of ethanol, which was considered to be representative of volatile organic compounds species. The results demonstrated an increased selectivity towards the formation of CO_2 [68].

2.3.2 Iron particles

Iron particles, in the presence of an oxidizing environment, form iron oxides that are relatively harmless (already present as rust). While the catalytic activity of iron oxide (Fe_2O_3) is less as compared to CuO and Mn_2O_3, iron oxide catalysts are still capable of achieving complete combustion of natural gas provided that its iron level is above a certain level [69] [70] [71]. Above that threshold, the activity increases linearly with iron contents [69] [70] [71]. The decomposition of metal precursor in the flame as well as the size, growth and morphology of evolving particles are significantly affected by the operating conditions and reactants. Since the catalytic activity is closely linked to the particle size, hence investigating

the precursor decomposition process becomes critical in metal based fuel additives. The blending of iron precursors with fuels has been carried out in engines as well as in flames.

Kannan et al. [72] and Fazliakmetov et al. [73] have highlighted the influence of iron additives in reducing PM emissions and enhanced oxidation of hydrocarbons. Nash et al. [11] observed that on the addition of iron as the fuel based catalysts to the flame, an overall decline in terms of total mass (32%) and volume concentrations (39%) was witnessed though the number of particles had demonstrated an increasing trend with the amount of catalyst added (0 to 200 ppm). This was on similar lines to the findings of Skillas et al. [74], which pointed to the decrease in particulate matter emission by 25-42%. Miller et al. [75] analyzed the impact of iron-doped diesel fuel on 1.5 litre diesel engine and detected a 20%-40% decline in total carbon in the samples collected from exhaust with 60 ppm iron. They deduced a threshold iron to carbon ratio of 0.013 for this engine, below which no effect of iron precursor was seen on soot morphology. They reported two different modes for the soot and metal nanoparticles: primary iron nanoparticles (5-10 nm) attached to carbon agglomerates and coagulated iron agglomerates (20-200 nm) attached to carbon agglomerates. While the authors hinted at the possible role of gas phase iron species, no conclusive evidence was provided.

Extensive work in exploring the influence of iron on the flame and its final products has been carried out. Gonzalez-Carreno et al. [76] utilized different Fe^{2+} and Fe^{3+} salts dissolved in ethanol in the flame synthesis process to produce and analyze the properties of the as-produced γ-Fe_2O_3. The salts included nitrates, ammonium citrate, chlorides and acetylacetone. The oxide was also reported to be in a disordered lattice. While chloride precursor leads to a mono-crystallite product with high degree of crystallinity (size of 60 nm), those from ammonium citrate develop hollow spherical shells (170 nm) [76]. The nitrate precursors develop compact spherical aggregates (around 180 nm), while the lowest size of around 6 nm was observed in the product prepared from acetylacetone precursors having a monodispersed structure [76]. Grimm et al. [77] used iron acetylacetone and iron pentacarbonyl, respectively, dissolved in toluene as the precursor into an oxyhydrogen flame.

The average particle size observed in the combustion of acetylacetone precursor in the flame was around 9 nm as a result of poor aggregation. The chief constituent of the powder was found to be γ-Fe_2O_3. Kagawa et al. [78] observed that the formation of α-Fe_2O_3 occurs at temperatures greater than 550 ^oC, as was achieved in his work [78] through inductively coupled plasma. The combustion of iron pentacarbonyl dissolved in toluene solution through an oxy-hydrogen flame resulted in the formation of γ-Fe_2O_3 with average size of 12 nm and not Fe_3O_4, which was otherwise produced when iron pentacarbonyl was combusted under a free flame [77]. Increasing the concentration of iron in the precursor was reflected in the increasing particle size. This was important as they demonstrated how particle size governed the formation of different end products formed from the same reactants. In oxy-hydrogen flame, Fe^{2+} is incepted at high temperature and comes into contact with CO_2 adsorbed on the particle surface [77]. This CO_2 acts as a source of electrons to oxidize Fe^{2+} to Fe^{3+} to result in the formation of different end products. A high degree of quenching through a larger retention time in the flame leads to the conversion of γ- Fe_2O_3 to α-Fe_2O_3. A smaller sized particle of γ- Fe_2O_3 will be engulfed by the reductive adsorbates, i.e. carboxylate ion and be transformed into Fe_3O_4 while a larger size particle, in the absence of sufficient carboxylate ions, result into α-Fe_2O_3 [77].

Janzen et al. [79] utilized a low pressure lean- H_2/O_2/Argon flame doped with varying concentrations of $Fe(CO)_5$ premixed with argon to generate Fe_2O_3 nanoparticles in flame. Premixed laminar flames were utilized for achieving the easily distinguishable one-dimensional structure with an extended reaction and particle formation zone. The particles were analyzed in-situ using a particle mass spectrometer (PMS). They also developed a numerical model comprising of homogeneous gas phase reactions along with a sectional model focusing on capturing the particle inception. The results demonstrated an increase in particle mass with increasing distance from the flame at different H_2/O_2 ratios. While temperatures did not seem to affect the particle size, increasing $Fe(CO)_5$ concentrations did lead to an increase in the particle size, which, however, was not captured in numerical studies [79]. With a mean particle size of around 10 nm as obtained under in-situ analysis, the paper

reported an increase in size due to growth on the substrate and annealing which underlines the importance of proper probing and measurement diagnostics [79]. The chief constituent of the products were γ-Fe_2O_3 with some α-Fe_2O_3 impurities [77] .

Yu et al. [80] achieved the synthesis of iron nanoparticles through the use of ethanol fuel with iron pentacarbonyl precursor in a ratio of 5:1. However, the particles had a core-shell structure indicating encapsulation by carbon in the ordered graphene state on the shell and either α- Fe_2O_3 or Fe_3C, which is distinctly distinguishable from the amorphous carbon, as was achieved in some studies [81]. Their study pointed out the creation of a Fe-C solid solution which, on cooling, led to the condensation of carbon in the form of an outer shell [80]. The authors also pointed out the absence of any carbon nanotubes or nanofibers in the sample, although the same process of carbon dissolution and subsequent condensation form the underlying principles of carbon nanotube and nanofiber synthesis. This is due to the fast decomposition of $Fe(CO)_5$ that led to large concentration of iron nanoparticles, which might have caused the dissolution of the available carbon [80].

Ma et al. [82] calculated a 3.7% fuel saving by using ferrous thiocyanate in diesel engine at 3200 rpm. Similar results with respect to fuel efficiency have also been demonstrated by using other ferrous compounds like ferrous picrate and iron chloride [83] [72]. Song *et al.* [84] focused on fuel-borne-precursor (4:1 iron to strontium ratio) assisted particulate matter oxidation under varying engine loading conditions (from 25% to 75% of peak load) and identified the multiple-oxidation-state retaining capability of in-flame metal oxides to be a significant driving force for emission reduction. However, no attempt was made to explain the emission reduction mechanism in depth. Key research findings on the use of iron based particles as catalysts are mentioned in Table 2.1. Pivkina et al. [85] and Jayaraman et al. [86] have attributed the enhanced oxidation capabilities of iron nanoparticles to their ability to potentially store energy on their surfaces. The unique property of metallic oxides to absorb and donate oxygen was attributed to their dual ability to reduce NO_x and oxidize CO, respectively [72] [87]. Similar observations were also made by Reichert et al. [88] and Fennell et al. [89] in terms of the enhanced conversion of NO_x and soot to N_2 and CO_2,

respectively, with excess O_2 under the influence of Fe_2O_3 in a post-combustion study. NO was found to undergo dissociative adsorption on soot-catalyst interface to produce adsorbed N and O atoms. The Fe_2O_3 lattice was found to provide enhanced surface mobility to atomic oxygen towards the soot-catalyst interface where soot is oxidized to CO_2 and the adsorbed atomic nitrogen (N) recombined to form N_2.

i) Iron pentacarbonyl chemistry

Iron pentacarbonyl ($Fe(CO)_5$) is a homoleptic metal carbonyl compound having high vapor pressure, which makes it attractive to be used as an iron precursor in flames. Reinelt et al. [90] reported $Fe(CO)_5$ to extend an inhibitory effect on flame propagation. In premixed flame, the effect was attributed to the recombination of H, O and OH atoms, which are the species responsible for propagation of the reactions, on surfaces of the products of $Fe(CO)_5$ decomposition. This effect was mainly observed at lower concentrations of $Fe(CO)_5$, while this inhibition effect becomes weaker at higher concentrations. The authors have hinted at agglomeration of iron particles being responsible for the reduction in the inhibition effect. In counterflow flames, the addition of $Fe(CO)_5$ on the oxidizer side resulted in a better flame retardation as compared to CF_3Br while its addition on the fuel side resulted in an increased flame propagation. They attributed this to the sub-equilibrium radical concentration on the fuel side and super-equilibrium radical concentration on the air side as was witnessed under numerical studies.

Rumminger et al. [91] put in efforts to further explore the inhibition mechanism of $Fe(CO)_5$ in counterflow and premixed flame through both experimental and numerical means. They observed the relative insignificant impact of $Fe(CO)_5$ decomposition as well as of Fe oxidation into FeO on flame inhibition under premixed conditions. In the case of premixed flames, extensive influence of the reactions resulting in hydrogen species abstraction was reported on the flame inhibition. Also the influence of iron reactions in the production and consumption of H radicals was reported to decline with increasing O_2 inlet mole fractions. A higher concentration of H-radicals than the equilibrium concentration was observed which was found to decline at higher iron concentration. They explained the loss of flame inhibition

characteristics at higher concentrations of $Fe(CO)_5$ as a result of decrease in this difference between the actual and equilibrium concentration of H-radical. However, in the case of counterflow burners, the decline in inhibition effect is attributed to the condensation of iron at higher inlet mole fractions. This was also supported by the works of Linteris *et al.* [92] who explored $Fe(CO)_5$ addition to a H_2-O_2 flame and found that the inhibition effect only comes into picture at higher concentrations (>150 μL/L) of iron compounds, while at lower concentrations, as also illustrated by Park *et al.* [93], $Fe(CO)_5$ promotes ignition through the enhancement of the oxidizing radical pool (H, O, OH). Celnik et al. [94] numerically analyzed the decomposition of carbon from source species like CO and their subsequent deposition on Fe. For the fuel decomposition, CO disproportionation and CO hydrogenation were proposed as possible mechanism that ultimately led to the formation of C atoms. These C atoms dissolve in the Fe catalyst to a saturation limit that is governed by the temperature beyond which a graphene layer or a carbon nanotube is formed.

Once the effectiveness of $Fe(CO)_5$ was established in reducing flame speeds and soot emissions from engines, the focus shifted towards more fundamental level analysis of the interactions of $Fe(CO)_5$ and the flame in terms of emission reduction. Kim et al. [95] explored the addition of 4000 ppm of $Fe(CO)_5$ to an isooctane diffusion flame in terms of soot reduction under actual operating conditions of a combustor and later analyzed the interactions between the iron species and soot particles in a similar isooctane diffusion flame [96]. Their work attributed the oxidative catalysis of soot to carbon coated iron/iron oxide particles which has also been suggested by Zhang et al. [97] and Rumminger et al [98]. The soot formation process is divided into three overlapping regions viz. the particle inception, particle growth and soot burnout regime with an overall residence time of the iron species in flame to be 50 miliseconds. Using light transmission measurement techniques, only a minor increase in the particle inception and no impact on soot growth was witnessed [95]. This study did not make any distinction between the soot and iron particles while analyzing the increased particle inception, which was attributed to enhanced soot inception over increased surface area of incepted iron particles. A significantly higher decline in soot under the soot

oxidation regime, as compared to the unseeded flames, was also documented. This was attributed to the enhanced soot oxidation by the iron (Fe)-rich nuclei dispersed among the soot particles under fuel rich conditions in the primary flame region and by the iron oxides (Fe_2O_3 and Fe_3O_4) under fuel lean conditions [95] in the soot oxidation region.

Table 2.1: Key research findings from the addition of iron precursors to flame

Authors	Key findings
Kannan et al. [72] Fazliakmetov et al. [73]	1. Iron additives proved effective in reducing PM emissions and enhanced oxidation of hydrocarbons.
Nash et al. [11] Skillas et al. [74]	1. Decrease in mass and volume concentrations of particulate matter by 32% and 39%, respectively.
Gonzalez-Carreno et al. [76] Grimm et al. [77] Kagawa et al. [78]	1. Chloride precursor forms a mono-crystallite product with high crystallinity (60 nm); ammonium citrate develops hollow shells (170 nm); iron nitrate precursor develop compact spherical aggregates (180 nm); iron acetylacetone precursor produce mono-dispersed particle (6 nm); toluene dissolved iron acetylacetone and iron pentacarbonyl produces γ-Fe_2O_3 particles (9 nm)
Janzen et al. [79] Yu et al. [80]	1. H_2/O_2/Argon flame doped with $Fe(CO)_5$ generates 10 nm Fe_2O_3 nanoparticles in flame, majority being γ-Fe_2O_3 with some α-Fe_2O_3 .
Ma et al. [82] Pivkina et al. [85] Jayaraman et al. [86]	1. 3.7% fuel saving by using ferrous thiocyanate in diesel engine. 2. Enhanced oxidation capability due to their surface energy storage ability.
Reichert et al. [88] Fennell et al. [89]	1. NO_x , soot convert faster to N_2 and CO_2 with Fe_2O_3 under excess O_2. 2. Dissociative adsorption of NO on Fe_2O_3 to produce N and O atoms. 3. Fe_2O_3 lattice enhances O mobility towards soot-catalyst interface.
Kim et al. [95] [96] Zhang et al. [97] Linteris et al. [92] Park et al. [93]	1. Enhanced soot oxidation by O,OH species on soot covered iron. 2. Higher $Fe(CO)_5$ concentration enhances inhibition while lower concentration promotes ignition by increasing the radical pool (H,O, OH).

2.4 Reaction mechanism of iron pentacarbonyl

In order to develop better understanding of the chemistry of gas phase iron precursor and its decomposition, numerical studies were employed. Numerical modeling of the iron pentacarbonyl doped fuel combustion required a mechanism that can adequately count for the gas phase intermediates, final products and all stages of the reaction. To address the requirement of developing a mechanism, Giesen et al. [99] came up with a single global reaction to represent the iron pentacarbonyl decomposition without accounting for any intermediate or byproducts: $Fe(CO)_5 \rightarrow Fe + 5CO$. The key issue with this mechanism was the unrealistically fast kinetics for the iron atom association reaction to form a dimer. Krestinin et al. [100] came up with a two stage mechanism : i) $Fe(CO)_5 \rightarrow FeCO + 4CO$ and ; ii) $FeCO \rightarrow Fe + CO$ to describe this decomposition; however, the dissociation energy used for this reaction is significantly greater than what was observed experimentally [43]. In their numerical efforts to analyze premixed and counterflow methane flame loaded with $Fe(CO)_5$, Rumminger et al [91] combined methane combustion mechanism GRI-Mech 1.2 along with a developed iron mechanism. This iron mechanism incorporated some of the initial work of Jensen et al. [101] focusing on enhanced H-atom recombination under $Fe(CO)_5$. The multi-staged reaction mechanism can be divided into three main components i) decomposition of $Fe(CO)_5$; ii) iron species formation and; iii) homogeneous reactions of the iron species scavenging reaction propagating radicals. This approach did not, however, consider possible polymerization of iron atoms to form clusters.

To further expand $Fe(CO)_5$ decomposition mechanism, Wen et al. [102] utilized the density functional theory (DFT) for detailed kinetic modeling of decomposition of $Fe(CO)_5$ in a shock tube under an inert argon atmosphere. It involved the calculation of thermochemical data for Fe_n ($n>=2$) , iron carbonyls and iron cluster complexes with CO while the chemical activation energies and the fall off rates were estimated using the Quantum Rice-Ramsperger-Kassel method (QRRK) and three body method. These are species whose thermochemical and kinetic data were not available on account of their short life time. Their work pointed out the decomposition of $Fe(CO)_5$ into $Fe(CO)_4$ and CO as the rate determining

step and also drew attention to the temperature threshold of around 800 K, above and below which, the decomposition of $Fe(CO)_2$ follow different pathways leading to different end products. While Rumminger et al. [91] assumed the decomposition of iron into Fe atoms, Wen et al. [102] further expanded the model to include iron clusters Fe_n, iron carbonyls $Fe(CO)_n$ and other intermediates $Fe_m(CO)_n$. Their methodology included the analysis of the mechanism in terms of molecular level reactions in the gas phase as well as those in the initial particle phase. The initiation of agglomeration was incorporated in the mechanism till a specific cluster size represented as a "bin" beyond which further agglomeration was depicted as reactions between the bins. Thus, this work details the reaction mechanism of iron pentacarbonyl decomposition and the coalescence of the nanoparticles upto a minimum aggregate size beyond which the reaction is depicted in terms of the interaction between aggregate particles. The paper reports the iron carbonyl structure to be more open as compared to that of iron clusters which occupy a caged structure. $Fe(CO)_2$ is found to be the most stable among all the iron carbonyls. At temperatures ranging from 400 K to 800 K, $Fe(CO)_2$ survives long enough to produce large iron clusters while lesser Fe atoms are formed. These iron clusters undergo nucleation and evolve into nanoparticles. On the contrary, high temperatures lead to the rapid breakdown of $Fe(CO)_2$ to produce Fe atoms, only some of which were able to form dimers thus resulting in fewer nanoparticles. Kluge *et al.* [103] and Poliak *et al.* [104] have credited these iron clusters to be the precursors of experimentally verified 'prompt nanoparticles' formed close to the burner surface in a premixed laminar flat-flame.

Janzen et al. [79] demonstrated particle growth simulation based on a sectional model containing the population balance equations. The model, however, neglected any intermediates formed as a result of interactions between iron and flame species. Wlokas *et al.* [105] investigated the formation of gas phase Fe_2O_3, both numerically and experimentally, in a premixed H_2/O_2 mixture. They appended the model developed by Ruminger et al. [91] with another sub-mechanism addressing the formation of gas phase iron oxide from iron atoms based on experimentally characterized concentrations of iron atoms and iron oxide particles.

Figure 2.4 graphically highlights the decomposition of $Fe(CO)_5$ and the subsequent fate of iron.

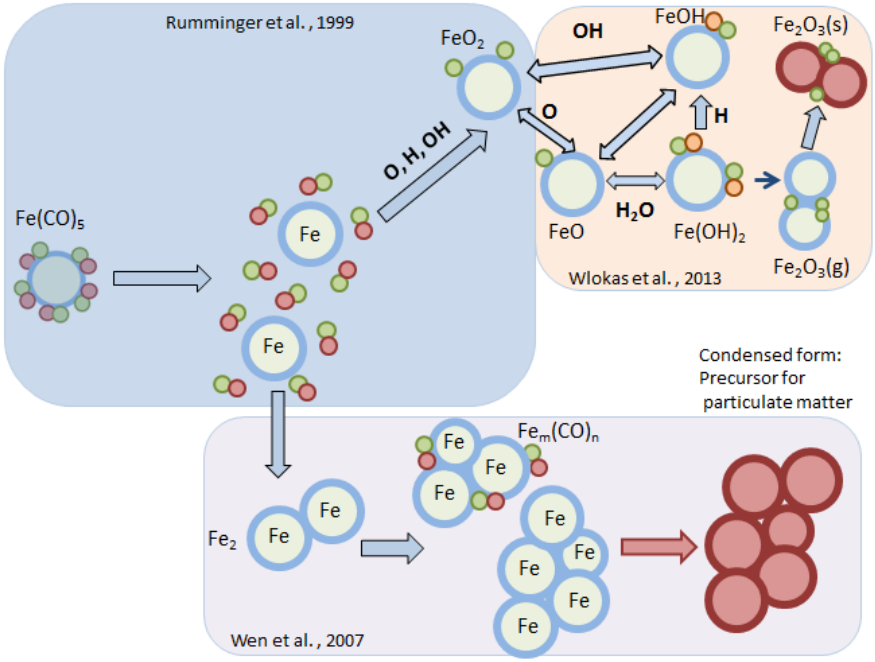

Figure 2.4: Graphical representation of $Fe(CO)_5$ decomposition and subsequent fate of iron

2.5 Counterflow flame configuration

Non-premixed flames are generally preferred in combustion applications like furnaces, gas turbines and diesel engines due to considerations of safety [106]. Premixing before combustion effectively rules out diffusion as the possible rate determining process, while in a non-premixed flame, the time scale of the chemical reaction is often much smaller compared to the diffusion and convective time scales [106]. A turbulent diffusion flame, as observed under a variety of combustion systems mentioned above, can be inherently viewed as a collection of multiple laminar flamelets [107]. Such flamelets in a turbulent flame can be approximated by means of a counterflow diffusion flame which possesses the same scalar structure and therefore can represent the inherent chemistry and transport phenomenon in the

flamelets [107]. The counterflow configuration general involves a planar structure and assumes the Lewis number to be unity, indicating equal thermal and species diffusivity, which effectively removes the complexity introduced by the phenomenon of curving of flames as seen through the use of non-unity Lewis number [108]. This also significantly simplifies the modeling process since the mixing of fuel and oxidizer is completely governed by diffusion process as the turbulent mixing is not considered [109]. Moreover, the use of scalars: mixture fraction 'Z_f', to which the mass fractions of all other species are directly related and; instantaneous scalar dissipation rate 'χ_{st}' which incorporates convection and diffusion components in the flow, renders the mathematical formulation of counterflow flames much simpler for analysis [107]. Previous studies [110] [111] [112] have highlighted the suitability of this flat diffusion flame for studying fast burning fuel/air mixtures and the high temperature oxidation kinetics at the atmospheric pressure. Consequently, a porous counter flow burner is chosen since it produces a stable, planar, two-dimensional diffusion flame front that provides ease of diagnostics of gases and particles [109]. It also provides flexibility to inject precursor from either the fuel or oxidizer side and impose temperature and oxygen concentration gradients as well as provides little to no disruption of the flame while sampling.

2.6 Particle size measurement

Techniques used for particle size measurement comprises of both intrusive and non-intrusive techniques. The non-intrusive techniques generally involve laser excitation followed by measuring extent of extinction and scattering [113] [114] and Laser Induced Incandescence (LII) [115] [116]. LII involves rapidly heating the sample using a pulsed laser source. Due to the subjection of the sample to such intense energy, the nanoparticles present in the samples are elevated to high temperature. The nanoparticles equilibrate thermally with their surroundings by size-dependent heat transfer processes including conduction and evaporation [117] [118]. The nanoparticle size can be inferred by regressing a measured pyrometric temperature, taken from time resolved incandescence measurements in the

nanoparticles, to modeled temperature produced by the heat transfer model [118]. Since material specific quantities like specific heat capacity and density are the pre-requisites for this technique, hence material characterization through XRD technique needs to be carried out before utilizing this. A key shortcoming of LII involves the assumption of a complex refractive index for the particles, that is greatly dependent on fuel type [119] and wavelength [120] used. Moreover, extinction measurement techniques are restricted by their requirement for line of sight approach and therefore are unable to ascertain particle size distribution although they have been used to measure soot volume fraction and some size dependent parameter [121]. While LII is gaining popularity as an effective technique for measuring soot volume fraction [122], the significant drawback associated with it is its inability to determine particles of bimodal size distributions, since small sized particles contribute very little to radiation [123]. Photo Ionization Mass Spectroscopy (PIMS) supersedes other techniques in terms of sensitivity and have detection range of the order of atoms and molecules, however, its upper range is limited to just 6 nm [124].

While intrusive techniques, like SEM and TEM sampling are less rigorous in terms of their formulation and do not require prior assumption with regard to optical properties, they are more cumbersome in terms of their requirement for multiple sampling so as to be able to visualize the particle size distribution [121]. The development of Scanning Mobility Particle Sizer (SMPS) has provided us with a valuable tool for analyzing particle size distribution and total particle concentration in almost real-time and does not involve any prior assumptions or disadvantages like losing the adsorbed organic on soot surfaces [125]. While significant number of previous research efforts have focused on soot particle size measurement in premixed flames [125] [126] [127] [128] by achieving probe sampling using an inert gas followed by analysis, less literature available about particle size investigation in a diffusion flame. Burtscher et al. [129] and Hepp et al. [130] carried out probe sampling from methane diffusion flame by means of quartz microprobe attached to a glass capillary tube for extracting samples and diluting it with inert gas to analyze the size distribution. This was followed by the works of Kasper et al. [131], who utilized similar technique for measuring

particle concentration from metal precursor seeded co-flow diffusion flame. Zhao et al. [125] refined this experimental methodology to collect samples from a laminar flame and used SMPS to determine the particle size distribution that has successfully been utilized in many premixed flames, thereafter. A key issue to address in probe sampling is potential particle loss by means of particle-particle coagulation or diffusive wall losses [132] [133]. Particle sampling without dilution could result in an estimated 10% particle loss as a result of coagulation in first 20 miliseconds [125]. Dilution also ceases any residual chemical activity in the sampling tube effectively, thus preserving the constitution as well as the size distribution in the sample [125]. Siegmann et al. [134] have observed that despite the impact of tube on the downstream flow, there is no impact on the collected sample when compared to another sample collected by means of a less intrusive probe. Kazemimanesh et al. [135] characterized soot nanoparticle formation in a laminar methane jet diffusion flame using a multi-stage dilution system. This work demonstrated the influence of dilution ratio on impacting agglomeration and identified the existence of a critical dilution ratio beyond which the particle size and concentration becomes independent of the dilution ratio. As counterflow methane flame provides greater control over the spatial temperature distribution with temperature peak lying somewhere between the two burners, it is better capable of analyzing the particle growth over a larger temperature range and gradient.

Chapter 3

Effects of Iron pentacarbonyl additive on counterflow methane and ethanol flames[1]

3.1 Overview

Addition of metallic precursors to flames deserves interest due to their potential ability to catalyze methane and ethanol combustion by means of supplemental gas phase and surface reactions**.** A counterflow flame burner is utilized to spatially characterize and analyze the emissions from iron pentacarbonyl borne ethanol and methane combustion. Samples of the flue gases are obtained from these laminar and planar flames and are quantified using gas chromatography (GC) and Fourier-transform infra-red (FT-IR) spectroscopy, while solid particles are examined through x-ray diffraction (XRD). Measurements from ethanol and methane flames are compared and analyzed, in order to investigate the role of metal particles derived from iron pentacarbonyl. Experimental data demonstrate, in both flames, a significant influence of the additive on combustion emissions, such as NO and soot precursors. The addition of iron pentacarbonyl is found to be more effective in restricting soot precursors in methane flames as compared to ethanol flames. An enhanced production of acetaldehyde in the ethanol flame is believed to result in changes of the emission profiles.

[1]The content of this chapter has been published as:

Raj A., Pan K., Qi H., Zhu H., Wen JZ., Croiset E. "Effects of an Iron Pentacarbonyl Additive on counterflow methane and ethanol flames". *Energy & Fuels*, vol.29, no.8, pp. 5361-5371, 2015

3.2 Introduction

Iron pentacarbonyl [$Fe(CO)_5$], has long been used as an iron precursor for aerosol flame synthesis of iron catalysts due to its high vapor pressure. While previous studies have demonstrated a decline in soot levels and enhanced fuel combustion, most of these works, have focused on the end products without analyzing the process of decomposition of the precursor and the interaction of iron with reaction intermediaries, which affects the final products. The major objective of this work is mapping the effects of $Fe(CO)_5$ on soot precursors, CO and NO formation in both the radial and axial directions. This will be subsequently utilized to illustrate the role of $Fe(CO)_5$ in emission reduction. Ethanol and methane are chosen due to the simplicity of their chemical structures and the availability of their detailed combustion mechanisms. The studies on these fuels will also provide a comparative assessment of the soot and NO suppression potential of iron pentacarbonyl in higher carbon, oxygenated vaporized hydrocarbon fuel against a single carbon, gaseous hydrocarbon fuel. A porous counter flow burner is chosen due to its capability of producing a stable, two-dimensional, laminar flame [109]. This configuration enables the user to explore the impact of precursor injection both from the fuel as well as from the oxidizer side. A circular burner ensures that the flame is axisymmetric and that the species concentration or temperature can be analyzed as a function of the axial distance.

3.3 Experimental setup and operating conditions

Counterflow burner system (McKenna flat flame burners), shown in Figure 3.1, consists of two opposing inlet ports separated by a distance of 20 mm that are enclosed with porous sintered bronze matrix. This matrix is composed of two coaxial cylinders: an inner cylinder of diameter 60.4 mm and outer cylinder of diameter 73.4 mm [136]. The lower inlet has been custom developed to have a central port of outer diameter 1/8 inch for the injection of precursor.

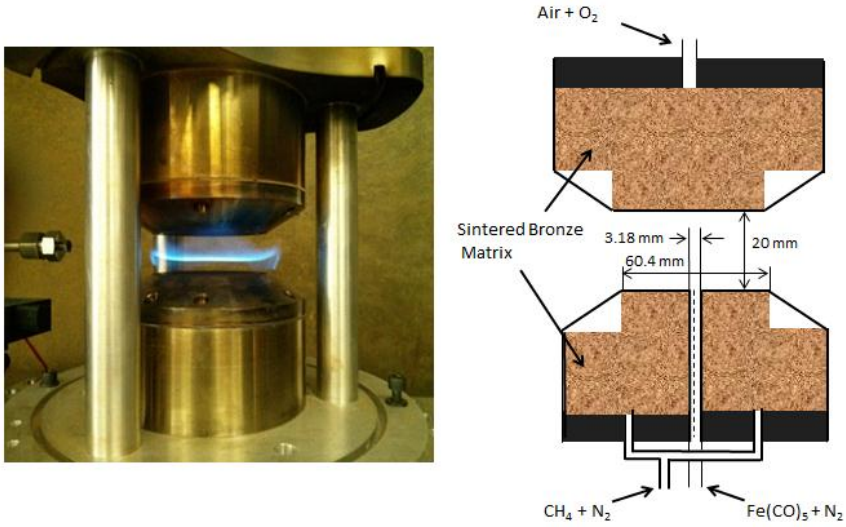

Figure 3.1: Counterflow burner assembly

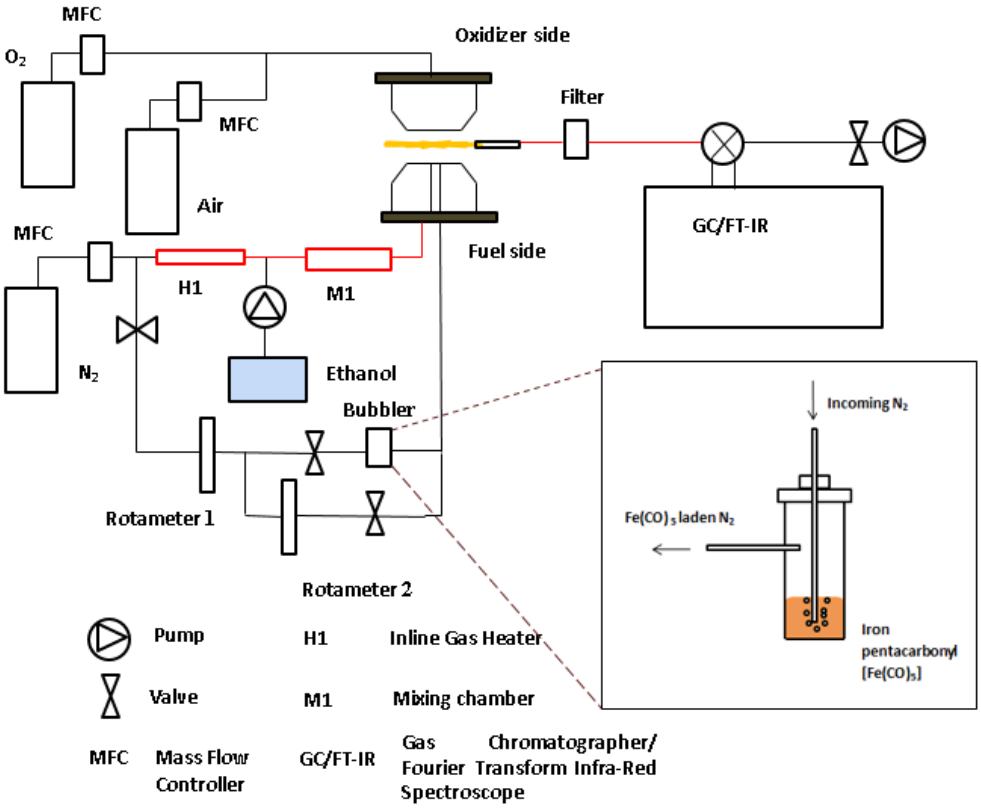

Figure 3.2: Experimental setup for counterflow flame analysis

Figure 3.2 describes the experimental setup used in this study. The methane fuel was directly sent from the cylinder to the counterflow burner apparatus while in the case of ethanol inline heaters were required to vaporize the fuel and mixing chambers were used to mix with nitrogen. The flow of O_2 and compressed air was sent through the top burner and regulated by a mass flow controller (MFC). A silica microprobe was utilized for periodic sampling from the flame and its adjacent locations by means of a pneumatic pump. N_2 was supplied along with the fuel from the lower burner. The flow of N_2 from the cylinder was controlled by a MFC. Thereafter, the flow was split into two parts: 1) the main line transporting the fuel directly to the burner in the case of methane and through a heated gas line and mixing chamber in the case of ethanol while; 2) the subsidiary line bleeds some amount of nitrogen through the bubbler so as to carry the catalyst directly into the flame through a concentric tube in the lower burner. The bubbler containing the catalyst precursor, as shown in the inset in Figure 3.2, was placed in a water bath and connected in parallel to a flowmeter while both of these were connected in series to another flowmeter (see Figure 3.1). This was done in order to regulate the N_2 flow into the bubbler while keeping the total N_2 flow in the subsidiary line constant. The partial pressure of iron pentacarbonyl was established from equation (3.1) [137] and was constant at a particular temperature.

$$log_{10}p\ (mm\ Hg) = -(2096.7)/T + 8.4959 \qquad (3.1)$$

Counterflow flames are usually characterized by means of the flow strain rate which is the normal gradient of the normal component of the flow velocity. It is the inverse of the characteristic flow time in this counterflow configuration and is defined by the following relation (3.2) [138]:

$$a = 2\frac{|V_{fuel}|}{L}\left(1 + \frac{|V_{ox}|\sqrt{\rho_{ox}}}{|V_{fuel}|\sqrt{\rho_{fuel}}}\right) \qquad (3.2)$$

where 'a' represents the strain rate on the fuel side (s^{-1}), 'L' is the distance between the two ports (20 mm), 'V_{fuel}' and '$V_{oxidizer}$' are the fuel and oxidizer velocities (cm/s) at their respective boundaries , '$\boldsymbol{\rho}_{fuel}$' and '$\boldsymbol{\rho}_{oxidizer}$' are the respective densities (g/cm^3) of the fuel and

oxidizer stream. Since the flame structure is of significant importance in counterflow configuration and emission measurements, it is important to characterize the Reynold number. For this study, all flames were studied as laminar flames which have Reynolds number less than 400. The Reynold numbers of the fuel and oxidizer streams were calculated from the relation (3.3):

$$Re = \frac{\rho U_{stream} d}{\mu} \tag{3.3}$$

Here 'μ' is the dynamic viscosity of the stream and 'd ' is diameter of the burner. The stoichiometric mixture fraction 'z_f' is defined in equation (3.4), where υ is defined as the stoichiometric mass ratio of oxygen to fuel, Y_{ox} and Y_f are the mass fractions of fuel and oxidizer with the subscript 'i' specifically pointing to their respective values at the inlets.

$$z_f = \frac{\upsilon Y_f - Y_{Ox} + Y_{Ox,i}}{\upsilon Y_{f,i} + Y_{Ox,i}} \tag{3.4}$$

The diameters of the upper and lower burners are 60.4 mm while the diameter of the central tube is 3.175 mm. The parallel arrangement of nitrogen supply provides the flexibility of varying the catalyst concentration. Maintaining a constant N_2 flow in the subsidiary line ensures similar transport conditions for catalyst thus enabling a comparative study. Gas Chromatography and Fourier Transform Infrared spectroscopy are used for the measurement of species. Agilent Gas Chromatographer GC6890 and Thermo Scientific Nicolet 6700 are used for the above study, respectively. In Gas Chromatographer, thermal conductivity detector column is used to measure O_2 and N_2 while flame ionization detector column is used to detect hydrocarbon species. NO and CO are measured through FTIR. The sample line from the flame was connected to the inlet of both the instruments. The experimental operating conditions were determined in order to achieve i) a stable, laminar flame; ii) equal momentum on fuel and oxidizer side to achieve a stagnation plane close to mid-plane and; iii) a ratio of 3.77 between nitrogen and oxygen. The operating conditions used in the methane and ethanol combustion experiment are summarized in Tables 3.1 and 3.2, respectively.

Table 3.1: Inputs for the methane combustion process

	Fuel Stream		Oxidizer Stream		Precursor stream	
	N_2	CH_4	O_2	Air	N_2	$Fe(CO)_5$ (ppm)
Flow Rate (l/min)	13	1.395	3.44	10.24	0.015	
Mole Fraction	0.903	0.097	0.41	0.59	0.992547	7853
Reynold's Number	360		342		7.14	
Strain Rate (s^{-1})	17					
Operating Pressure (atm)	1					

Table 3.2: Inputs for the ethanol combustion process

	Fuel Stream		Oxidizer Stream		Precursor stream	
	N_2	Ethanol	O_2	Air	N_2	$Fe(CO)_5$ (ppm)
Flow Rate (l/min)	8.3	0.0025(liq)	2.2	12	0.015	
Mole Fraction	0.863	0.137	0.155	0.845	0.993	7853
Reynold's Number	241.45		395		7.14	
Strain Rate (s^{-1})	12.21					
Operating Pressure (atm)	1					

3.4 Results

3.4.1 Methane combustion

The bubbler containing the precursor is maintained at a temperature of 0^o C which corresponds to the mole fraction of iron pentacarbonyl to be 7853 ppm in the carrier gas. The sampling domain includes the volume between the two flat inlets, as shown in Figure 3.1 and is assigned polar coordinate with origin being at the central tube in the lower burner for

analysis. The measurements of species and temperature are primarily carried out at different points in the axial direction. The injection of catalyst from a central tube causes its concentration to be non-uniformly distributed in the radial direction thus necessitating radial measurement. A silica microprobe (inner and outer diameter 0.2 mm and 0.34 mm, respectively) is placed at various positions in the flame for the collection of the sample with a sampling time of 15 minutes. A Type-K thermocouple (Nickel-Chromium/Nickel-Alumel) is used for temperature measurement. The particles collected from the flame location, by means of a glass plate, are also analyzed by means of x-ray diffraction (XRD).

Methane combustion is normally characterized by low soot formation and high NO_x concentrations. The location of the luminous zone of the methane flame, as observed visually, was taken to be the flame location. This flame location was averaged through multiple measurements and was found to be 8.51±0.3 mm from the fuel inlet, with the 0.3 mm being considered the flame thickness. A significant change in flame color from blue to bright yellow along with visible thickening of the flame to around 0.7 mm and large number of orange particles was observed under catalytic conditions. This change in color of the flame is depicted in Figure 3.3. Among soot precursors, C_2H_2, C_2H_4 and C_2H_6 are the prominent species which were measured in the present setup using Gas Chromatographer (GC). As these species are the building blocks of aromatic ring formation process from small aliphatics which is the rate determining step in soot formation [139], loss of these species eventually slows down the soot inception process. Figure 3.4 indicates that emissions of these C_2 species were reduced by 80%-95% in the presence of $Fe(CO)_5$, as compared with the non-catalytic combustion data, downstream of the axial locations of 5 mm up to the flame, although no significant difference in C_2 concentrations was observed from the fuel port to an axial location of 4 mm. The peak values of these gaseous species were also detected to be 2~2.5 mm lower than their previously measured positions under combustion without precursor. In addition, oxygen availability increases on the fuel side under catalytic conditions, which might cause C_2 species to be completely oxidized at an earlier location.

Figure 3.3: Methane flame under (a) non-catalytic; (b) catalytic conditions

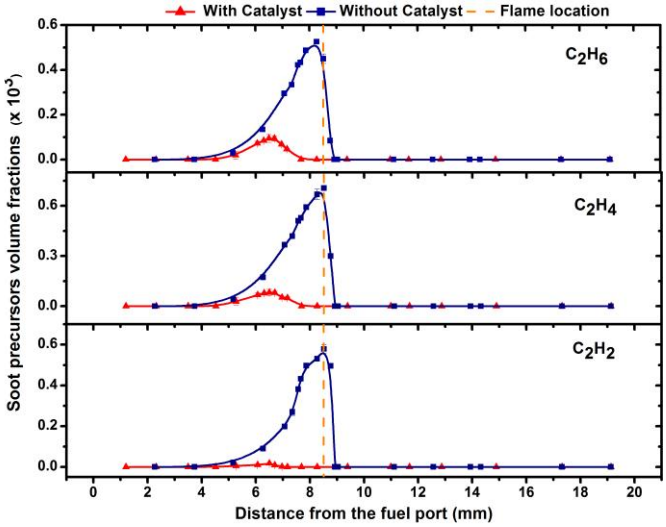

Figure 3.4: Soot precursors profiles in methane combustion at r = 0 mm

Figure 3.5 depicts the profiles of CO, methane, O_2 and NO along the central axis [A]. A significant reduction in CO mole fraction was observed along with slight shifting of peak value position at an upstream location, as shown in Figure 3.5(a). The CO concentration under catalytic conditions is an outcome of the CO formed due to the decomposition of $Fe(CO)_5$ and that produced as a result of combustion. From the methane profile in Figure 3.5(b), it can be found that under catalytic conditions, methane consumption is initiated at an upstream location closer to the fuel port while its most enhanced consumption is occurring downstream of 4 mm. Relatively more O_2 is present towards fuel side while less O_2 exists at the oxidizer side, which also corresponds to an opposite trend in the N_2 profile in catalytic conditions as compared to the non-catalytic conditions as seen from Figure 3.5(c).

[A]FT-IR calibration and NO measurement was done in collaboration with Masters student Huixiu Qi. C_2 species (soot precursors) measurement was done in collaboration with Masters student Kang Pan.

The oxygen concentration gradient from the oxidizer to the fuel burner is also found to be much more gradual in the case of catalytic combustion than in non-catalytic combustion. The increase in oxygen concentration, under catalytic conditions, near the flame location on the fuel side is probably induced by excess oxygen getting diffused on the fuel side as a result of enhanced consumption of fuel occurring at an upstream location as well as due to the heterogeneous recombination of adsorbed O radicals on the surface of catalyst particles [88].

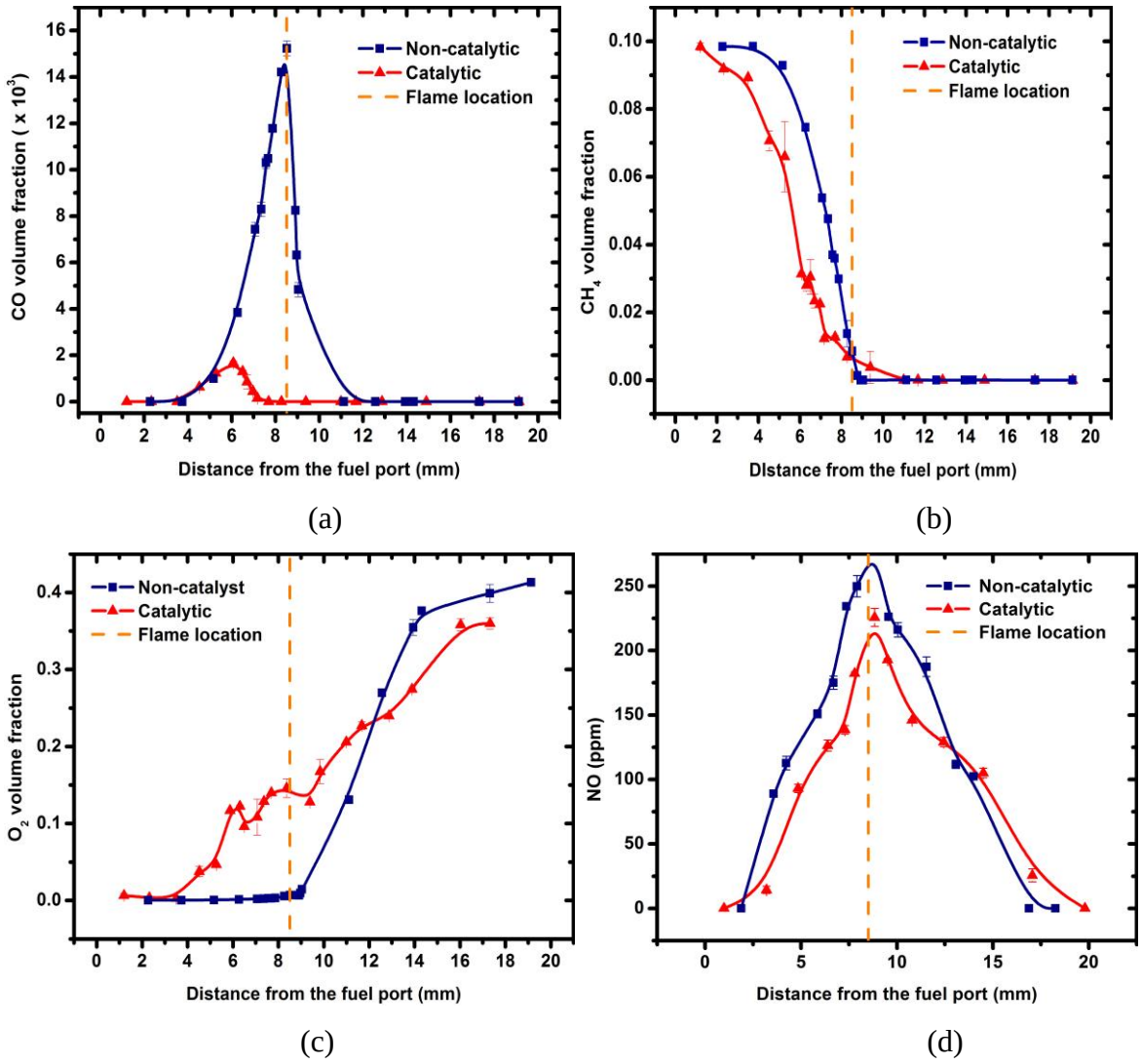

Figure 3.5: (a) CO; (b) CH_4; (c) O_2 and (d) NO profiles at r = 0 mm in methane combustion

In Figure 3.5(d), it was observed that the NO concentration reaches its peak at the flame, where the maximum temperature would be present. Under the influence of the precursor, a decline of around 15-20% was observed in the peak value of NO just above the flame with the addition of precursor; however, this decline in the NO concentration, under catalytic conditions, withers off gradually at locations closer to the fuel and oxidizer ports.

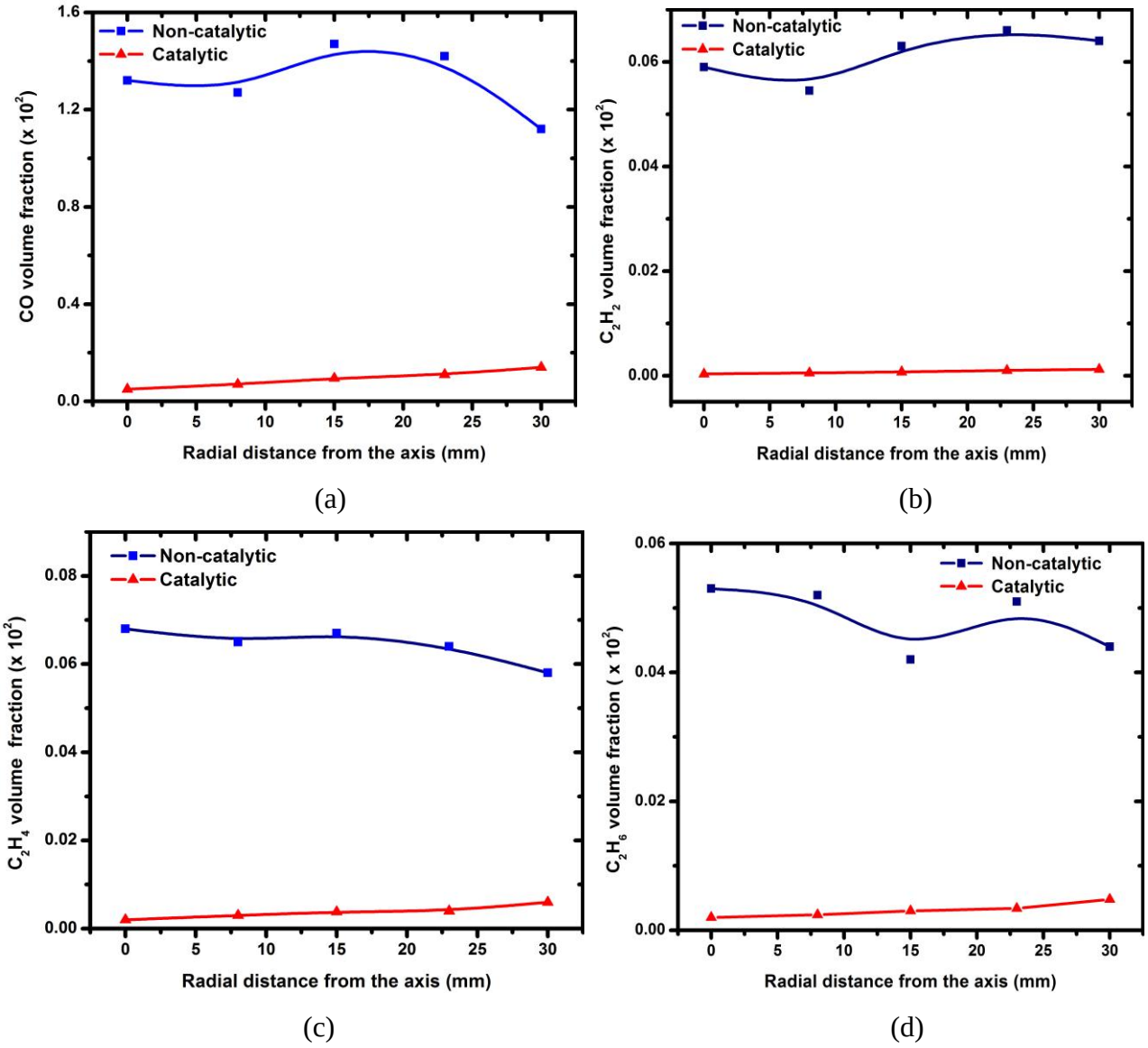

Figure 3.6: Gas emissions in radial direction measured from the catalytic and non-catalytic combustion in methane combustion at the flame location (8.51 mm)

Figure 3.6 (a)-(d) are the curves showing the gas profiles of the major emissions in the radial direction measured from the catalytic and non-catalytic methane flames. The gas samples were collected at the location of the flame, i.e., 8.51 mm above the burner. In these figures, the x-axis indicates the distance between the microprobe tip and the burner central axis (defined as the zero point), and the y-axis shows the concentration of the generated emissions. Overall, the concentrations of CO and C_2 species are significantly reduced radially by the iron-containing catalysts as seen in Figure 3.6. Also it was observed that under non-catalytic conditions the above species demonstrate a non-uniform, yet significant concentration in the radial direction; however under catalytic conditions, the species concentrations are significantly reduced and remain invariant in radial direction. The radial distribution of NO at the flame is visualized in Figure 3.7. While the trends exhibited under both catalytic and non-catalytic conditions remain qualitatively the same with an initial rise followed by a decline, a maximum decline of around 15-20% was observed in the NO concentration under catalytic conditions.

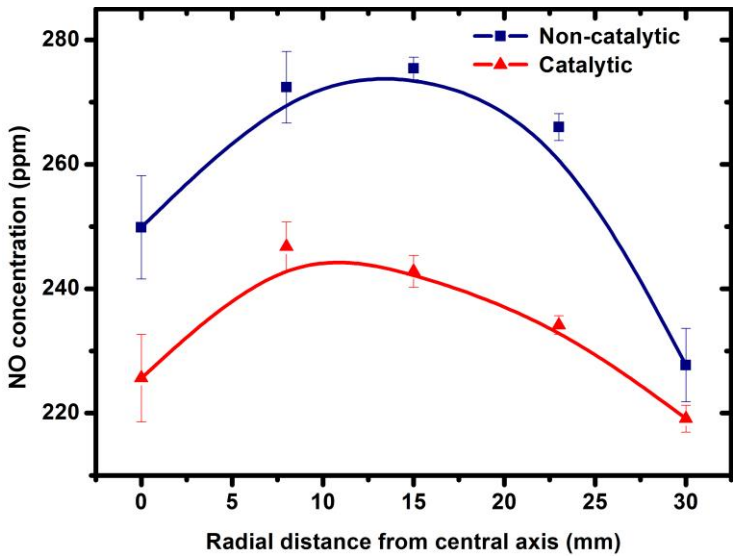

Figure 3.7: Radial profiles of NO at flame location (8.51 mm) in methane

Temperature measurement was carried out by means of a calibrated thermocouple while the radiation loss was accounted for separately as explained in the work of Roberts et al. [140].

The equivalence ratio is estimated by using the detected concentrations of methane and the oxidizer from Figure 3.5 (b) and (c). Figure 3.8 illustrates the temperature and equivalence ratio profiles across the domain at the central axis. The temperature demonstrates a gradual increase from the fuel port to around an axial distance of 3.5 mm, followed by a rapid rise thereafter up to axial distance of 7 mm. Further downstream, the gradient of temperature rise is found to decline and the temperature peak is realized just above the flame. The impact of the addition of iron pentacarbonyl precursor can be seen in terms of a decline of around 100 ^{o}C in the peak temperature just above the flame due to the additional thermal mass. An initial increase in temperature below the flame under catalytic conditions can be attributed to the combustion of fuel as a result of faster decline in the equivalence ratio due to enhanced oxygen presence on the fuel side, as shown in Figure 3.5(c). The equivalence ratio is found to decline at an upstream location under catalytic conditions; however the gradient of this decline is greatly reduced around 5 mm and the conditions for combustion (equivalence ratio ~1) are found to occur roughly around the same location as seen under non-catalytic conditions.

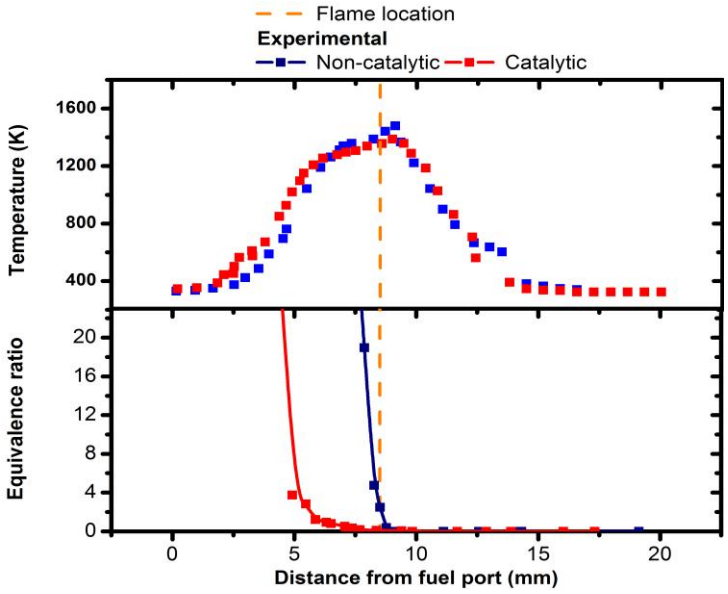

Figure 3.8: Temperature and equivalence ratio profiles at the central axis in methane combustion

3.4.2 Ethanol combustion

The most luminous zone of the ethanol flame was found at axial location of 7.91± 0.5 mm and was considered the flame location. Thickening of flame from 0.5 mm to 0.8 mm along with an enhanced consumption of ethanol was observed under the influence of $Fe(CO)_5$ as seen from Figure 3.9(a) where a steeper decline in ethanol concentration was observed on the fuel side under catalytic conditions.

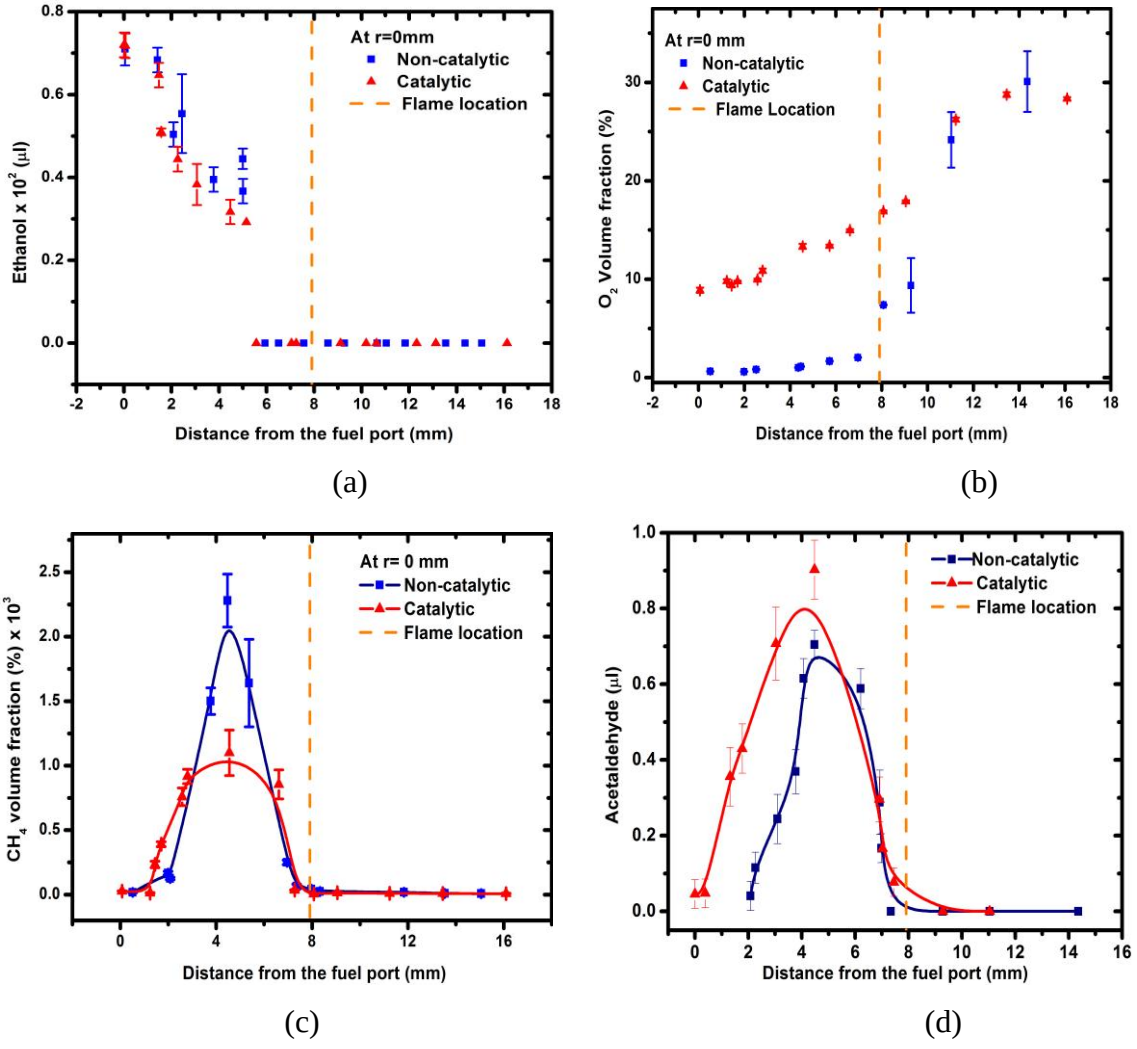

Figure 3.9: (a) Ethanol; (b) O_2; (c) CH_4 and (d) CH_3CHO profiles along the central axis of the counter-flow burner at r = 0 mm in ethanol combustion

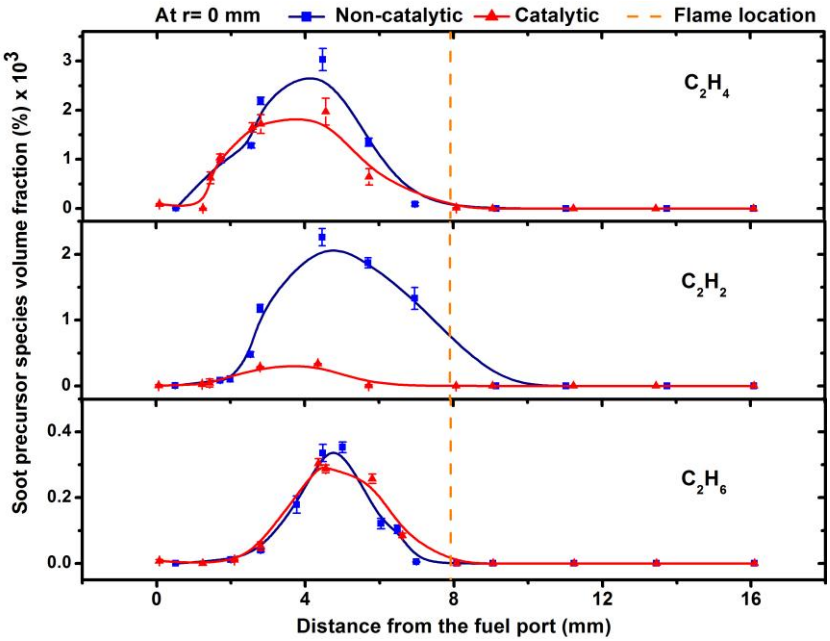

Figure 3.10: Soot precursors at r = 0 mm in ethanol combustion

Figure 3.9(b) shows the oxygen profile in the sampling domain. The oxygen concentration declines from the oxidizer port towards the flame, however, some amount of oxygen is still available close to the fuel port. Figure 3.10 shows the distribution of the C_2 species under catalytic and non-catalytic conditions. From Figure 3.10, it was observed that their evolution and consumption are primarily confined in a region below the flame on the fuel side. It is also worthwhile to point out the fact that under non-catalytic conditions, these precursors mostly reach their peak concentrations around 5 mm from the fuel burner which coincides with the complete consumption of ethanol as can be seen from Figure 3.9(a). However, the addition of the precursor causes the peak of these species to decline as well as to move upstream closer to the fuel port, even though the ethanol is still available. This shift in the peak-value plane of C_2 species towards the fuel inlet demonstrates the enhanced ethanol consumption while the decline in their absolute values is attributed to the heightened oxygen concentration on the fuel side. Figure 3.9 also shows the concentrations of methane and acetaldehyde (CH_3CHO) as observed in the products of ethanol combustion. The hydroxyl component in ethanol gives rise to oxygenated species like acetaldehyde, which sequesters

carbon precursors to develop into soot [141]. While methane shows a decline in its concentration, the acetaldehyde (CH_3CHO) concentration gets enhanced on the addition of the precursor with the peak of acetaldehyde curve, which lies around 5 mm from the fuel port under non-catalytic conditions, shifting upstream. The increase in the catalytic trend for acetaldehyde also coincides with the initiation of ethanol consumption under catalytic conditions. This might suggest the activation of other pathways in the ethanol combustion reaction on the addition of the precursor as will be explained later. The peak concentration of methane was found to be at an upstream location (around 4.5 mm) than those of the C_2H_2, C_2H_4, C_2H_6 species indicating possible dehydrogenation of methane to methyl radicals, followed by their recombination to form higher carbon species. Due to the non-uniformity of the catalyst concentration in the radial direction, as the result of central injection, it is important to analyze the species distributions in that direction. Figure 3.11 shows the NO profile at the central axis. With the addition of catalyst precursor, a decline in the NO peak concentration was observed just below the flame, which is followed by a significant decline in the concentration in the above-flame region.

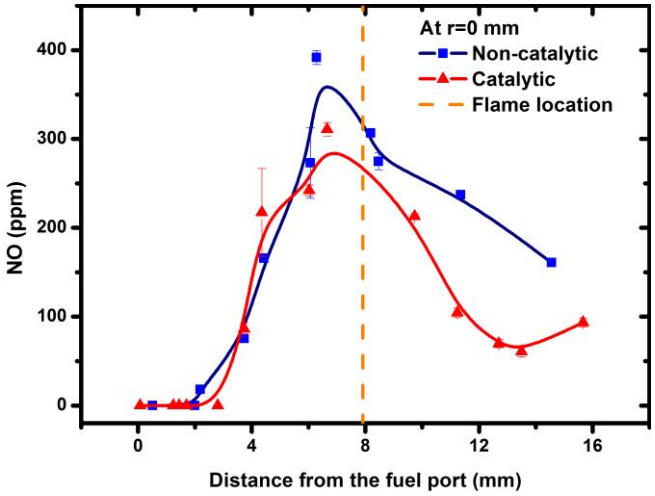

Figure 3.11: NO profles in ethanol combustion at r = 0 mm

Figure 3.12 exhibits the concentration profiles of various species (ethanol, CH_4, C_2H_2, C_2H_4) in the flame along the radial direction and at the axial distance of 4.55 mm. Under non-catalytic conditions the variation in the radial direction is not significant up to 20 mm.

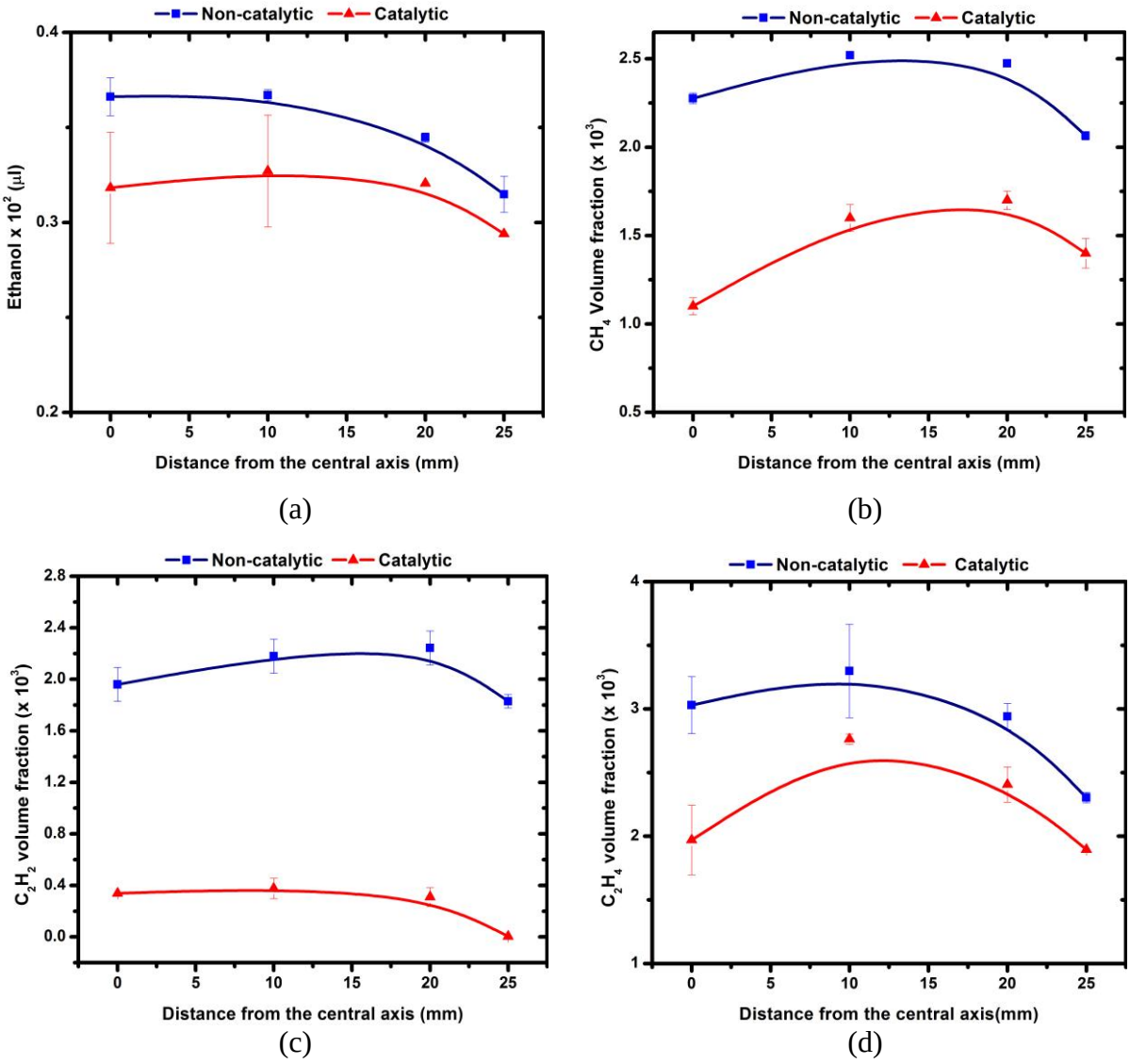

Figure 3.12: Profiles of (a) Ethanol; (b) CH_4; (c) C_2H_2 and (d) C_2H_4, in the radial direction at axial location of 4.5 mm from the fuel inlet

However, beyond it, the concentration shows a minor decline as observed from this figure. Under catalytic conditions, the species concentrations are considerably reduced. In CH_4 and C_2H_4, an initial increase in radial direction is followed by eventual decline which could be due to non-uniform spread of the centrally injected precursor.

3.5 Discussion

A symmetric planar flame was established at respective axial positions for methane and ethanol in order to map the axial and radial profiles of various chemical species. It was observed that, the addition of the $Fe(CO)_5$ precursor turned the blue flame into uniformly orange, which indicates the formation of particles in the flame and their transportation was radially outwards along with the flow. In order to identify the composition of as-produced particles, XRD analysis was performed. The results are depicted in Figure 3.13 and it was found that Fe_2O_3 dominated other compositions in the sample collected from the flame location by means of glass slides connected to the positioning device. While this is validated by the findings of several other research groups that detected Fe_2O_3 to be the chief constituent of the particles in the presence of excess oxygen, it is quite likely that the particles formed at upstream locations, having lesser presence of oxygen, comprise of Fe_3O_4 or Fe [76] [77] .

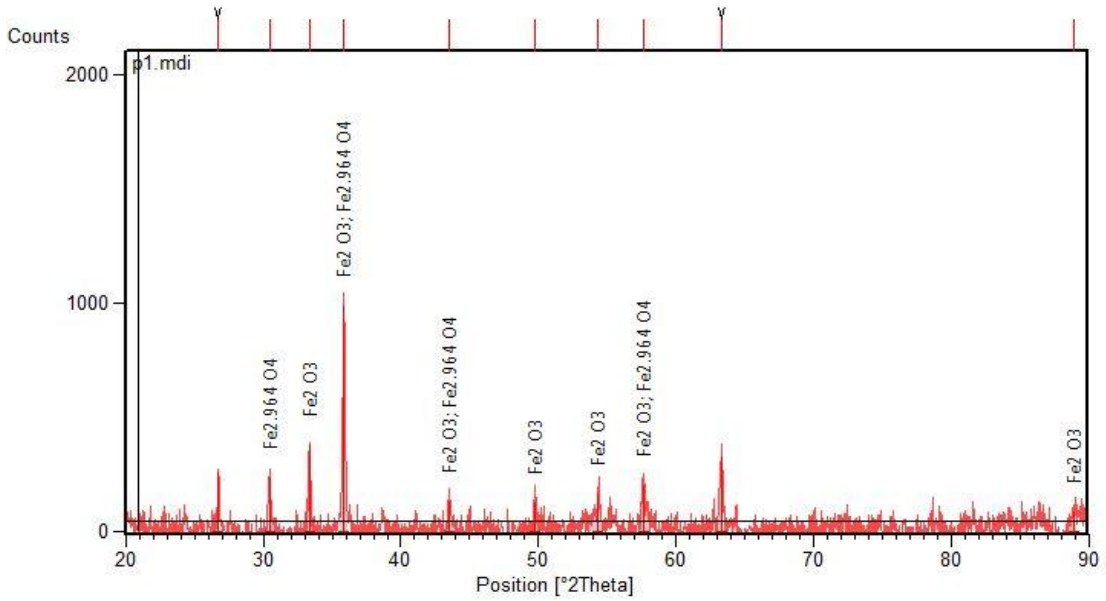

Figure 3.13: XRD data of the collected powder from the flame

The decomposition of iron pentacarbonyl precursor occurs below the flame, at relatively low temperatures as suggested by Wen et al. [102], leading to the formation of iron clusters,

which result in iron nanoparticles. The oxidation of iron to Fe_2O_3 can occur concurrently via gas-phase oxidation of iron atoms and clusters as well as via surface reactions on iron particles, which both can result in Fe_2O_3 particles, as described in references [91] [90] [95] [103] [104] [142]. The decline in soot precursor species, as observed previously, can therefore be directly associated with the iron oxide particles present in the flame, as suggested by Reichert et al. [88] and Fennell et al. [89]. Iron oxide (Fe_2O_3) particles are able to provide a surface for the dissociative adsorption of O_2 and readily transfer the dissociated atomic oxygen, present at the surface and also from the sub-surface level, to the interfaces of soot and catalyst due to their high lattice mobility [88]. It provides an additional surface mechanism for fuel oxidation apart from the existing gas phase mechanism as proposed by Lee et al. [143] and also shown in Figure 3.14 for methane. This additional surface oxidation pathways, usually occurring at lower temperature, lead to faster consumption of fuel as seen from methane and ethanol profiles in Figures 3.5(b) and 3.9(a).

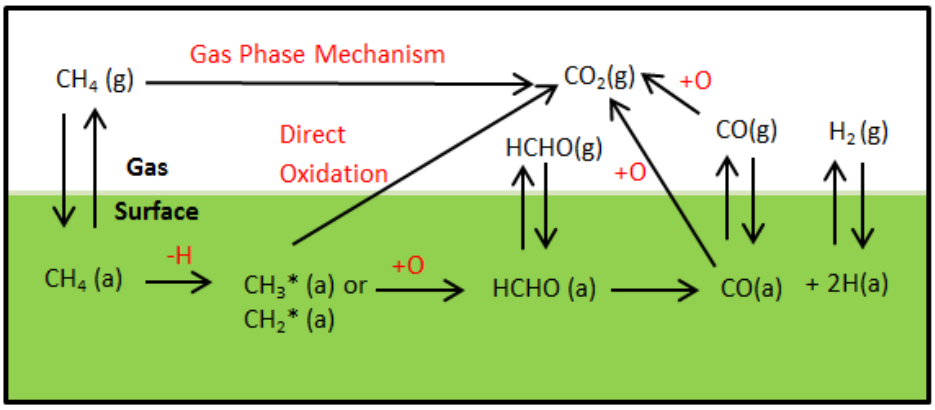

Figure 3.14: Additional pathways available for methane oxidation under heterogeneous surface mechanism in methane combustion [143]

In the case of methane combustion, initially the methane quantity close to the fuel port remains almost invariant in the catalytic and the non-catalytic process, as shown in Figure 3.5. This is possibly due to the lower temperature close to the fuel end, being insufficient to initiate precursor decomposition as suggested by Wen et al. [102], which keeps the conditions

effectively the same as in the non-catalytic combustion. The precursor decomposition is initiated closer to the flame with more particles being formed in that region as observed visually. The addition of precursor was found to initiate the early consumption of methane. The formation of C_2 species follows the possible mechanism involving the combination of methyl radicals in the presence of a third body 'M' to form higher carbon species [18] as shown in Figure 2.1. This process normally involves radicals like H, O and OH, which help the hydrogen abstraction from methane to form the methyl radical. This methyl radical then participates in a trimolecular reaction with a third species to produce larger hydrocarbons. This process is quite slow and is therefore the rate determining step [18] in the gas phase reaction. Furthermore, C_2H_6 loses its H atoms as a result of abstraction by OH radical in presence of a third species 'M' to form unsaturated compounds C_2H_4 and C_2H_2 which eventually form carbon monoxide [103]. As stated by Rumminger et al. [91] , the iron species also act as scavengers for the H, O and OH radicals thereby causing their concentration to decline. This factor along with the catalytic oxidation of methane over Fe_2O_3 particles severely constrains the formation of species like C_2H_6 , C_2H_4 and C_2H_2, and ultimately CO as observed from Figures 3.4 and 3.5.

In the case of ethanol combustion, the alcohol molecule can undergo various pathways [33] as shown in Figure 2.2. One of these pathways involves dehydration under the influence of third body species 'M' to produce C_2H_4, which thereafter loses H atom as a result of abstraction by H, OH and O radicals and produces C_2H_2. Another main pathway involves the oxidation of ethanol to aldehyde by means of H, OH and O radicals, followed by its decomposition into methyl radicals, which on recombination with themselves form C_2H_6 under the influence of third body 'M' reactions. From the results of the catalytic methane and ethanol combustion experiments, a faster consumption of the fuel was observed as compared to non-catalytic case along with considerable presence of oxygen on the fuel side, thereby letting excess oxygen diffuse to the fuel side, as seen from Figure 3.5 and 3.9. The oxygen concentration is much higher in the case of ethanol combustion as compared to that of methane which is probably due to the decomposition of ethanol to produce oxidizing species

including OH, O, H_2O which combine to form oxygen [144] under catalytic conditions apart from the diffusion of oxygen on the fuel side due to faster combustion of the fuel under catalytic conditions. Another reason for increased oxygen presence on the fuel side is the dissociative adsorption of NO and CO on Fe_2O_3 particles which lead to recombination of dissociated O species, adsorbed on catalyst, as specified in the works of Reichert et al. [88].

Under catalytic conditions, the decline was most prominent in the case of C_2H_2 followed by C_2H_4 and very minimal in terms of C_2H_6. Reduced formation of C_2 species also signifies an enhanced combustion efficiency achieved under the catalytic conditions. Also an enhanced production of aldehyde (CH_3CHO) and decline in methane species were observed on the addition of the precursor. These indicates that under the influence of the precursor, the second pathway (see Figure 2.2), involving the oxidation of ethanol to aldehyde by means of radicals, gains prominence. From Figure 3.9(d), it could also be seen that the aldehyde formation gets initiated much closer to the inlet port. The most plausible explanation is the enhanced decomposition of ethanol into acetaldehyde, since this path is potentially very viable [144] as well as due to the availability of excess surface area, as a result of iron oxide particle inception and growth, which enhances adsorption of the gas-phase reactants and their surface oxidation through a heterogeneous reaction mechanism. The presence of O_2 close to the fuel port, as seen from Figure 3.9(b), encourages the conversion of ethanol to CH_3CHO as visualized in Figure 2.2. This pathway thus dominates other possible pathways and leads to enhanced formation of CH_3CHO from ethanol. The further transformation of CH_3CHO to methane through methyl radical was reduced as a result of scavenging of the H, O and OH radicals, while the formation of C_2H_6 from methyl radical was not particularly affected as it depended only on the third body species ‘M’ but not the radicals. In terms of NO distribution, the peak value was observed just above the flame under both fuels and was found to be reduced with the addition of the catalyst precursor. This can be attributed to the reduced peak temperatures experienced due to the additional thermal mass present in the form of iron oxide particles as well as due to the catalytic nature of iron oxide particles [89] .

Overall, the addition of iron pentacarbonyl seems to be more effective in restricting soot precursor species in methane combustion as compared to that in ethanol. This is because in the case of ethanol combustion, various pathways contribute to the formation of these species, while lesser number of pathways is responsible for the production of these species in methane combustion, as seen from Figure 2.2. Significant decline in NO peak close to the flame under catalytic conditions was observed in both fuels. As the flame lies close to the interface of the iron catalyst laden fuel and oxidizer stream, considerable amount of Fe_2O_3 is produced at this location as shown by the XRD results of the collected sample in Figure 3.13. The formation of Fe_2O_3, as pointed out by Reichert et al. [88] and Fennell et al. [89] , provides surface sites for dissociative adsorption of O_2, which is later transferred to soot-catalyst interface to enhance soot oxidation as well as form complexes to facilitate the dissociation of NO and its transformation to N_2. Consequently, the best NO reduction results were observed at regions close to the flame on the fuel side. Also, the decline in the peak flame temperature by around a hundred degrees on the addition of $Fe(CO)_5$ as shown in Figure 3.8 would also result in the reduction of thermal NO formation; however, the catalytic effect of Fe_2O_3 particles in NO is apparent from the considerable decline under catalytic combustion of methane at axial location of 6.5 mm, where the temperature under catalytic and non-catalytic conditions remain the same. In both fuels, the insignificant variance among species concentration in the radial direction in the non-catalytic cases could be explained due to diffusion of fuel outwards in the radial direction and possible reaction with the surrounding air outside the sampling domain. Under catalytic conditions, the concentration becomes significantly reduced with the distribution showing negligible variance in the radial direction thus highlighting uniform distribution of catalyst.

3.6 Uncertainty in experimental analysis

Probable sources of errors in the measurement include i) inherent limitations of the measuring instruments for the species (GC, FT-IR spectroscope, mass-flow controllers), spatial distances (Vernier Calipers) and temperature (thermocouple); ii) inaccuracies

associated with the sampling technique and iii) perturbations caused due to insertion of the probe into the flame and due to formation and deposition of particles on the microprobe under catalytic conditions at regions close to the flame.

The calibration results of the GC and FTIR demonstrated the maximum error of 4% and 5%, respectively. The flow controllers and rotameters have an associated system error of 1% as compared to the experimental results, the K-type thermocouple has an error band of +/- 2.2^{o} C while the digital vernier calipers are accurate up to 0.01 mm. In order to address the risk of blockage in the microprobe itself due to the formation of iron oxide particles, extensive sampling was carried out with even larger sampling periods than that used in the study. Consistent results with acceptable error margins were achieved, under catalytic conditions, using a sampling time of 30 minutes; however, a lesser sampling time of 15 minutes was utilized in the study. The perturbation in the flame could possibly be a source of error as the outer diameter of microprobe was of the order of flame thickness.

3.7 Summary

The influence of introducing iron pentacarbonyl precursor into a fuel combustion process in a counterflow arrangement was investigated in terms of emissions. The fuels analysed include methane and ethanol, the first one being one of the most commonly used hydrocarbons and the other one being the most commonly used renewable fuel, when derived from biomass. The results depicted excellent uniformity in the distribution of the precursors in the reaction zone indicating the merit of this configuration in conducting catalyst based fundamental combustion research. The results indicate that, while the iron pentacarbonyl additive enhances combustion efficiency and depicts exceptionally good results in suppressing soot precursors and NO especially in methane combustion, a relatively weaker effect was observed in ethanol combustion. The enhanced catalytic activity due to the precursor addition is likely attributed to the gas-phase chemistry of iron species that act as scavengers to consume reaction propagating species as well as to the heterogeneous reactions on iron oxide (Fe_2O_3) particles. These findings are also significant for evaluating the

effectiveness and feasibility of this catalyst injection method in industrial applications, as the conclusions reveal that the chemical additive ($Fe(CO)_5$) injected into the fuel stream through the central port can be well transported to the whole flow field closer to the flame.

Chapter 4

Numerical analysis of hydrocarbon and nitric oxide emission reduction from iron pentacarbonyl loaded counterflow methane flame

4.1 Overview

The present work focuses on deepening the understanding of interactions of iron species and key emissions (soot precursors and NO formation) pathways. It explores underlying issues, which are, otherwise, difficult to analyze by means of experimental analysis including investigating the role and ultimate fate of iron species through the analysis of kinetics of key iron species reactions in the flame and exploring their impact on the emission level. Numerical model is developed using the Computational Fluid Dynamics (CFD) techniques and verified through experimental and literature data. A sensitivity analysis is carried out to understand the influence of input parameters, such as iron pentacarbonyl concentration and fuel fraction on emissions. The simulation results demonstrate a proportional decline in most C_2 and NO species with increasing the concentration of precursor $Fe(CO)_5$. The decline in NO and C_2H_2 emissions is found to demonstrate an increase with increasing the fuel fraction. Beyond a certain threshold the enhanced fuel fraction enlarges the radical pool sufficiently enough to overwhelm the additional iron reaction pathways responsible for radical scavenging and consequently the emission reduction declines. Higher temperatures result in activation of new iron pathways, which lead to a higher emission reduction.

4.2 Introduction

Challenges exist in understanding the formation mechanism of iron oxide species in their condensed phase counterparts and their roles in emission reduction. In the literature, most research has focused on the inhibition effects of $Fe(CO)_5$ on the flame speed, the in-flame nanoparticle formation process and experimental soot reduction using fuel doped iron precursors in engines. A better understanding of the interplay between the formation of iron oxides and the methane combustion mechanism will help develop better correlation between the operating parameters for combustors and optimal outputs in terms of fuel efficiency and emissions. Two key outcomes are expected out of precursor assisted combustion: first, the combustion efficiency may be changed due to the change of the fuel/air ratio and mixing of different flow patterns (axial and radial flow) and secondly, catalytic combustion may be altered significantly due to the catalytic nature of the gas phase iron, iron oxide particles and iron clusters. While the flame inhibiting characteristics of iron pentacarbonyl decomposition in flames have been documented for premixed H_2/O_2 flames [105], a comprehensive understanding of their interdependency along with the impact on emissions is lacking in the case of hydrocarbon fuels based diffusion flames.

While the potency of iron pentacarbonyl in achieving C_2 and NO species reduction was established through experimental analysis of the emissions and flame structure using a counterflow burner as described in Chapter 3, the limitations of that study include its inability to distinguish the emission reduction due to gas phase reactions from that due to heterogeneous catalytic reactions between iron species and hydrocarbon combustion intermediates and products. Due to the unique geometry of the counterflow burners and the location of the flat flame being close to the mid-plane (lying at an axial distance of 10 mm), it is observed that while the formation of particles, responsible for heterogeneous catalysis, is mainly restricted to the flame region in the experimental study, the gas phase iron species is predicted to occur at upstream locations from the modeling studies in literature. As a result, it remains important to assess the impact of both gas phase and heterogeneous reactions separately. Experimental analysis was limited to Gas Chromatography and Fourier

Transform Infra-Red Spectroscopy in Chapter 3 with the absence of quantitative diagnostics for the iron species measurement. The present numerical study focuses on bridging this gap through the analysis of formation of emissions, iron, iron oxide and hydroxide species and developing an understanding of their mutual dependency in a precursor laden counterflow methane diffusion flame. This study utilizes the available gas phase mechanisms for methane combustion, iron pentacarbonyl decomposition, iron clusterization and iron species formation without considering the heterogeneous reactions between iron and absorbed hydrocarbons.

4.3 Numerical modeling

Two numerical models are developed for the non-catalytic and catalytic cases, respectively. Each has a two-dimensional axi-symmetrical steady-state geometry comprising of solid and fluid domains which incorporates mass, momentum and energy balances through continuity, Navier-Stokes and energy equations using ICEM and FLUENT CFD packages. This geometry consists of two burners separated by a distance of 20 mm and surrounding region. The lower burner has a concentric central tube for the injection of iron precursor laden carrier gas. The dimensions of the geometry are presented in Figure 4.1 while the boundary conditions, based on the experimental operating conditions, are listed in Table 4.1.

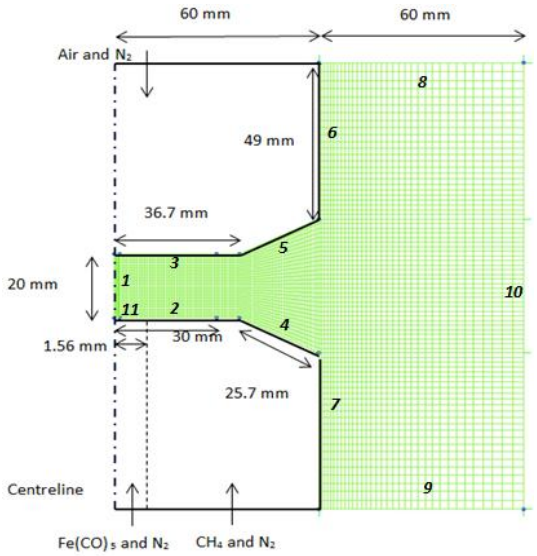

Figure 4.1: Computational geometry of counterflow burner system with meshing

Table 4.1: Inputs for the base catalytic methane combustion case with reference to Figure 4.1 labeling

	Velocity Inlet		Wall	Pressure Inlet	Pressure Outlet	Centreline
Regions	2,3,11		4,5,6,7	8,9	10	1
Temperature (K)	288.15		300	288.15	288.15 (Backflow only)	N/A
Species flow						
	Fuel Stream		**Oxidizer Stream**		**Precursor stream**	
	N_2	**CH_4**	**O_2**	**Air**	**N_2**	**$Fe(CO)_5$ (ppm)**
Flow Rate (l/min)	13	1.395	3.44	10.24	0.015	
Mole Fraction	0.903	0.097	0.41	0.59	0.9925	7853
Reynold's Number	360		342		7.14	
Strain Rate (s^{-1})	17					
Pressure (atm)	1					

Meshing is finer in the region close to the opening of both burners while relatively coarser near the surroundings. Mesh independence testing is done in order to identify and resolve any effects of numerical setup on the final results (results shown in Figure A-1 in Appendix). The minimum face area of 2.645×10^{-4} m^2 is used along with 7600 nodes and 14741 faces. The convergence criterion of 10^{-6} is used for all the residuals except for the iron species for which a residual of 10^{-5} is used due to its slow convergence rate. Boundary conditions in the two models remain the same except for the absence of iron precursor in the case of non-catalytic model. The volume flow rates of gases calculated before entering the burner system are converted to velocities and used as boundary conditions at the regions specified as velocity inlet in Table 4.1. The governing equations include conservation of mass, momentum and

energy as shown in equations (4.1), (4.2), (4.3) and (4.5), respectively. Equation (4.4) accounts for the viscosity of the gaseous mixture.

$$\frac{\partial}{\partial x}(\rho v_x) + \frac{\partial}{\partial r}(\rho v_r) + \frac{\rho v_r}{r} = 0 \tag{4.1}$$

$$\begin{aligned}&\frac{1}{r}\frac{\partial(r\rho v_x v_x)}{\partial x} + \frac{1}{r}\frac{\partial(r\rho v_r v_x)}{\partial r} \\ &\quad = -\frac{\partial p}{\partial x} + \frac{1}{r}\frac{\partial\left[r\mu(2\frac{\partial v_x}{\partial x} - \frac{2}{3}(\nabla.\vec{v}))\right]}{\partial x} + \frac{1}{r}\frac{\partial\left[r\mu(\frac{\partial v_x}{\partial r} + \frac{\partial v_r}{\partial x})\right]}{\partial r} + F_x\end{aligned} \tag{4.2}$$

$$\begin{aligned}&\frac{1}{r}\frac{\partial(r\rho v_x v_r)}{\partial x} + \frac{1}{r}\frac{\partial(r\rho v_r v_r)}{\partial r} \\ &\quad = -\frac{\partial p}{\partial r} + \frac{1}{r}\frac{\partial\left[r\mu(2\frac{\partial v_r}{\partial r} - \frac{2}{3}(\nabla.\vec{v}))\right]}{\partial r} + \frac{1}{r}\frac{\partial\left[r\mu(\frac{\partial v_x}{\partial r} + \frac{\partial v_r}{\partial x})\right]}{\partial x} - 2\mu\frac{v_r}{r^2} + \frac{2}{3}\frac{\mu}{r}(\nabla.\vec{v}) + \rho\frac{{v_z}^2}{r} + F_r\end{aligned}$$

(4.3)

$$\mu = \sum_i y_i \mu_i \tag{4.4}$$

Equation (4.5) represents the energy equation. Radiation is accounted for by incorporating the molecular radiationto the numerical model.

$$\sum \dot{m}_i'' \frac{dh_i}{dx} + \frac{d}{dx}(-k\frac{dT}{dx}) + \dot{m}'' u_x \frac{du_x}{dx} + \dot{m}''\sigma\sum_i y_i a_{p,i}(T^4 - T_b^4) + \sum h_i \dot{m}'''_i = 0 \tag{4.5}$$

The multispecies mass transport in the whole gaseous computational domain is described by equation (4.6). It solves for the fluxes of each species in terms of mole fraction. Equation (4.6) accounts for diffusion, convection and reaction source/sink term. The source/sink term is determined from the reaction kinetics of the used mechanism.

$$\frac{1}{r}\frac{\partial(r\rho v_x Y_i)}{\partial x}+\frac{1}{r}\frac{\partial(r\rho v_r Y_i)}{\partial r}-\frac{1}{r}\frac{\partial(r\rho D_{AB}\frac{\partial Y_i}{\partial r})}{\partial r}=\dot{m}''' \quad (4.6)$$

Here ρ, t, u, h, T and $\dot{m}''$ represents the density, time, velocity, enthalpy, temperature, mass flux of the bulk flow, respectively while $\dot{m}'''$ represents the mass production rate of species formed/consumed in the reaction. Subscript '*i*' relates the property to individual species in the bulk mixture while $x, Y, k, \mu, D, \sigma, a$ depict any specified spatial direction, mass fraction of individual species in bulk mixture, thermal conductivity coefficient, viscosity, diffusivity coefficient, Stefan's constant and absorption coefficient, respectively. The gas phase reaction mechanisms include: i) GRI 3.0 mechanism [24] for gas phase methane combustion for both catalytic and non-catalytic models respectively; ii) iron pentacarbonyl decomposition into gas phase iron atoms by Rumminger *et al.* [91] ; iii) their further clusterization (Fe_n with highest n=16) and subsequent reactions mechanisms by Wen *et al.* [102] for the catalytic model and; iv) interaction of iron species with reaction propagating radicals like H, O and OH by Rumminger *et al.* [91] and Wlokas *et al*. [105] for the catalytic model. Similar modeling approaches, with regard to the use of mechanisms, have been adopted in the works of Kluge *et al.* [103], Poliak *et al*. [104] and Feroughi *et al.* [142] . Their respective kinetic and transport data are also taken from the literature [91] [102] [24] . The present study restricts iron cluster size 'n' to 16 so as to reduce computational cost.

4.4 Results

4.4.1 Model validation

To ensure validity of the present model, it is compared with other models incorporating similar chemistry as well as with experimental results. Numerical modeling results for counterflow flames like that of Flame A as specified in the work of Bufferand *et al.* [145], those achieved by Sahu *et al.* [146] and those from the experimental work of Smooke *et al.* [147] are compared against the results from developed non-catalytic model incorporated with

their respective boundary conditions. The two reference models (Flame A from Bufferand *et al.* [145] and another flame from Sahu *et al.* [146]) simulated counterflow methane combustion using the GRI 3.0 mechanism.

Figure 4.2(a) highlights the comparison of temperature distribution profiles under catalytic and non-catalytic conditions achieved through the developed numerical model with both experimental and numerical results, available from literature. On comparing against the available models from Bufferand *et al.* [148] and Sahu *et al.* [146], it can be observed that the predicted profile is closely analogous to that in the literature. Figure 4.2(a) also highlights the results obtained under experimental analysis and compares it with the predicted temperature distribution profiles from the developed catalytic and non-catalytic models, simulated under the same boundary conditions. The velocities at both the burners are calculated from the known volume flow rate of the fuel into the burner. The modeling results are found to accurately predict the maximum temperatures under both non-catalytic and catalytic conditions with better agreement in the case of non-catalytic model. The difference between the measured temperature and model predicted temperature on the oxidizer side under catalytic conditions can be attributed to the hot flame-synthesized particles escaping to the oxidizer side resulting in higher temperatures being measured. The distribution trends of major species, predicted using the developed model and experimental results from Smooke *et al.* [147], also demonstrate a high degree of similarity as shown in Figure 4.2(b).

In order to validate the combined iron mechanism used in the developed model, it is compared against the methane combustion model containing 100 ppm of iron pentacarbonyl precursor, as proposed in Rumminger *et al.* [91] in which the iron reaction mechanism used does not account for iron clusterization. Figure 4.2(c) shows the iron species distribution trend predicted by the present model to those illustrated in the literature. The results in Figure 4.2(c) demonstrate extensive qualitative similarity between the simulation and the available literature results, highlighting the effectiveness of the combined mechanism in iron species prediction.

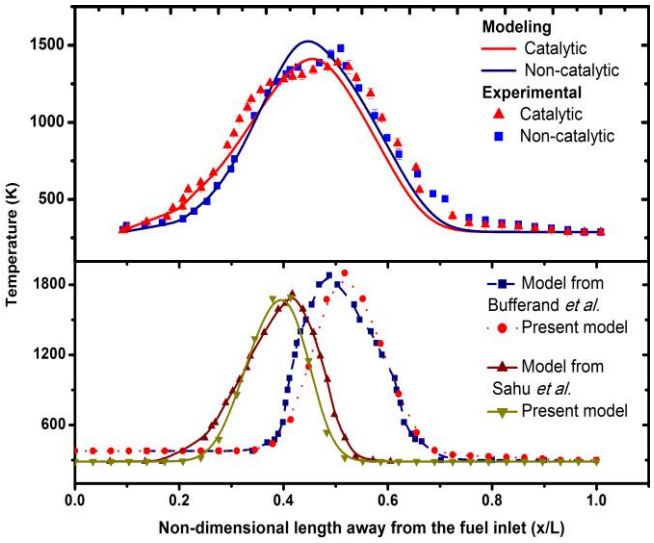

(a)

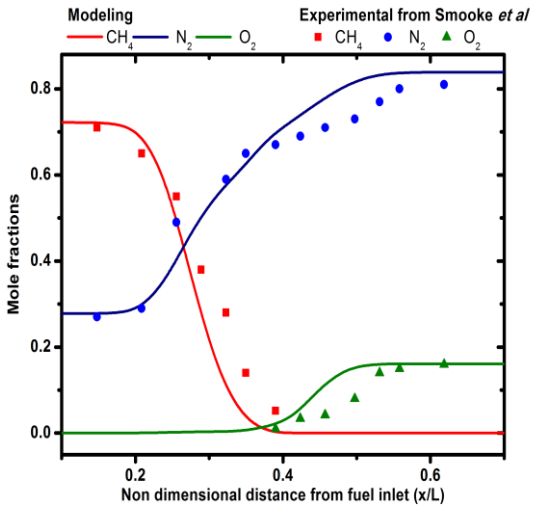

(b)

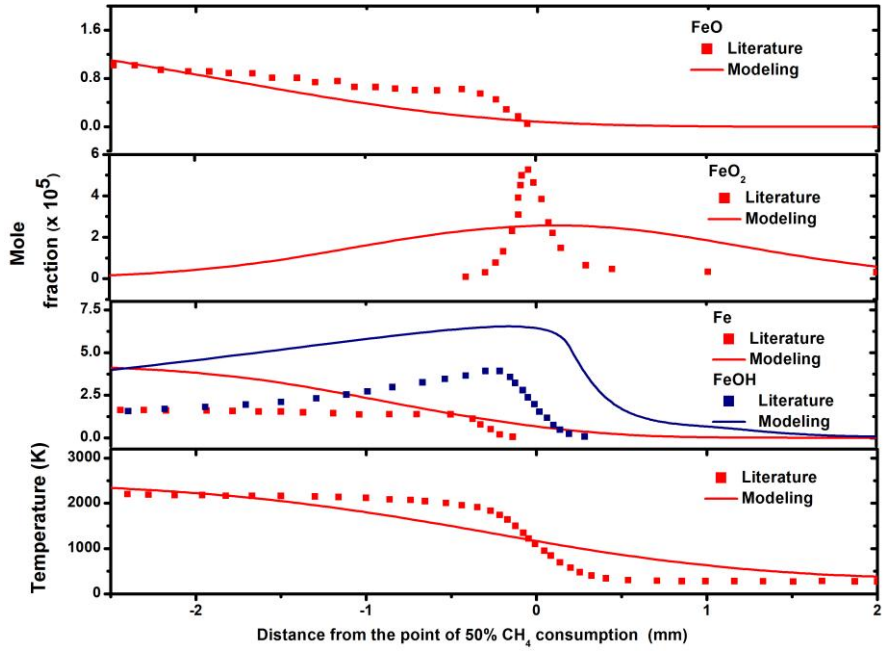

(c)

Figure 4.2: Validation of the (a) temperature; (b) CH_4, O_2 and N_2 species from the developed model with simulation data from literature [146] [148] and; (c) iron oxide and hydroxide species from developed model and simulation data from literature [91]

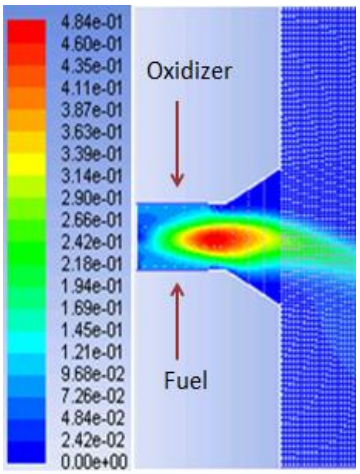

(a) Velocity magnitude-non catalytic

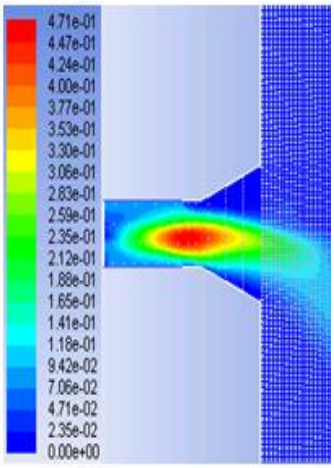

(b) Velocity magnitude-catalytic

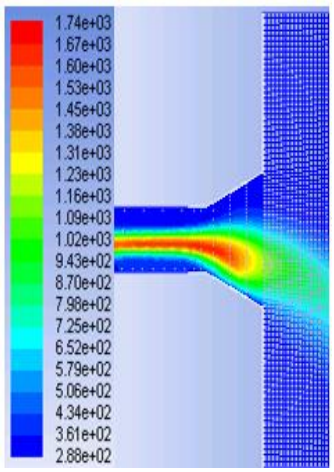

(c) Temperature-non catalytic

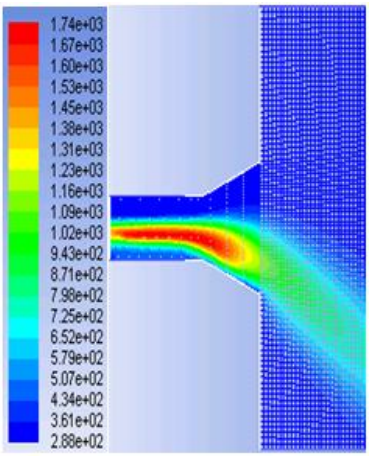

(d) Temperature- catalytic

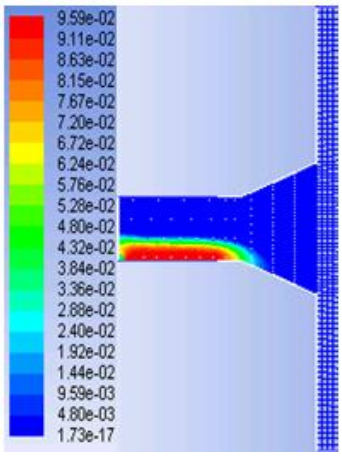

(e) Methane -catalytic

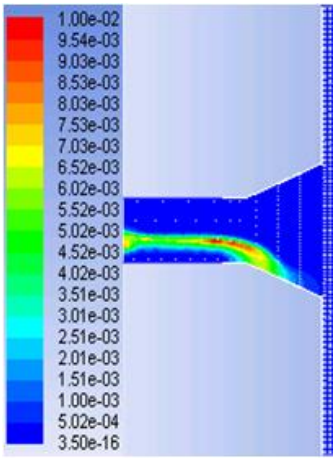

(f) CO-catalytic

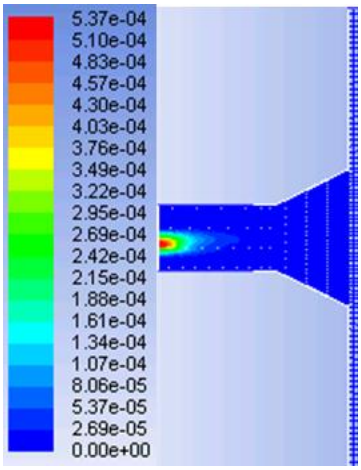

(g) $Fe(OH)_2$

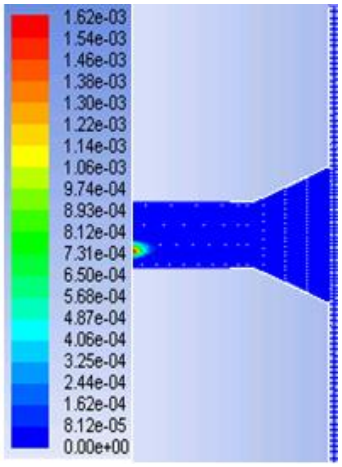

(h) FeO_2

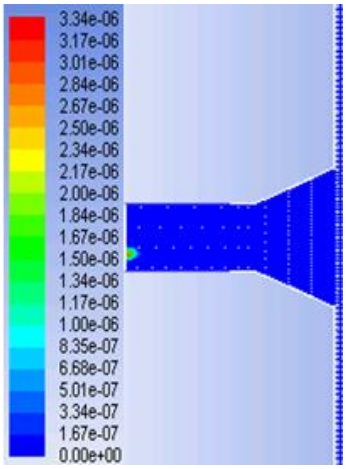

(i) Fe_8 clusters

Figure 4.3: Contours of (a) velocity magnitude vector non-catalytic; (b) velocity magnitude vector catalytic; (c) temperature non-catalytic; (d) temperature catalytic; (e) methane catalytic; (f) CO catalytic; (g) $Fe(OH)_2$; (h) FeO_2 and (i) Fe_8 clusters

4.4.2 Model prediction

Figure 4.3 shows the contours of the temperature and other species as obtained from the simulation. A decrease in the maximum velocity is observed under catalytic conditions, the temperature rise is observed to be more restricted spatially in the case of catalytic combustion. The distribution of the main iron products is also observed close to the centreline of the burner although significant amount of methane can be found at the periphery of the burner. Another important result is the upstream shift of the stagnant plane, towards the fuel port, by a distance of 0.5 mm under catalytic condition as shown in Figure A-3 in Appendix A. This shift hints on the change in the composition of the product species in the combustion reaction under catalytic conditions, which is also verified by the results in Chapter 3 as lesser emission products are detected.

Figure 4.4 sheds light on the model predicted C_2 soot precursor species distribution with reference to the experimental results. The modeling results are found to closely-predict the distribution of C_2H_4 and C_2H_6 under both catalytic and non-catalytic conditions, while under-predicting C_2H_2 under non-catalytic conditions. The effect of precursor addition is visible in terms of the significant decline in the peak values of the species under both modeling and experimental results. Figure 4.5 shows the distributions of CO and NO for the model prediction and the measurement. The modeling results are found to under-predict NO under both the catalytic and non-catalytic conditions as compared to the experimental results; though, qualitatively, they follow the same trend and highlight the effect of emission reduction due to precursor addition. The model prediction for CO under non-catalytic conditions is found to be slightly less than that witnessed experimentally while that predicted under catalytic conditions is found to demonstrate its peak at an upstream location as compared to experimental results. The CO peak under catalytic conditions is larger than that predicted by the non-catalytic model, which is a deviation from the observations in the experimental results which showed a decline in CO on adding $Fe(CO)_5$. This discrepancy

could be attributed to the iron pentacarbonyl decomposition parameters in the reaction mechanism, some of which were estimated in oxygen-free environment.

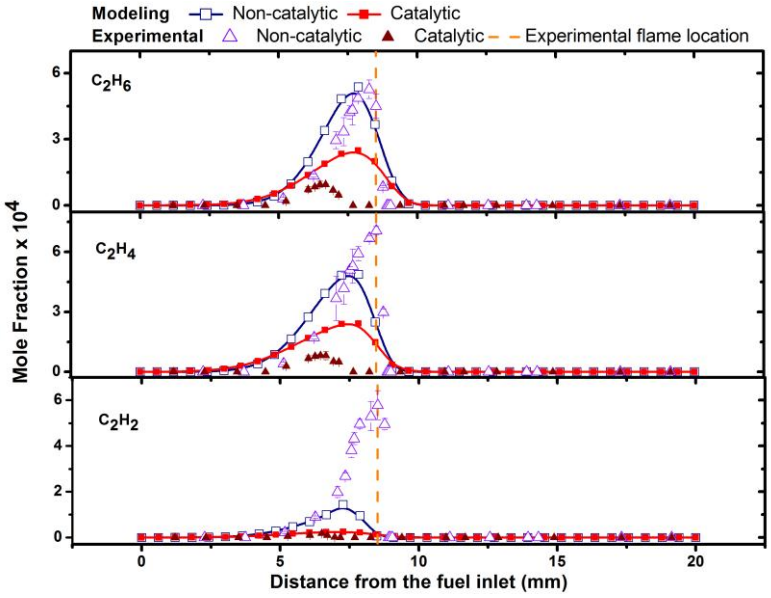

Figure 4.4: Modeling and experimental results of C_2 species distribution under catalytic and non-catalytic conditions

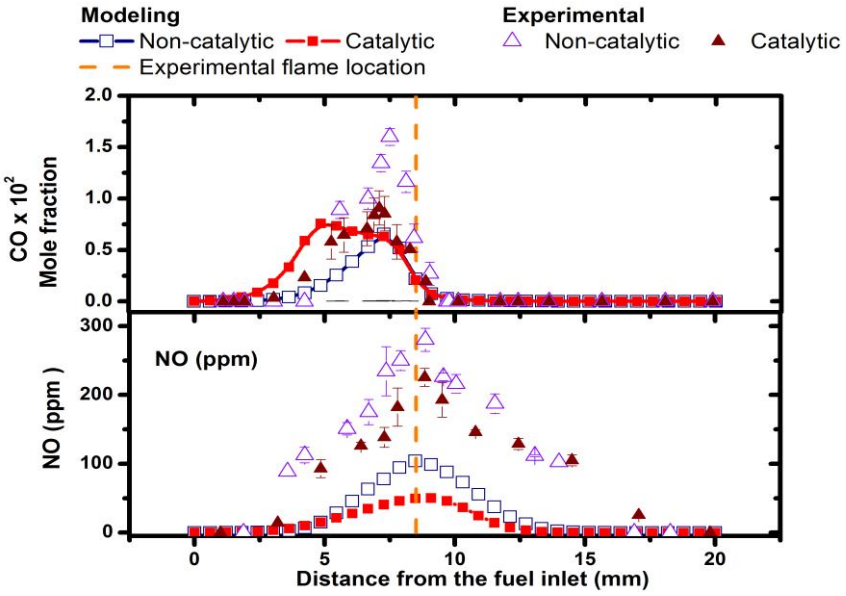

Figure 4.5: Modeling and experimental results of CO and NO distribution under catalytic and non-catalytic conditions

Moreover, a wide range of variation has been reported in the rate constants of some of the association reactions from lower to higher iron carbonyls [149]. The CO profile under catalytic modeling condition resembles a combination of two separate peaks, which is representative of CO evolved from $Fe(CO)_5$ decomposition and CO from partial combustion of fuel.

Figure 4.6 highlights these rates of key constitutive reactions for the prompt NO and thermal NO mechanism under both the catalytic and non-catalytic cases. From the figure, it can be observed that while both thermal and prompt NO reactions are weakened with increasing the precursor concentration; the reactions contributing to the thermal NO are affected more significantly as compared to the reactions impacting the prompt NO.

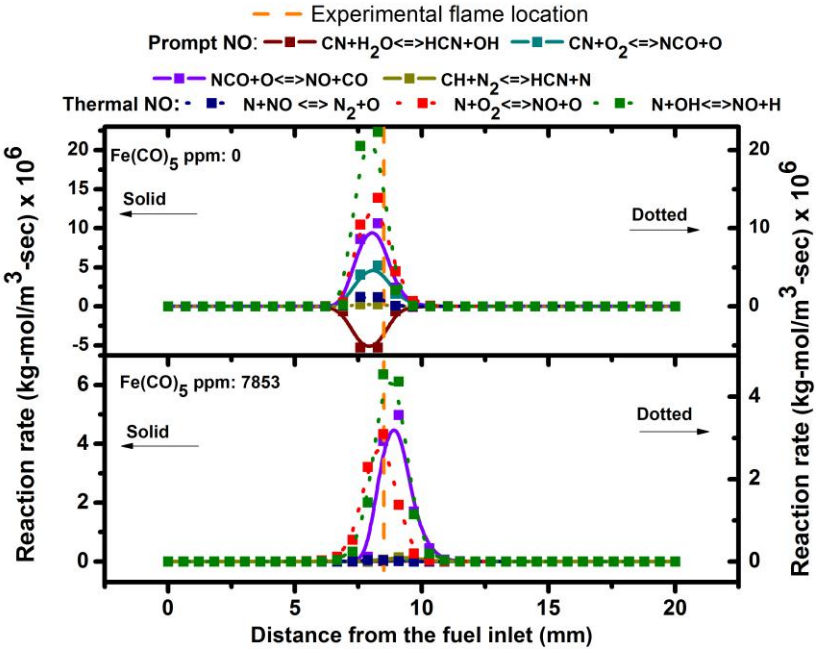

Figure 4.6: Reaction rates for the formation of prompt-NO and thermal-NO as calculated from the developed models

This model is utilized to investigate other aspects of precursor assisted emission reduction which could not be addressed in the experimental investigation. It is important to track the final fate of iron that was hitherto injected in the form of iron precursor so as to understand

its role in the emission reduction mechanism. Figure 4.7 shows the distribution of iron species and clusters along the central axis of the burner under the base catalytic conditions. From Figure 4.7, Fe_8 is observed to be the most dominant while no significant quantities of any other lower order iron cluster (Fe-Fe_7) are observed. Wen *et al.* [102], in their work, have considered higher order clusters (Fe_{16} and beyond) to be representative of incepted iron particles, and thus the present model could be used to provide a fair estimate of particle formation. The presence of various oxides of iron is also witnessed primarily on the fuel side with FeO_2 being the dominant oxide species below the flame while $Fe(OH)_2$ dominates closer to the flame.

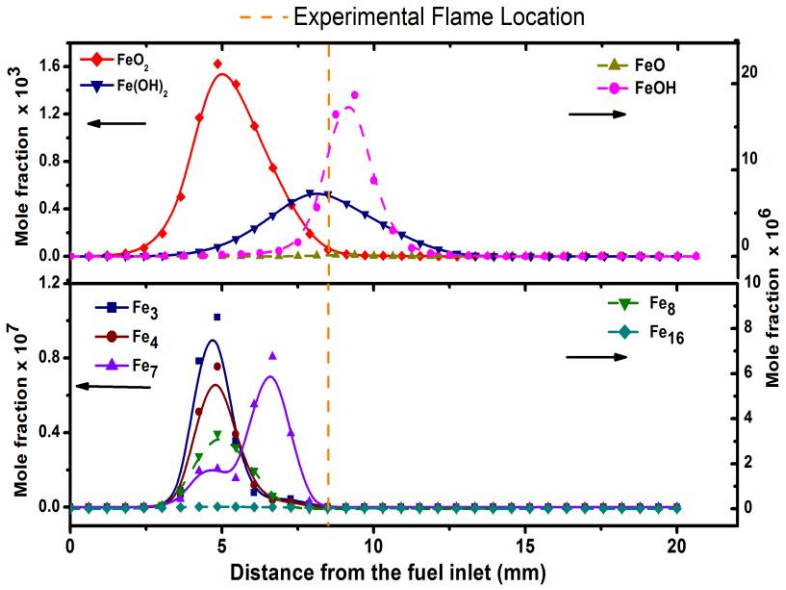

Figure 4.7: Distribution of simulated a) iron oxides, hydroxides and; b) iron cluster along the centreline

4.4.2.1 Effect of precursor concentration

The impact of precursor concentration is also explored on key species in the emissions. Apart from the base catalytic case having precursor concentration of 7853 ppm, lower precursor concentrations of 1500 and 5000 ppm are also explored. Figure 4.8 highlights the relationship between O and OH radicals, NO, C_2H_2, C_2H_4 emissions and the iron precursor concentration. It can be observed that C_2 and NO species along with O and OH radicals

demonstrate a decline in their peak values with increasing the precursor concentration. Also worth noting is the shift of their peak values downstream toward the oxidizer port with increasing the precursor concentration.

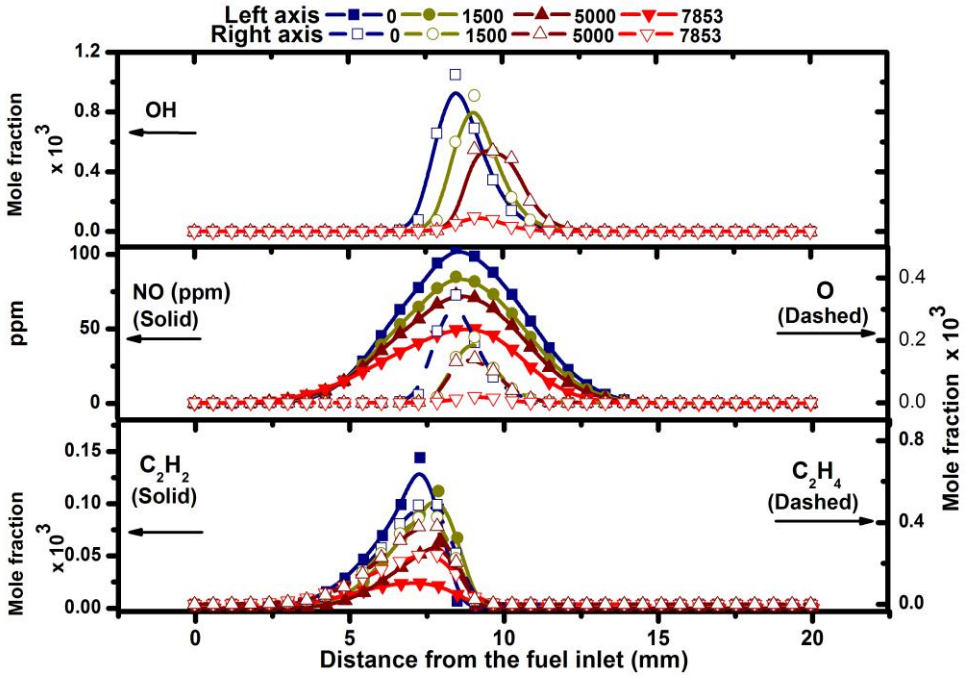

Figure 4.8: Profiles of OH, NO, O and C_2 species under various concentrations of the precursor

4.4.2.2 Effect of methane fraction

In order to ascertain the potency of iron pentacarbonyl at higher temperatures, emission profiles under base catalytic conditions with different methane fractions in the fuel stream were determined, while maintaining the same 7853 ppm of $Fe(CO)_5$. Higher methane fractions of 0.15 and 0.2 are selected for comparison apart from the base case. Figures 4.9 and 4.10 highlight the impact of higher fuel fraction on temperature, CO, NO and C_2 species distribution. Higher temperatures are observed with increasing methane fraction, which demonstrates that the increasing combustion enthalpy due to methane addition plays a more important role in determining the flame temperature. This is also in line with the results of Som *et al.* [150] , in which the impact of higher and lower H_2 fractions in fuel stream on temperature was analyzed.

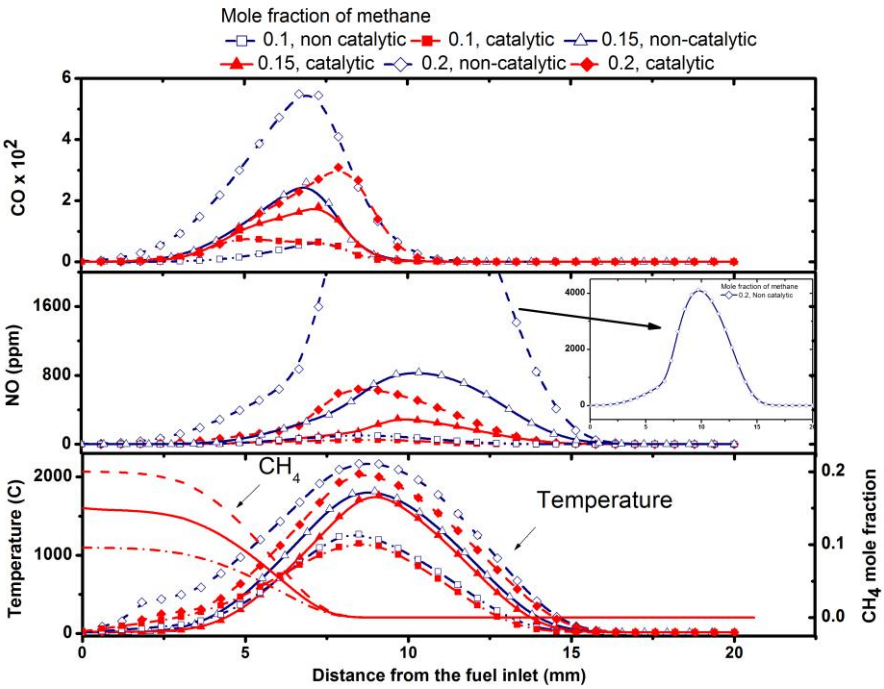

Figure 4.9: Impact of higher CH_4 fraction on temperature, CH_4, CO and NO emissions

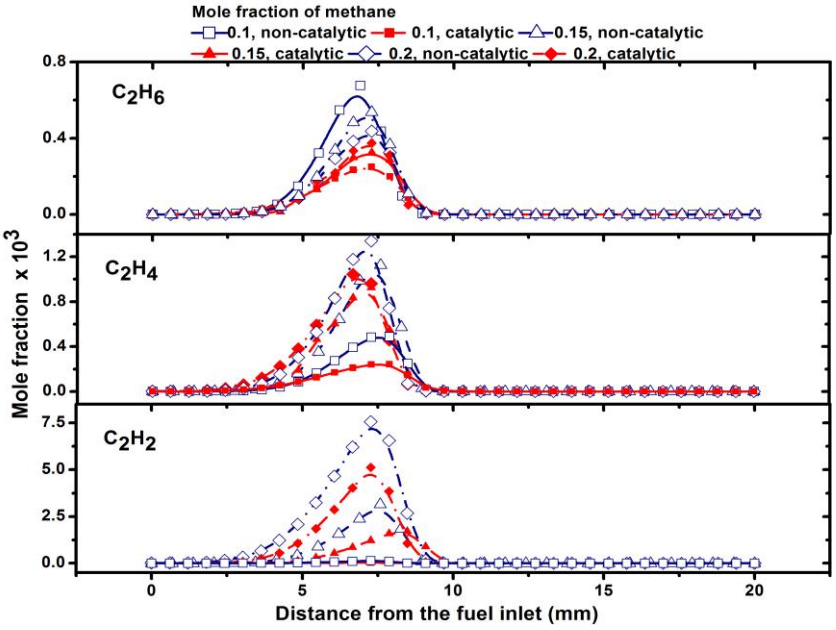

Figure 4.10: Impact of higher CH_4 fraction on C_2 species under catalytic and non-catalytic conditions

With higher temperatures, increased emissions of NO, CO and C_2 species are observed in both the catalytic and non-catalytic cases except in the case of C_2H_6 under non-catalytic conditions in Figure 4.10, which decreases at higher temperatures. The catalytic decline in species is found to be more profound at higher fuel fractions with C_2H_6, NO and CO showing considerably larger decline at higher fuel fractions, while the magnitude of temperature decline due to catalyst addition seems to remain unaffected by increasing fuel fraction. Figure 4.11 shows the distribution of the dominant iron oxide and hydroxide species under different CH_4 fractions. While FeO demonstrates an increase, other species like FeO_2, FeOH and $Fe(OH)_2$ decline with increasing fuel fraction. The FeO_2 peak, which is formed below the flame, is found to move further upstream with increasing fuel fraction. $Fe(OH)_2$, FeO and FeOH peak at a location close to the flame; however, only $Fe(OH)_2$ exhibits similar upstream shift of the peak. Higher temperatures are found to lead to an increased proportion of FeO_2 and FeO in the resultant iron oxides and hydroxide species.

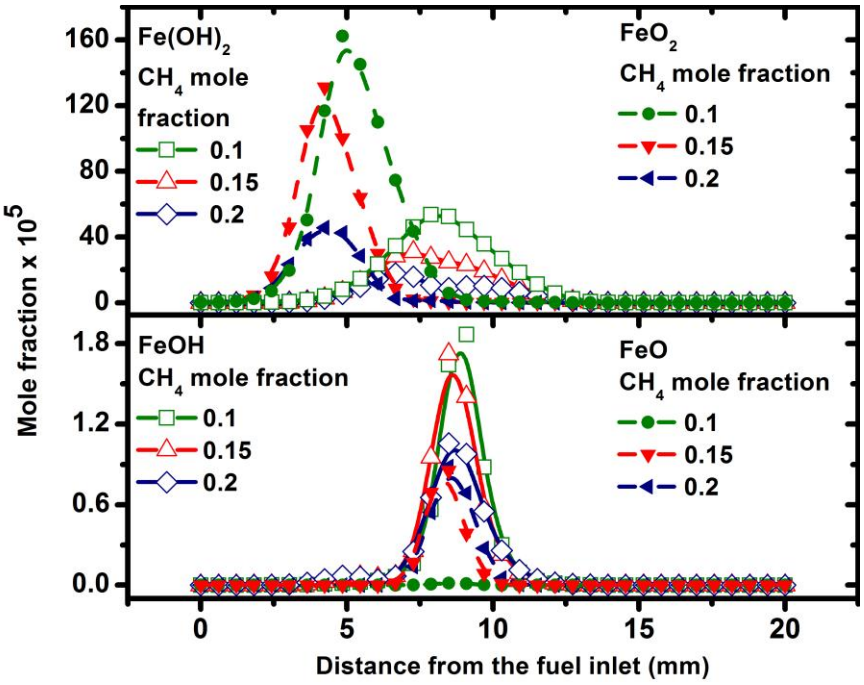

Figure 4.11: Impact of higher CH_4 fraction on iron species

Figure 4.12 highlights the net reaction rates of key iron species with positive and negative rates reflecting formation and consumption of the species, respectively. In the case of FeO_2, the trend demonstrates an initial increase followed by a decline into the negative region, which again returns to the neutral state above the flame. The trend is found to shift downstream initially and the reaction rate is found to decrease with increasing methane fraction on the fuel port side with an almost invariant value being obtained at methane fraction of 0.2. For $Fe(OH)_2$, the net reaction rate trend changes from exhibiting a normal distribution around the flame at the methane fraction of 0.1 to a wave like structure exhibiting an initial rise followed by a fall at higher methane fractions of 0.15 and 0.2 with the reaction rates shifting progressively towards the negative region. In the region just above the flame, the gradient of their net reaction rates under the methane fraction of 0.15 and 0.2 turns positive with the reaction rate returning to a net neutral value.

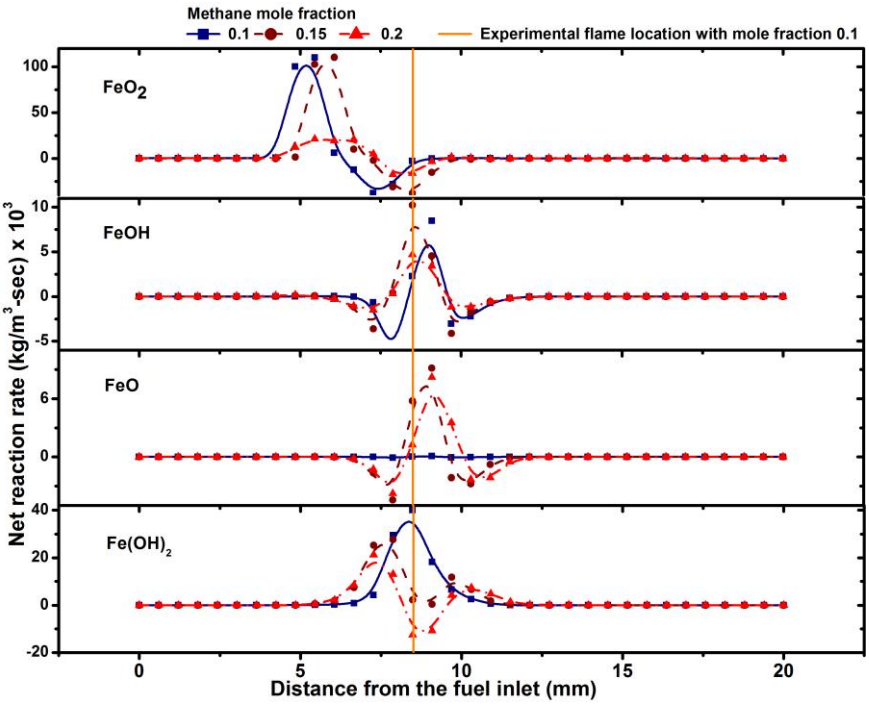

Figure 4.12: Variation of net reaction rate of key iron species with mole fraction of methane

For species FeO and FeOH, their reaction rate is found to be net positive close to the flame location while demonstrating net negative rates in regions distant from the flame and towards

the reactant ports. For FeO, higher methane fractions of 0.15 and 0.2 lead to the highest production rate at the flame and the highest consumption rate in regions further away from the flame, respectively. In the case of FeOH, higher methane fractions induced an initial consumption followed by an increased production of the species that occurs at an upstream location closer to the fuel port. This is followed by a rapid decline occurring above the flame in the oxidizer side. The net reaction rate trend of FeOH witnessed a progressive shift towards positive reaction rates at higher methane fractions.

4.5 Discussion

The developed model, while not accounting for experimental uncertainties such as the flame perturbation effect due to probe sampling and not including iron-oxide clusters in the mechanism due to the absence of their kinetic data, is still found to predict with reasonable accuracy the distribution of temperature and key species; therefore, successfully capturing the impact of $Fe(CO)_5$. The catalytic modeling results for C_2 species, as observed from Figure 4.4, mostly over-predict experimental results, which could be due to the fact the developed model does not account for the heterogeneous surface reactions over the formed iron oxide. As per the findings of Reichert *et al.* [88] and Fennell *et al.* [89], these iron oxide particles act as a source of atomic oxygen, which is transferred to the soot particles through soot-catalyst interface leading to their reduction. Another reason for the emission reduction is the scavenging of reaction propagating radicals like O, H, OH by the major Fe species in gas phase as has been noted in the works of Wlokas *et al*. [105], thus establishing a correlation between the emission reduction and the formation of FeO_2, FeOH and $Fe(OH)_2$. This is illustrated in Figure 4.8, where radicals undergo a decline with increasing the iron pentacarbonyl concentration and a retarding effect is experienced in the combustion process. The formation of C_2H_6, C_2H_4 and ultimately C_2H_2 from methane is a serial reaction process progressing in the same order as described by Turns [18], aided by the reaction propagating radicals O, H and OH. The abstraction of these radicals by iron species is thus found to hamper the formation of these C_2 radicals, thereby curtailing their emissions. An upstream

shift of the stagnation plane, as seen from Figure A-2 in Appendix A, also indicates momentum loss on the fuel side possibly due to faster decomposition of methane into other products and also results in an enhanced penetration of oxygen from the oxidizer port towards the fuel port.

It is observed from the combined mechanism that as $Fe(CO)_5$ breaks down, two competing mechanisms struggle for the gas phase iron atoms: one leading to their formation of clusters; while the other involves their reaction with the reaction propagating radicals. The concentration of the larger iron clusters remains insignificant close to the fuel port and show further decline on the oxidizer side due to the presence of an oxygen lean environment. From Figures 4.11-4.12, it can be determined that while FeO_2 and $Fe(OH)_2$ are the key final products; higher temperatures closer to flame activate pathways leading to the formation of FeO at the cost of FeO_2 , FeOH and $Fe(OH)_2$ while the production of these other species is shifted upstream closer to the fuel port. In order to further validate this, the contribution of individual reactions from the overall mechanism towards the production and consumption of key iron species specified in literature [105] , is analyzed with respect to methane fraction.

The key reactions from the mechanism, found to have the greatest contribution towards major iron species from the modeling results, are depicted in Table 4.2 along with their reaction parameters. These reactions are found to be similar to those mentioned in the works of Gerasimov *et al.* [151] and Wlokas *et al.* [105] . Figure 4.13 illustrates the reaction rates of key iron species reactions from Table 4.2 at different methane mole fractions. Reactions 1, 2, 4, 7, 8 and 9 from Table 4.2 demonstrate their enhanced reaction rates with increasing the methane fraction, although reactions 4 and 9 do exhibit a degree of saturation in their reaction rates beyond the the mole fraction of 0.15. Reactions 3, 5 and 6 show an initial increase followed by a rapid decline. This decline in the reaction rate of these specific reactions can be attributed to other reactions, involving the consumption of reactant species FeO_2 and FeOH, becoming thermally activated at elevated temperatures. This can be seen from the trend of R7 in Figure 4.13 between axial distance of 6 to 8 mm, where there is no significant increase even at methane mole fraction of 0.2, as well as from Figure 4.12, where

there is a decline in the net reaction rate of FeO_2 and FeOH with increasing the methane fraction from 0.15 to 0.2 within the same axial range. From Figure 4.13 it is observed that the conversion of FeOH to $Fe(OH)_2$ is not direct but happens through the formation of intermediate FeO as the reaction rates of R4 and R5 convert FeOH to FeO remains an order higher than that of R6 converting FeOH to $Fe(OH)_2$ even at the high methane mole fraction of 0.2. This is also reflected in an increase in the net formation rate of FeO at the flame, which coincides with the decline in $Fe(OH)_2$ as shown in Figure 4.12.

Table 4.2: Major reactions contributing to the formation and consumption of key iron species as seen from simulation results

Reaction No.	**Reactions**	**$K= AT^B exp(-E_A/RT)$**			
		A (mol.cm.sec.K)	**B**	**E_A (cal/mol)**	**Reference**
1	$Fe+O_2(+M) \Leftrightarrow FeO_2(+M)$	2.00E+13	0	0	Rumminger et al. [91]
2	$FeO_2+OH \Leftrightarrow FeOH+O_2$	1.00E+13	0	11992.7	Wlokas et al. [105]
3	$FeO_2+O \Leftrightarrow FeO+O_2$	1.50E+14	0	1499.3	Wlokas et al. [105]
4	$FeOH+O \Leftrightarrow FeO+OH$	5.00E+13	0	1499.3	Wlokas et al. [105]
5	$FeOH+H \Leftrightarrow FeO+H_2$	1.50E+14	0	1598.6	Wlokas et al. [105]
6	$FeOH+OH \Leftrightarrow Fe(OH)_2$	6.00E+11	0	0	Rumminger et al. [91]
7	$Fe(OH)_2+H \Leftrightarrow FeOH+H_2O$	1.98E+14	0	599.7	Rumminger et al. [91]
8	$Fe(OH)_2+OH \Leftrightarrow FeOOH+H_2O$	1.00E+13	0	17990.1	Rumminger et al. [91]
9	$FeO+H_2O \Leftrightarrow Fe(OH)_2$	1.62E+13	0	0	Wlokas et al. [105]

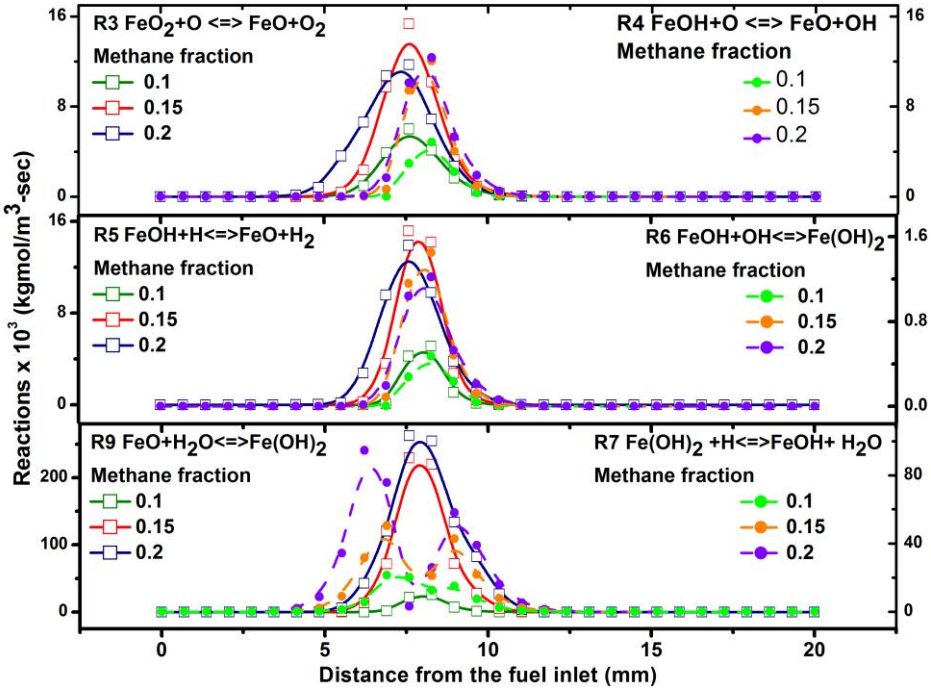

Figure 4.13: Rates of some of the iron reactions specified in Table 4.2 with different methane fractions

The key impact of increased temperature as a result of higher methane fraction is a significant enhancement of the reaction kinetics of methane combustion and iron oxide and hydroxide formation. While the lower temperature contributes to lesser thermal NO_x, the emission reduction in the case of C_2H_4 and C_2H_6 species is found to be the highest in the case of fuel fraction of 0.1, while the emission reduction in the case of C_2H_2 species is highest at the fuel fraction of 0.2. This is due to the fact that although there is an increase in the radical pool at higher fuel fraction contributing to enhanced formation of C_2 species as shown in Figures 4.8 and 4.9, the iron oxide species formation is greatly enhanced as well, thereby, increasing the scavenging of the radicals as shown in Figures 4.11 and 4.12. Since C_2H_2 is the final product in a linear serial mechanism derived from C_2H_4 and C_2H_6, as highlighted in the methane combustion mechanism in Figure 2.1, the impact of enhanced scavenging by

iron species results in a greater reduction of C_2H_2 as compared to C_2H_4 and C_2H_6 at higher fuel fractions.

4.6 Summary

The present work numerically analyzes the iron precursor assisted emission reduction process in a counterflow methane diffusion flame in order to better understand the underlying catalytic process and factors that influence it. The developed model was validated against numerical and experimental data from the literature. The emission reduction process was attributed to the scavenging of the reaction propagating radicals by the iron species formed in flame. Most of the emissions were found to decrease with increasing precursor concentration with the gradient declining at higher precursor concentrations. The enhanced fuel fraction increases the availability of fuel resulting in higher temperatures, which, upon addition of iron precursor, activates certain temperature dependent iron reaction pathways, which, in turn, enhances the radical scavenging process. However, beyond a certain threshold the enhanced fuel fraction enlarges the radical pool sufficiently enough to overwhelm the additional iron reaction pathways responsible for radical scavenging and consequently the emission reduction declines. It highlights the reduced potency of precursor in reducing emissions at higher temperatures and oxidizer rich environment and therefore the precursor injection should primarily be restricted in the fuel rich region.

Chapter 5

Particle sampling and growth analysis in a counterflow methane flame using Scanning Mobility Particle Scanner (SMPS)

5.1 Overview

The addition of metal additives to fuel is being explored as a possible method for emission control due to in-flame synthesis of iron oxides, which acts as a catalyst for achieving cleaner combustion. The particle evolution process governs the particle size that determines the available specific surface area for catalysis. Using a counterflow burner configuration enables better visualization of the particle evolution process due to the formation of distinct fuel rich and fuel lean regions and also provides ease of sampling. This chapter focuses on analyzing the impact of iron pentacarbonyl on the particle evolution process in a counterflow methane diffusion flame through mapping of particle parameters from various axial and radial locations near the flame by means of an orifice. This is followed by the analysis of geometric mean particle diameter, mean particle concentration and particle size distribution using a Scanning Mobility Particle Sizer (SMPS) and the analysis of particles' morphology using Scanning Electron Microscope (SEM), under both non-catalytic and catalytic conditions. The results highlight enhanced particle inception at lower temperatures with reduced mean particle size under catalytic conditions, indicating enhanced presence of smaller sized particles. The result also hints at the possible encapsulation of smaller iron oxide particles within larger soot particles.

5.2 Introduction

The use of transition metal additives in reducing emissions during fuel combustion results in the aerosol flame synthesis of metal oxide catalyst particles in the flame under an oxygen lean environment [152]. As specific metal oxides have demonstrated strong catalytic potential for oxidation of soot on account of their enhanced oxygen mobility within the crystal lattice [70] [71], it is vital to explore physical parameters associated with the particle evolution process. As the catalysis process is governed by the available specific surface area [153] [154], it becomes imperative to monitor parameters like size, concentration and size distribution at various stages of the combustion process in order to develop a fundamental understanding of the particle evolution process, which could later be used for optimizing the operating conditions for best results. As there are multiple factors influencing the particle evolution process, there is a need to simplify the process so as to isolate the factors influencing the process and study their respective influence. The counterflow flame is, therefore, quite suited for this application as it can be considered as an approximation of laminar flamelets, which constitute a turbulent diffusion flame [107], thus being more representative of actual combustors like furnaces, gas turbines and diesel engines. It assists in simplifying the analysis since under counterflow conditions, the time scale of the chemical reactions is much smaller compared to the diffusion and convective time scales [106]. The objective of this study is to develop a methodology for particle sampling over a counterflow diffusion methane flame and carry out the sampling to shed light on the underlying evolution process.

5.3 Experimental setup and methodology

In the present work, the mean particle size, number concentration and size distribution are measured from various locations of a counterflow, laminar methane flame bearing iron precursor by means of a GRIMM Aerosol Scanning Mobility Particle Sizer. Scanning mobility particle sizer (SMPS) is capable of determining particle size distribution and total particle concentration in almost real-time. The SMPS system comprises of i) Medium-

Differential Mobility Analyzer (DMA) (GRIMM Model 5.706) for segregating the polydispersed particles into mono-dispersed bins on account of their varying electrical mobility and; ii) Faraday Cup Electrometer (FCE) (GRIMM Model 5.706)) for measuring the concentration of the segregated charged particles. While the FCE is capable of high resolution and therefore exhibits good accuracy in detecting particles from 0.8 nm to 1100 nm [155], the medium sized DMA restricts the detection limit from 8 to 500 nm. The sample flow, sheath flow, channel width etc. are controlled by means of an external console. The particles are initially charged and then classified by varying the applied voltage in a stepwise manner, causing smaller diameter particles to deviate first towards the detector, followed by larger particles. The sample flow determines the sample size flowing into the device by means of a built-in pump in the device while the sheath flow assists in reducing particle loss and enhancing the resolution [155]. The device uses a filter to accumulate the charge on the nanoparticles and an amplifier to convert the electrical charges on the nanoparticles to voltages by using a resistor of 2.5 TΩ.

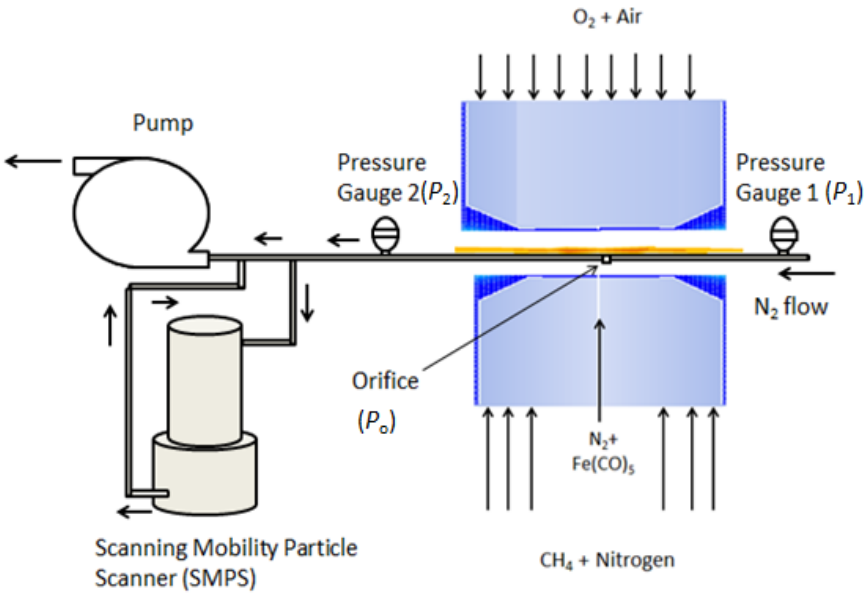

Figure 5.1: Schematic of the counter-flow burner and SMPS arrangement

The details of the counterflow burner apparatus and the methane flame parameters are specified in Section 3.3 in Chapter 3. The sampling technique, developed by Zhao et al. [125], involving the use of an orifice bearing tube is modified in the present study to achieve sampling under a counterflow flame. Figure 5.1 shows the schematic of the setup. A steel tube, of specified length (see Table 5.1) and ¼" O.D, is connected to a mass flow controller and is placed on a movable platform which provides axial and radial movement. An orifice of fixed diameter is made on the tubing for the purpose of sampling. A high flow rate of nitrogen is passed through the steel tubing to minimize particle agglomeration in the incoming sample line as well as to entrain the particles in the flow and direct them to the SMPS. Different orifice diameters are chosen to vary the dilution ratios. This orifice is placed at different locations between the two burners using the movable platform and is used to draw samples from the flame by means of a pump. The vacuum pressure is estimated by means of two digital pressure gauges placed upstream and downstream of the orifice. A secondary tube, placed next to the downstream pressure gauge, diverts some amount of sample into the SMPS system. 100% isokinetic sampling is assumed in the study while the amount of sample drawn is controlled by the SMPS console.

Other studies employing ethylene, a known soot precursor, as the fuel have utilized a high diluent flow rate of 29.5 slm [125] [156]. The present experimental setup utilizes methane fuel, which has lesser propensity to produce soot and would therefore not require such high diluent flow rate [135]. In order to determine the diluent nitrogen flow rate, it is important to consider additional constraints that accompany the use of a counterflow burner. While an increased nitrogen flow would ensure high dilution rates, it is equally important to ensure that: i) the flat laminar flame remains undisturbed; ii) a suction pressure is maintained at the orifice and; iii) a steady flow from the sample line is maintained towards the SMPS. Addressing all these criteria, it was determined that a diluent N_2 flow rate of 10.5 slm was adequate. Equations (5.1)-(5.4) are used to determine the dilution ratio [125] .

$$\Delta P = P_1 - P_2 \qquad (5.1)$$

$$P_o = P_1 - \frac{a}{L}\Delta P \quad (5.2)$$

$$V_o = \frac{\pi {d_o}^4}{128\mu t}(P_{atm} - P_o) \quad (5.3)$$

$$f_D = k\frac{V_s}{V_o} \quad (5.4)$$

In these equations, P_1 and P_2 are the respective pressures upstream and downstream of the orifice, respectively. P_o, V_o and d_o represent the pressure at the orifice, sample flow through the orifice and diameter of the orifice, respectively. f_D represents the dilution ratio while V_s represents the Nitrogen flow rate. L and a represent the distance between both the pressure gauges and the distance from the upstream pressure gauge to the orifice, respectively, μ represents the dynamic viscosity as calculated through numerical modeling, c represents the coefficient based on experimentation, t represents the pipe thickness and k represents the ratio of temperature at the orifice to that of the ambient. Table 5.1 below highlights the key parameters for sampling process used in the present work.

Table 5.1: Key parameters and their values used in the present study

Parameters	**Values**
Distance between the pressure gauges L	19 cm
Distance between upstream pressure gauge and orifice a	11.5 cm
Sheath air flow rate	5 litres/min
Sample flow rate	1 litre/min
Nitrogen flow rate (V_s)	10.5 litres/min
Number of mono-dispersed channels	24
Thickness of steel tube (t)	1.05 mm

The total particle concentration (N) which represents the total number of particles in 1 cm^3 and the gradient of particle concentration with respect to the log of its diameter

(dN/d(log D_p)) for each bin, respectively, are derived from the SMPS after subtracting the background, which is obtained under the diluent nitrogen flow. The upper limit of the bin 'i' is $D_{p,u}$ while lower limit is specified by $D_{p,l}$. The channel size ($D_{p,u} - D_{p.l}$) and the average bin diameter are determined through the number of channels being used for the analysis. Equation (5.5) is utilized to determine the particle concentration in each channel [157]. D_p is assumed to be approximately the midpoint of the ith channel.

$$n_i \approx \frac{dN}{d(\log D_p)} . (\log D_{p,u} - \log D_{p.l}) \qquad (5.5)$$

From the particle concentration in the individual channels, the geometric mean diameter of the sample, across all the channels, is derived using equation (5.6)-(5.7) [157].

$$D_g = (\prod D_i^{n_i})^{1/N} \qquad (5.6)$$

$$N = \sum n_i \qquad (5.7)$$

Here n_i and D_i represents the particle concentration and the midpoint particle diameter at the ith channel, respectively. It is important to estimate the degree of coagulation happening in the sampling line from the probe location to the SMPS in order to develop a comprehensive understanding of the particle evolution process and highlight any possible limitations of the present method. The average coagulation coefficient for a polydispersed aerosol was estimated from Table 12.4 from the work of Hinds [158]. The residence time of the sample, from the probe to SMPS, in the sampling line is calculated to be around 54 miliseconds. Using the most polydispersed geometric standard deviation of 2.5, the average coagulation coefficient is found to range between 50.9 X 10^{-10} to 10.1 X 10^{-10} cm^3/s for median diameter size ranging from 10 nm to 500 nm, respectively. The degree of coagulation is estimated from equation (5.8).

$$\frac{N_{coagulated}(t)}{N_{total}} = \frac{N_{total}\,\bar{K}\tau}{1+N_{total}\,\bar{K}\tau} \qquad (5.8)$$

Here $N_{coagulated}/N_{total}$ represents the fraction of particles that has undergone coagulation, while N_{total} represent the total number of particles. The residence time is represented by τ while $\bar{K}$ represents the average coagulation coefficient.

5.4 Results

The vacuum generated by means of the pump is carefully balanced against the diluent nitrogen stream to achieve the required level of suction without influencing the flame. Under conditions of valve being 100% open, Figure 5.2 shows that the dilution ratios decrease with increasing the orifice diameter as more sample is drawn in with a higher orifice diameter. The dilution ratios at various radial locations do not vary from that detected at the central axis (r=0 mm). An increase in the dilution ratio is found to occur with increasing the axial direction from the fuel port with its peak being achieved close to the flame location, beyond which a decline is witnessed in the trend. This increase is largely due to a combination of increasing temperatures, viscosity as well decreasing orifice pressure at locations closer to the flame. The lowest dilution ratio under the orifice diameters of 0.5 mm, 0.75 mm and 1 mm are roughly 1050, 480 and 150, respectively. The dilution ratio is utilized to estimate the actual particle concentration at different locations from the detected particle density.

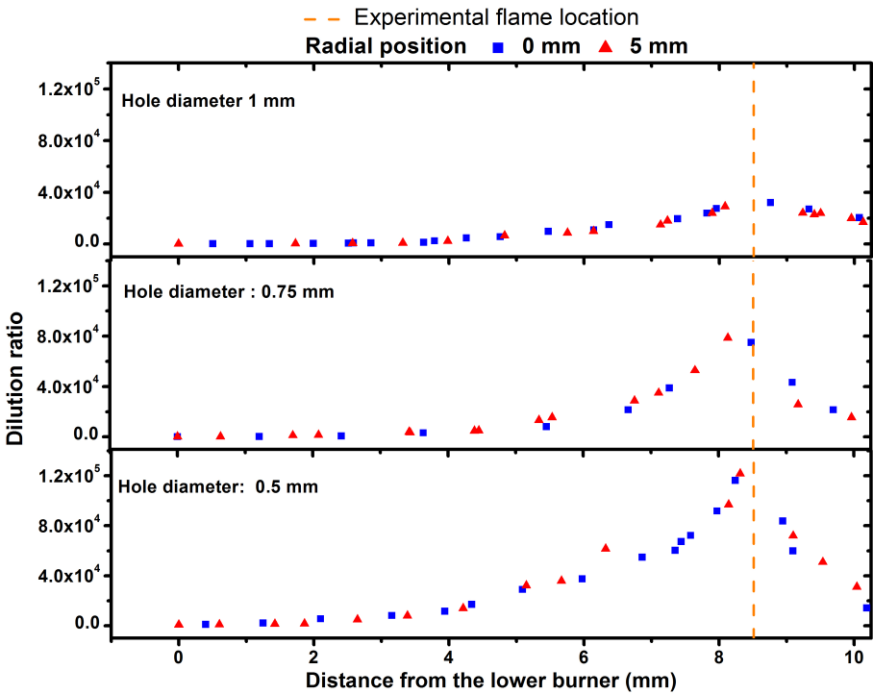

Figure 5.2: Dilution rates at different locations for various orifice diameters

5.4.1 Particle concentration and geometric mean particle size measurements

Figure 5.3 and Figure 5.4 highlight the spatial distribution of the geometric mean particle size and particle concentration under both non-catalytic and catalytic conditions using orifice sizes of 0.5 mm and 1 mm, respectively.

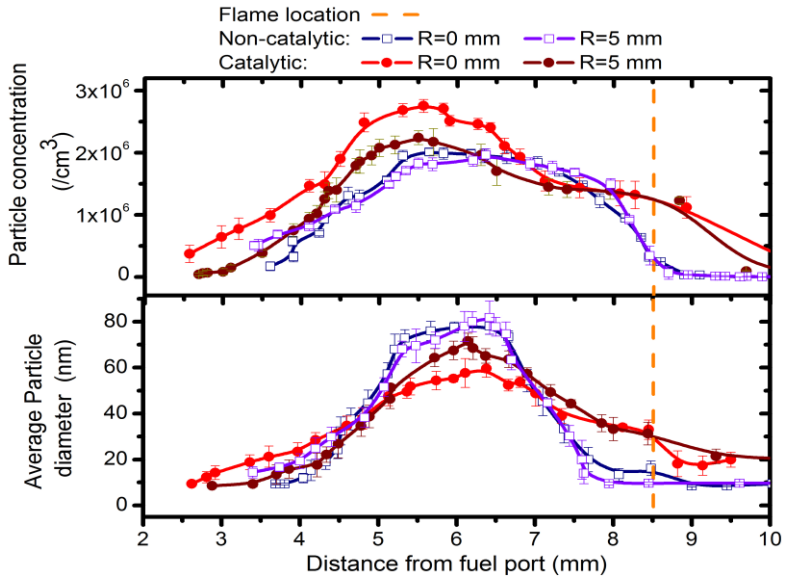

Figure 5.3: Total particle concentration and geometric mean particle size under non-catalytic and catalytic conditions sampled with an orifice size of 0.5 mm

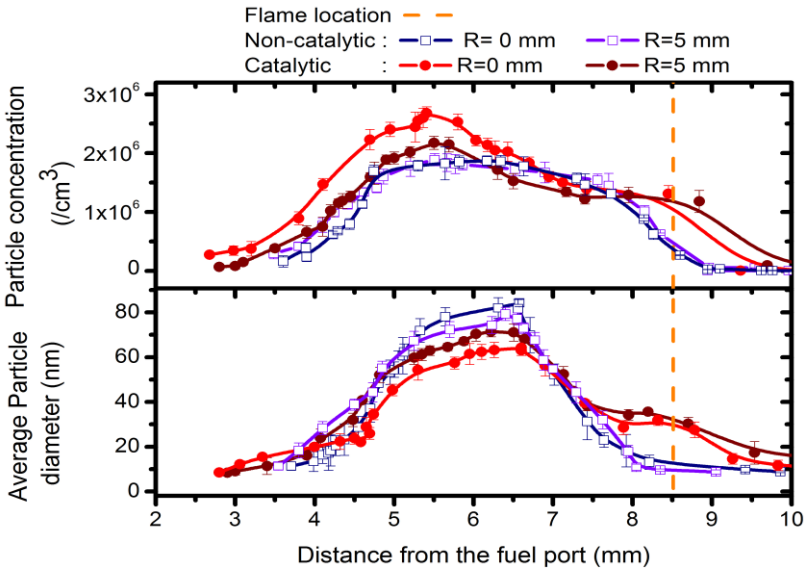

Figure 5.4: Total particle concentration and geometric mean particle size under non-catalytic and catalytic conditions with an orifice size of 1 mm

Under non-catalytic conditions, the measurements are carried out at the radial distances of 0 and 5 mm, respectively, from the burner axis in order to account for presence of concentric tube at the fuel port for precursor injection. Under both orifice sizes, the particle concentration and mean size are marginally higher at the radial distance of 5 mm, than that seen at the radial distance of 0 mm between axial distances of 3-5 mm from fuel port, as seen from Figures 5.3 and 5.4. No significant difference in the particle concentration and mean particle size values is detected at other downstream locations on account of their radial location. This is due to the fact that the concentric tube, used solely for precursor injection, lies at the centre (radial distance 0 mm) of the fuel port and no methane is injected through that tube leading to reduced soot formation. At locations further downstream at r = 0 mm, the diffusion of methane from radial direction brings the methane concentration as well as particle formation to same levels as that at the radial locations. Under non-catalytic conditions, the maximum average particle size is found to be around 82 nm and the maximum particle concentration is around 2.01×10^6 per cm^3 at the axial distance of approximately 6.5 mm and 5.5 mm, respectively, from the fuel port as measured under both orifice sizes. On comparing the results between the two orifice sizes of 0.5 mm and 1 mm, higher values of mean particle size along with lower particle concentration are observed using the orifice diameter of 1 mm as seen from Figures 5.3 and 5.4. For better visualization, these results are presented separately in Figures B-1 and B-2 in the Appendix B.

The initial soot particles, under non-catalytic conditions, are detected at an axial distance of around 3.5 mm. Moving downstream towards the flame, an initial increase in particle size and concentration is observed, as seen in Figure 5.3 and Figure 5.4. A two-phased increase in particle size is observed up to an axial distance of 6.5 mm with the shorter succeeding phase, observed from 5 mm to 6.5 mm, having a much smaller gradient as compared to the longer preceding phase. Beyond 5 mm, the particle size continues to demonstrate a much slower growth up to an axial distance of 6.5 mm, thereafter, a rapid decline is witnessed leading to almost complete combustion of particles under both orifice diameters. The increase in particle concentration is found to be linear up to an axial distance of 5.5 mm. After this, this

rapid initial rise is found to slow down and ultimately be reversed into a gradual decline, which becomes more profound after 7.5 mm.

Under catalytic conditions, particles are detected at an upstream location as compared to that under non-catalytic conditions. An increase in the particle concentration and mean particle size is observed in the direction of the flame. The particle concentration at radial location of 0 mm under catalytic conditions exceeds that under non-catalytic conditions and reaches a maximum of 2.72 x 10^6 /cm^3 at a much upstream location of 5.3 mm. However, at locations closer to the flame between 6-7 mm, particle densities exhibit steeper decline and are lesser as compared to those under non-catalytic conditions. The impact of reduced particle concentration is also exhibited on the mean particle size whose peak value is significantly reduced under catalytic conditions to around 70 and 64 nm, respectively, at radial distance of 5 mm and 0 mm from the burner axis. The central tube injection of precursor restricts its spread radially especially at lower axial distances causing the catalytic particle concentration trend at radial distance of 5 mm to closely resemble that of non-catalytic conditions from fuel port till axial location of 5 mm. Thereafter, the trend diverges and follows qualitatively the trend exhibited under catalytic conditions at radial distance of 0 mm, although the reduction in the particle size is not as significant as that at radial distance of 0 mm. This reduced catalytic effect, at radial distance of 5 mm, is also manifested in the form of lower maximum particle concentration as well as reduced intensity for initial increase and later decline in the particle concentration, as compared to catalytic conditions.

5.4.2 Particle size distribution

5.4.2.1 Non-catalytic conditions

Figure 5.5 highlights the particle size distribution in the collected sample over mono-dispersed channels of specific diameters under non-catalytic conditions using the orifice diameter of 0.5 mm. The insets within Figure 5.5 magnify the concentrations of sub-100 nm particles, present in the sample. Under both radial locations, most of the particles are found to be of sub-150 nm size. A high concentration of particles (<10 nm) is observed at an axial

location of around 3.5-4 mm indicating the initiation of the soot inception process. At axial distances below 5 mm and between 7 mm and the flame location, the samples are found to be mainly dominated by sub-50 nm particles with only a smaller number of particles of larger diameters being present. With increasing axial distances towards the flame, a gradual shift of the particle size distribution towards large particle size (>200 nm) is observed along with an increasing prominence of the bimodal nature. The concentration of particles greater than 200 nm is found to be less at the radial distance of 5 mm as compared to that at radial distance of 0 mm, possibly due to stronger radial velocities moving heavier particles in the sample away from the probe. However, beyond an axial distance of 7 mm, there is a reverse shift towards lower particle size along with a decrease in the absolute particle concentration at each mono-disperse channel and decline in bimodal nature.

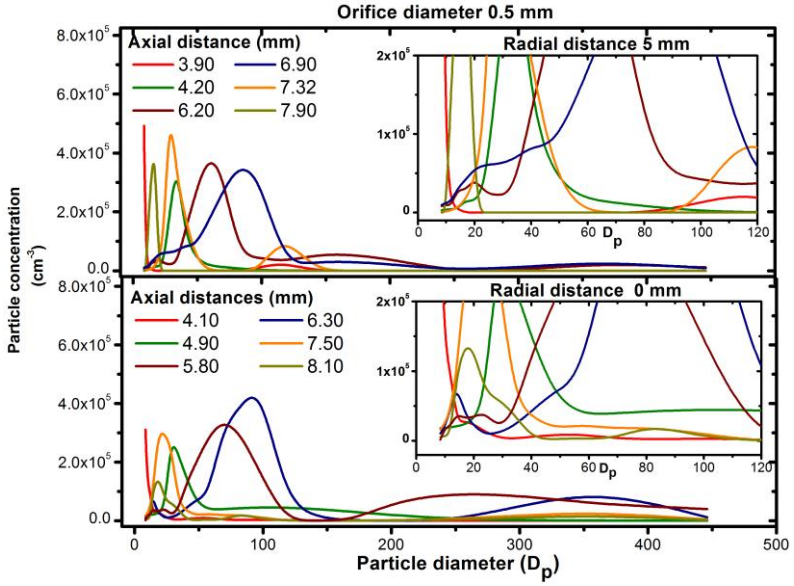

Figure 5.5: Particle concentration distribution with respect to particle diameter at various axial positions under orifice diameter 0.5 mm under non-catalytic conditions

Figure 5.6 highlights the particle size distribution among various mono-dispersed channels under non-catalytic conditions using the orifice diameter of 1 mm. The trend is similar to that observed using an orifice diameter of 0.5 mm in Figure 5.5. Up to an axial distance of around 5 mm, the size distribution is primarily unimodal with the peak shifting towards higher particle size with increasing axial distance. Beyond this axial distance, there is a larger

variation in the particle sizes in the sample and the distribution turns bimodal with large particles of around 200-300 nm also being detected. The bimodal distribution of particles between axial distances of 5 and 7 mm is centered at 80 nm and 250-300 nm, respectively as seen in Figures 5.5 and 5.6. Further closer to the flame, the particle concentration across all particle sizes is greatly reduced and a unimodal distribution around 15-20 nm is observed.

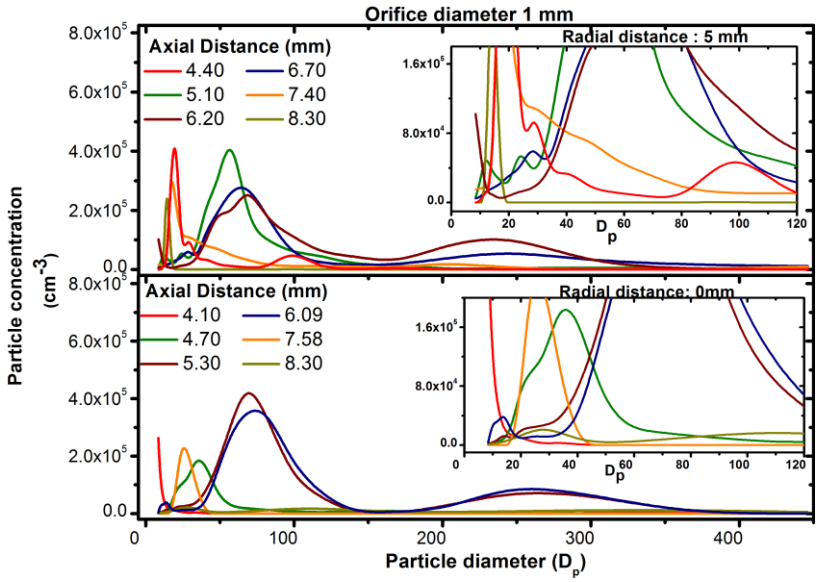

Figure 5.6: Particle concentration distribution with respect to particle diameter at various axial positions under orifice diameter 1 mm under non-catalytic conditions

5.4.2.2 Catalytic conditions

Figure 5.7 and Figure 5.8 show the distribution of particle size among various mono-dispersed channels in a precursor-laden flame as sampled using an orifice of 0.5 mm and 1 mm, respectively. Particle inception is found to initiate at an upstream axial location of 2.5-3 mm, as compared to non-catalytic conditions. Particles with diameter (<50 nm) are found to predominate in the sample up to an axial distance of 5 mm. An increase in particle concentrations, as well as a shift in the peaks towards larger diameters, is observed on moving away further downstream from the fuel burner to an axial distance of 7 mm. At regions between the axial distances of 5 to 7 mm, the bimodal distribution of particles is exhibited, which is centered around 50 nm and 300-350 nm, respectively. While the second

mode for the particle distribution is found to shift towards larger particle diameters, the particle concentration at those diameters remains considerably low. For both orifice diameters, there is a reverse shift of the peak towards smaller sized particles at locations very close to the flame, possibly due to disintegration of the large agglomerates.

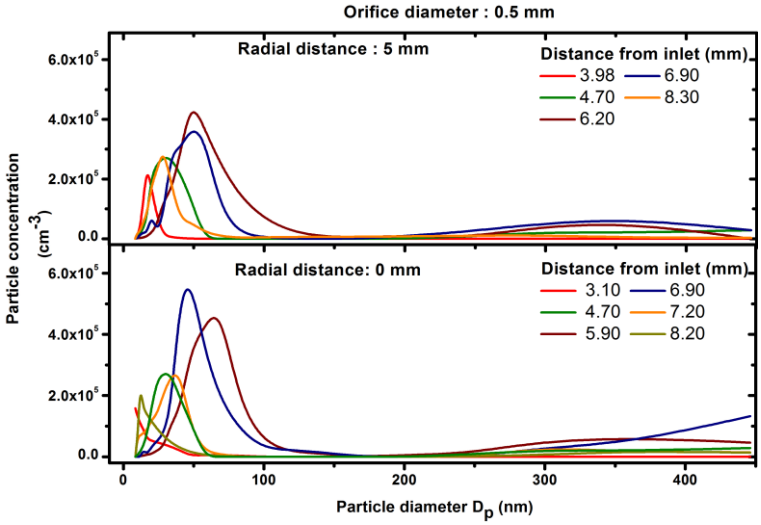

Figure 5.7: Particle concentration distribution with respect to particle diameter at axial locations under orifice diameter 0.5 mm under catalytic conditions

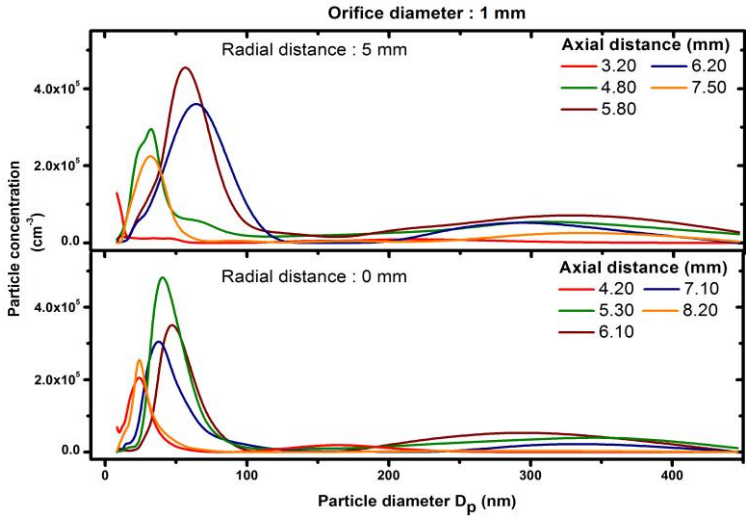

Figure 5.8: Particle concentration distribution with respect to particle diameter at axial locations under orifice diameter 1 mm under catalytic conditions

Overall, higher particle concentration is seen at the radial location of 0 mm than that at 5 mm due to precursor injection at radial location of 0 mm. An increased particle concentration of larger sized particles (>200 nm) is observed in samples obtained using the 1 mm orifice.

5.4.3 SEM analysis

SEM/EDAX techniques are utilized to analyze the morphology of the particles and confirm the results achieved through SMPS analysis. The sampling is carried out for 15 minutes, by means of 0.1μm pore size MILIPORE© type VCTP filter paper, placed in the main line. It is washed by means of acetone and subjected to sonication for 1 hour to disperse the particles in the solution, as specified in Okyay et al. [159]. Thereafter, the solution is coated on a tape and subjected to SEM and EDAX analysis. Figure 5.9 demonstrates the SEM images of the samples under both non-catalytic and catalytic conditions.

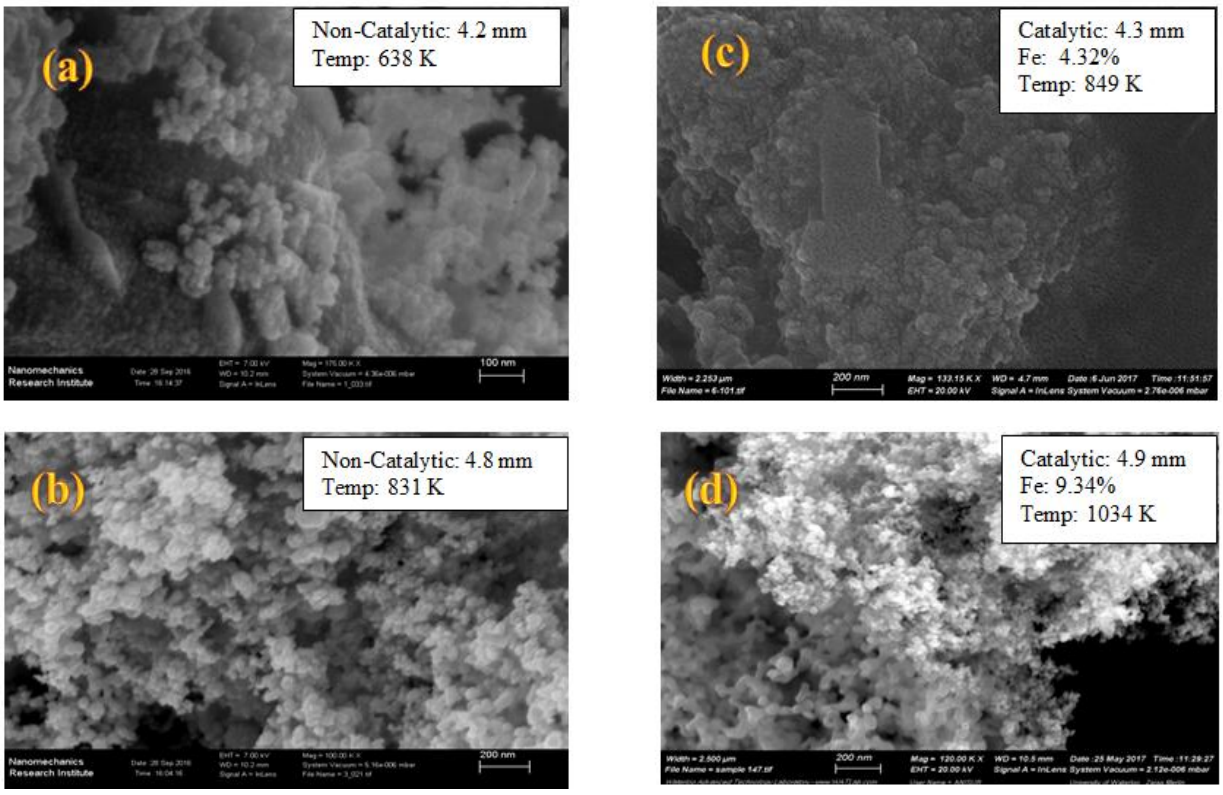

Figure 5.9: SEM Images of samples collected under non-catalytic conditions at axial distance of a) 4.2 mm; b) 4.8 mm; and under catalytic conditions at axial distance of c) 4.3 mm; d) 4.9 mm

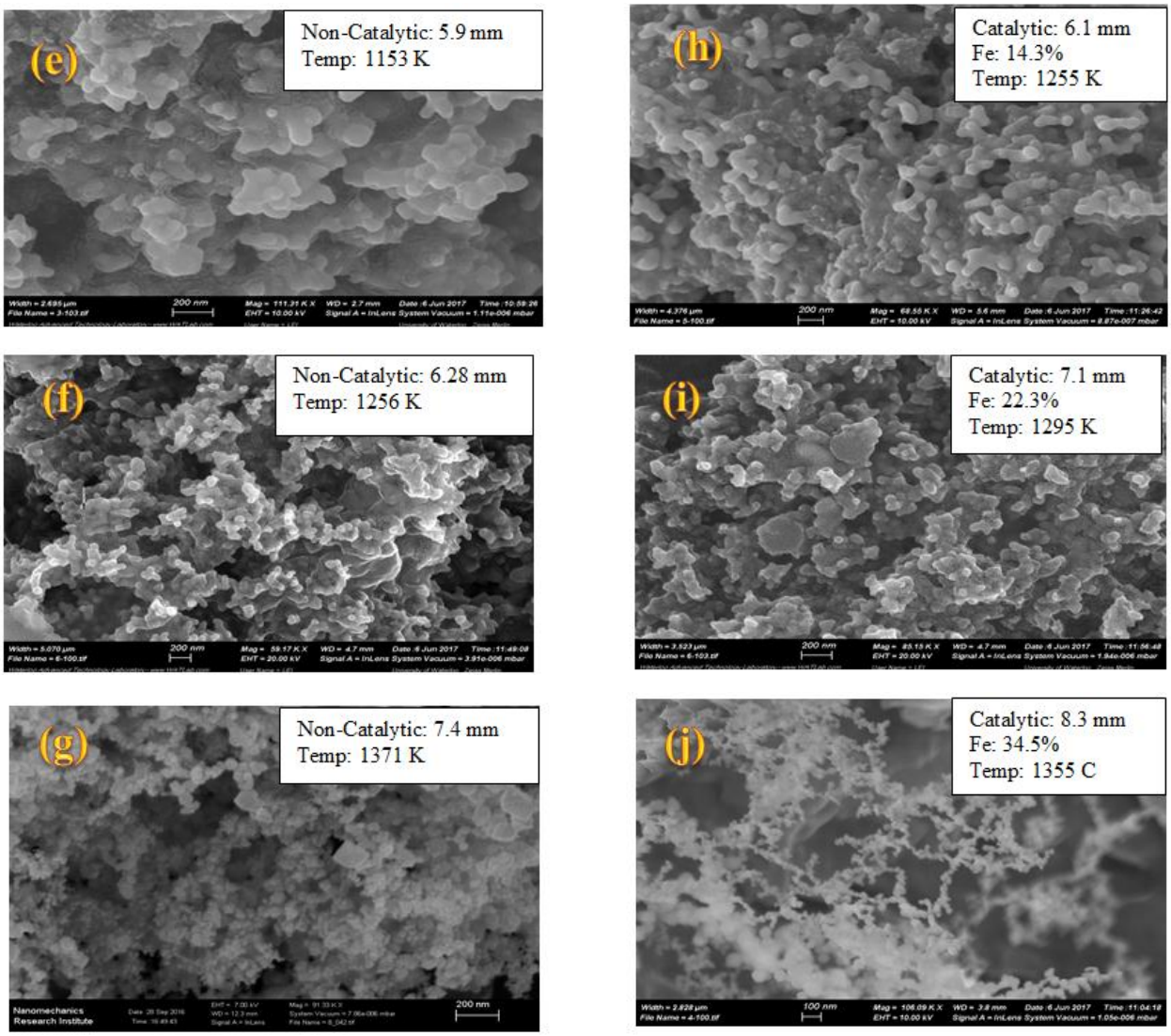

Figure 5.9: SEM Images of samples collected under non-catalytic conditions at axial distance of e) 5.9 mm; f) 6.28 mm; g) 7.4 mm and; under catalytic conditions at axial distance of h) 6.1 mm; i) 7.1 mm and; j) 8.3 mm

Figures 5.9 (a) and (b) showing images of non-catalytic samples at 4.2 and 4.8 mm, respectively, demonstrate cluster-like structures with each particle in the cluster being in the range of 10-30 nm. The small size of the individual particles indicates the dominance of particle inception at this stage of evolution. Samples from the axial distance of 6 mm (Figure 5.9 (e)) are found to be comprised of bigger agglomerates of approximate size 50-80 nm. The transformation of smaller aggregates, in Figures 5.9 (a) and (b), into larger well-defined agglomerates at downstream locations (Figure 5.9 (e)) highlights the occurrence of agglomeration along with extensive surface growth. Close to 6.3 mm in Figure 5.9 (f), the large sized aggregates seen in upstream location are found to start unraveling with many smaller size particles also visible. At regions further downstream and closer to the flame at around 7.5 mm (Figure 5.9(g)), the particle size is greatly reduced, likely, as a result of enhanced presence of oxygen and higher temperatures, since the relatively thinner carbon linkages, which bound different particles into a single aggregate, get oxidized.

At axial locations of 4.3 mm under catalytic conditions, smaller particles of size less than 30 nm are found to predominate as shown in Figure 5.9(c) which are not much different from those seen in the case of non-catalytic samples obtained at approximately similar axial heights. At an axial distance of approximately 5 mm, two distinct particle structures are observed in Figure 5.9(d): one exhibiting a dendritic structure with an indistinct outline; while the other comprising of well-defined particles. The size distribution is tilted towards smaller sized particles with the maximum particle size being close to 60-70 nm. Further downstream at axial distances of approximately 6 mm and 7 mm as shown in Figures 5.9(h) and 5.9(i), particles having a well-defined outline are observed with a strong degree of agglomeration among themselves. It is important to note that the degree of agglomeration is comparatively stronger in Figure 5.9(h), since enhanced oxidation leads to loosening of linkages that bind large aggregates as seen in Figure 5.9(i). In these two figures, the particle size is found to be distributed over a wider range with some bigger aggregates reaching a size of 200 nm. It is important to note the absence of dendritic structure here, which was visible at the earlier upstream location. Closer to the flame at approximately 8 mm in Figure 5.9(j), a

large concentration of relatively small sized particles, arranged in long chains, is observed with their size being around 20 nm. The increasing presence of iron can be attributed to more gas phase iron being incepted on moving closer to the flame.

5.5 Discussion

The use of two different orifice sizes for measuring different parameters enables us to compare the results to determine possible particle loss due to aggregation in the steel tubing. Using equation (5.8) to estimate the degree of coagulation, it was observed that the degree of coagulation does not exceed 1% under both catalytic and non-catalytic conditions. The low degree of coagulation can be attributed to the relatively low particle concentration due to low sooting propensity of methane and significant degree of dilution. The experimental results vindicates the theoretical results as results from both the orifices are much in agreement although the results detected at orifice size of 1 mm demonstrate higher mean particle size along with lower particle concentration, as compared to that under 0.5 mm in Figures 5.3 and 5.4, as well as from Figures B-1 and B-2 in Appendix B. This is most likely due to coagulation among particles in samples having higher particle concentration. In case of measurements using different orifice sizes, more variation in results is witnessed under the catalytic conditions than that under non-catalytic conditions. This indicates other factors like partial clogging of orifice, other than coagulation, to be also at play.

The temperature distributions, under catalytic and non-catalytic conditions, are depicted in Section 3.4 in Chapter 3. Also, the measured particle parameters can be related to the detected gaseous species from Section 3.4 in Chapter 3 to understand the underlying processes. The laminar, diffusion, counterflow flame has a unique structure in which two opposing, high flow-rate streams of fuel and oxidizer, meet at a stagnant plane, close to the mid-plane of the two burner inlets. This causes the fuel stream entering from the fuel port to be gradually heated as it moves towards the stagnation plane. This results in combustion and the resulting high temperature is restricted spatially to a small region close to the mid-plane. Methane is found to react over a large axial region extending from the fuel port to an axial

distance of 8 mm in the case of non-catalytic conditions and 6 mm under catalytic conditions as seen in Section 3.4.1 in Chapter 3 as well as in [160]. Also, the presence of the key soot precursor species, C_2H_2, is also found to extend from an axial location of 4 mm up to the flame under non-catalytic conditions. This ensures the presence of significant amounts of methane even after the initial soot particles are formed and demonstrates that the soot particle inception process occurs concurrently with soot agglomeration and particle growth. This has also been highlighted in the works of Frenklach et al. [161] [162], in which they attributed the spheroid shape of the primary particles to rapid surface growth happening simultaneously with intense particle nucleation.

Under non-catalytic conditions, as the fuel from the fuel inlet port gets heated some of it decomposes to form C_2H_2 [163] [160], an established soot precursor, under the fuel rich conditions and thereby initiates the soot formation as described in Section 2.2.2. The different trends of mean particle size, concentration and distribution at both radial locations in non-catalytic cases highlight the distinct regions where soot inception, particle agglomeration and surface growth process dominate as well as their transition from one dominant regime to another. The soot inception process is initiated around axial distance of 4 mm, at temperatures close to 400 ^{o}C, as confirmed from the presence of small sized particles (<15 nm) from Figures 5.5 and 5.6 and is responsible for the increase in particle concentration upto an axial location of 5 mm with temperature being 650 ^{o}C. While the soot inception temperature is found to be lower than the generally accepted temperature, several latest studies [164] have reported the formation of C_6H_6 structures at around 480 ^{o}C at equivalence ratio of ϕ=3.0. In the present counterflow structure, the equivalence ratios are much higher at the same temperatures leading to greater interaction among the soot precursor species which could have, ultimately, resulted in an earlier inception of soot particles. The soot inception process dominates the, concurrently occurring, soot agglomeration process resulting in an increase in particle concentration despite an increase in mean particle size in the downstream direction upto an axial distance of 5 mm, as seen from Figures 5.3 and 5.4

under non-catalytic conditions. The SEM image in Figure 5.9(a) agrees with the estimated mean particle size.

The agglomeration process gains prominence beyond 5 mm which is demonstrated through the increase in particle size gradient in Figures 5.3 and 5.4. This is also supported by the sudden shift of the particle concentration distribution trends, in Figures 5.5 and 5.6, between 4.5 to 5.5 mm, where the temperature ranges from 420 ^{o}C to 770 ^{o}C, respectively. This shift from around 20-30 nm towards higher diameters close to 50-60 nm, in Figures 5.5 and 5.6, is also verified through the SEM image in Figure 5.9(b). The occurrence of surface growth is observed, in Figures 5.3 and 5.4, in the region between axial distances of 5.5 mm to 6.5 mm, where the temperature ranges from 770 ^{o}C to 989 ^{o}C. This region exhibits relatively invariant particle concentration, while there is a corresponding increase in particle size. Particle surface growth can also be visualized by the gradual shift of the peaks between axial distances of approximately 5.5 mm to 6.5 mm while being spread over the same range of particle size, as seen in Figures 5.5 and 5.6. This is also confirmed from Figure 5.9(e), where the surface growth is causing the boundaries of individual particles in the aggregate to be more indistinct. Contrasting this gradual particle diameter growth in the surface growth regime with the sudden and abrupt increase in the mean particle size close to the fuel port helps in understanding the role of surface growth against that of agglomeration. Beyond 6.5 mm corresponding to temperature of 989^{o} C, the particle size is found to greatly decline as a result of their rapid oxidation.

Under catalytic conditions, it is important to account for the uneven radial spread of precursor from the concentric central tube on the fuel port side. The spread of the injected precursor is restricted closer to the axis near the fuel port but spreads to a greater radial distance at locations closer to the flame. The gas-phase iron pentacarbonyl precursor also undergoes heating in the flame leading to its decomposition into gas phase iron atoms, some of which forms clusters among themselves, while others react with available species to form other iron oxides and hydroxides. Beyond a certain size, these gas phase species would crystallize into incipient particles. From Figure 4.7 in Chapter 4, the presence of gas phase

iron as well as iron oxides is verified at a distance as close as 2.5 mm from the fuel burner, which coincides with the detection of particles at an upstream location under catalytic conditions as seen in Figures 5.3 and 5.4. This results in the possibility of having a mixture of both carbon and iron in the synthesized particles downstream of 2.5 mm under catalytic conditions. While the overall particle concentration at radial distance of 0 mm, under catalytic conditions, is found to be much higher than that under non-catalytic conditions below an axial distance of 5 mm where temperature is 650 ^{o}C, it remains difficult to discern the individual contribution of soot and iron oxide particles. However, taking into consideration the results from Chapter 3, which demonstrated that the gas phase iron species formation occurs simultaneously along with the soot inception process and interferes with it leading to a lesser production of soot [160] through scavenging of radicals, it is quite likely that propagation radical scavenging by gas phase precursor might reduce soot inception. Thus, it can be reasonably deduced that the enhanced particle inception is primarily because of iron oxide particles with soot inception being significantly reduced. [96].

The inception process is found to intensify further downstream as a result of increasing temperature as seen from the increased concentration of small sized particles (<20 nm) detected up to axial distance 5 mm corresponding to a temperature of 780 ^{o}C, as shown in Figures 5.7 and 5.8. The agglomeration process occurs concurrently with the inception process upto an axial distance of 5-6 mm, which corresponds to the temperature range of 780 ^{o}C – 950 ^{o}C. This is illustrated by the increase in both the particle size and concentration seen in Figures 5.3 and 5.4 as well as through the presence of small sized particles detected along with medium sized particles at axial locations within the specified region in Figures 5.7 and 5.8. The presence of two distinct particle structures in Figure 5.9(d) highlights the presence of both soot and iron/iron oxide particles. The dendritic structure having smaller size than the other structure is identified to be that of iron oxide on account of its presence at locations close to the flame in Figure 5.9(j), where most of the soot is expected to be oxidized and from deposited particles on the burner surface shown in Figure B-3 in Appendix B. Surface growth, characterized by an invariant particle concentration and gradual increase in particle

size, is witnessed from axial distances 5 mm to 7 mm, corresponding to the temperature range of 785 ^{o} C to 1020 ^{o}C, similar to the non-catalytic case as seen in Figures 5.3 and 5.4. A significant concentration of particles with size ranging from 30-40 nm is still detected near and at the flame location under catalytic conditions while these parameters are greatly reduced in that region under non-catalytic conditions. This residual particle size and concentration verifies the presence of non-carbon particles (later identified as Fe_2O_3 particles) which are not affected by high temperatures any further while the soot particles formed under non-catalytic conditions are mostly oxidized. The detection of dendritic structure at an axial location of around 5 mm under catalytic conditions as shown in Figure 5.9(d), followed by its absence in the SEM images of samples obtained at downstream locations (Figures 5.9 (h) and 5.9 (i)) and reemergence at location close to flame (Figure 5.9(j)) indicate more effective surface contact between the soot and iron oxide particles which in some cases might lead to the possibility of iron particles being completely encapsulated by carbon. This leads to an enhanced soot oxidation by the iron (Fe)-rich nuclei dispersed among the soot particles under fuel rich conditions in the primary flame region and by the iron oxides (Fe_2O_3 and Fe_3O_4) under fuel lean conditions [95] [96]. This considerably slows down the soot growth process and accelerates soot oxidation, leading to reduced particle size as compared to the non-catalytic case, as seen from Figures 5.3-5.8.

5.6 Uncertainty in experimental analysis

The key sources of error in this study are: i) the perturbation of the flame due to the insertion of sampling tube; ii) the degree of coagulation among particles; iii) wall losses in the sampling tube from the burner to the SMPS; iv) inherent limitations associated with the FCE and the DMA systems of the SMPS; v) errors in temperature measurement due to deposition of iron particles on the thermocouple and; vi) possible errors in determining dilution ratio.

The structure of the counterflow flame is characterized by its confinement within a very small region between the two burners, resulting in reduced occurrences of the sampling tube

disturbing the planar nature of the flame. This, significantly, reduces the perturbation impact of the sampling tube. In order to minimize the actual insertion of the sampling tube into the flame, the tube is rotated so that the orifice faces the flame at locations closer to the flame. While the degree of coagulation is accounted for in this study, the wall losses still remain unaccounted although the significant dilution ratio is expected to ensure the entrainment of the sampled particles. FCE, as claimed by the supplier, is very accurate and can detect particles upto the size of 0.8 nm but the medium-sized DMA has a lower limit of 8 nm. This would lead to the smaller particles being also accounted under the 8 nm channel.

5.7 Summary

Particle sampling from an iron pentacarbonyl seeded methane diffusion counterflow flame is carried out by means of different sizes of orifices and part of the collected sample is diverted to the SMPS device after adequate dilution with nitrogen. The counterflow configuration is ideal for diagnostics for particles as it is capable of producing a stable, planar and two-dimensional diffusion flame front [109] and can provide flexibility in adjusting temperature and concentration gradient. From the results of geometric mean particle size and number concentration, different dominant phases in particle evolution are identified at different axial locations. An increase in the particle inception is observed under catalytic conditions; however, the impact of precursor on soot inception cannot be conclusively predicted, since the individual inception of soot and iron oxide particles, respectively, cannot be discerned. However, accelerated soot oxidation during the soot growth phase offsets the increase in particle size, leading to a faster decline in particle concentration under catalytic conditions and lower mean particle sizes. The results also hint at the possible presence of carbon encapsulated iron nanoparticles under catalytic conditions between axial locations 6-7 mm, exhibiting temperatures ranging from 1200-1300 K. The soot particle is mainly oxidized at the flame but there remains a significant concentration of small sized particles(<20 nm) , being primarily Fe_2O_3, at the flame under catalytic conditions.

Chapter 6

Conclusions and Future Work

6.1 Conclusions

The key contribution of the present work is the exploration of emission reduction potential of $Fe(CO)_5$, as a precursor, on combustion products using an experimental methodology that provides much higher spatial resolution for species and temperature measurement in a more controlled environment by means of a counterflow flame with methane as the primary fuel of interest, although ethanol is also used. The present work has analyzed the impact of $Fe(CO)_5$ precursor on gaseous pollutants like CO, NO as well as on soot particles from a counterflow methane diffusion flame through experimental study while also developing numerical model to study the underlying mechanisms and minor species, primarily that of iron. Experimental infrastructure and methodology are developed to capture the impact of precursor at different stages of the methane combustion process.

The results of the present study demonstrate the potency of iron pentacarbonyl in slowing the: i) particle inception phase by scavenging the reaction propagation radicals and thereby weakening the HACA mechanism for soot formation and; ii) the particle growth phase through enhanced soot oxidation by the iron (Fe)-rich nuclei dispersed among the soot

particles under fuel rich conditions in the primary flame region and by the iron oxides (Fe_2O_3 and Fe_3O_4) particles under fuel lean conditions. While the catalytic activity of iron oxide (Fe_2O_3) particles is amply documented, the present research has tried to bridge the gap in the literature about the process of precursor initiated particle evolution in the flame and its impact on emission reduction. The results demonstrate various regimes of particle growth at various axial locations. Addition of iron pentacarbonyl leads to enhanced production of relatively much small sized iron oxide particles as compared to the bigger soot particles, which would enhance the contact surface between soot and catalyst species and thereby enhance the catalytic oxidation of soot.

A detailed iron reaction mechanism is incorporated into the numerical model of the counterflow burners, with the boundary conditions being derived from the operating parameters from the experimental study, to analyze the role of iron species in reducing the emissions from the flame. The interaction between the methane combustion chemistry and the key gas phase iron species (FeO, FeO_2, FeOH and $Fe(OH)_2$) is explored spatially at different temperatures. While increasing the precursor concentration enables enhanced radical scavenging, higher temperatures as a result of higher hydrocarbon fuel fractions could offset the impact of radical scavenging process on account of the enhanced radical production.

6.2 Recommendations for future work

Future studies focusing on the behavior of iron pentacarbonyl in emission reduction at various pressures, representative of real-time conditions in various combustors like engines as well as in the exhaust system in automobiles, need to be studied. Different pressures can significantly impact the reaction rates of key pathways in the mechanism governing the iron species, the methane combustion mechanism and their interaction. Another possible area of exploration could be the use of iron pentacarbonyl under higher hydrocarbons like isooctane, heptane or a blend of them, representing existing fuels, under realistic operating conditions would provide more information about the emission reduction potential.

Metals, on account of their high energy density, are already being used as propellants, additives and explored as potential fuels [165]. While previous attempts to introduce metals to flames have also involved the injection of metal particles and metal dust directly to the flame, these approaches have not been as successful due to logistical issues related to their scaling up to industrial standards as well as safety concerns. Injection of metal precursors, either in liquid or vapor state, to the flame is an existing technique being currently utilized for industrial-scale production of metal/metal oxide catalyst particles [152]; however, analyzing this process as an energy source through metal combustion deserves merit and needs more fundamental investigation.

Though the present work could not identify the percentage of soot particles among the enhanced particle concentration detected under catalytic conditions, it clearly demonstrated the slowing of particle size growth followed by its reversal under catalytic conditions due to the smaller catalytic role played iron/iron oxide nuclei embedded among soot particles. A potential area for research could be the exploration of the impact of iron precursor injection after soot particle inception has occurred. In practical terms, this could mean analyzing the impact of iron precursor injection between the cylinder exhaust and the diesel particulate filter.

The mechanism of surface chemistry of metal catalysts is still an active area for research and since iron remains a relatively benign and abundantly available metal, identifying and presenting its detailed mechanism for surface chemistry still remains a challenge. Incorporating the heterogeneous catalytic mechanism occurring on the surface of iron oxide (Fe_2O_3) into the existing numerical model accounting for just the gas phase reactions will be a major step towards accurate prediction of emission reduction.

List of Publications

Publications Referring to the Topic of Current Ph.D. Thesis

- ***Raj A.***, Pan K., Qi H., Zhu H., Wen J.Z., Croiset E. (2015). Effects of an Iron Pentacarbonyl Additive on Counterflow Natural Gas and Ethanol Flames. Energy & Fuels, vol. 29, no. 8, pp. 5361-5371.
- ***Raj A.,*** Wen J.Z., El Sayed A., Croiset E. (2017). Numerical analysis of hydrocarbon and nitric oxide emission reduction from iron pentacarbonyl loaded counterflow natural gas flame. Submitted to Fuel, June 2017. Manuscript number: JFUE-S-17-02767
- ***Raj A.,*** Zhu D., Wen J.Z., Tan Z., Croiset E. (2017). Particle sampling and analysis of the particle evolution process in an iron pentacarbonyl loaded counterflow natural gas flame. Currently under preparation.

Bibliography

[1] Barfknecht TR., "Toxicology of soot," *Progress in Energy Combustion Science,* vol. 9, pp. 199-237, 1983.

[2] Hodnebrog Ø., Myhre G., Samset BH., "How shorter black carbon lifetime alters its climate effect," *Nature Communications,* vol. 5, no. 5065, 2014.

[3] Solomon S., " Stratospheric ozone depletion: A review of concept," *Reviews of Geophysics,* vol. 37, pp. 275-316, 1999.

[4] Vitousek PM., Aber JD., Howarth RW., Likens GE.,Matson PA.,Tilman DG., "Human alteration of the global nitrogen cycle: sources and consequences," *Ecological Applications,* vol. 7, no. 3, pp. 737-750, 1997.

[5] US Energy Information Administration, "Annual Energy Review 2011," 2012.

[6] Hagen J., Industrial Catalysis (2nd Edition), 2006.

[7] Pratsinis SE., "Flame aerosol synthesis of aerosol powders," *Progress in Energy and Combustion Science,* vol. 24, p. 197, 1998.

[8] Stratakis GA.,Stamatelos AM., "Thermogravimetric analysis of soot emitted by a modern diesel engine run on catalyst-doped fuel," *Combustion and Flame,* vol. 132, pp. 157-169, 2003.

[9] Tijare SN., Bakardjieva S., Subrt J.,Joshi MV., Rayalu SS.,Hishita SS.,Labhsetwar N. , "Synthesis and visible light photocatalytic activity of nanocrystalline PrFeO3 perovskite for hydrogen generation in ethanol–water system," *Journal of Chemical Science,* vol. 126, no. 2, pp. 517-525, 2014.

[10] Zhang Z-H., Balasubramanian R., "Influence of an iron-based fuel-borne catalyst on physicochemical and toxicological characteristics of particulate emissions from a diesel engine," *Applied Energy,* vol. 146, pp. 270-278, 2015.

[11] Nash DG., Swanson NB.,Preston WT., Yelverton TLB.,Roberts WL., Wendt JOL.,Linak WP., "Environmental implications of iron fuel borne catalysts and their effects on diesel particulate formation and composition," *Journal of Aerosol Science,* vol. 58, pp. 50-61, 2013.

[12] Huber DL., "Synthesis, Properties, and Applications of Iron Nanoparticles," *Small : review,* vol. 1, no. 5, pp. 482-501, 2005.

[13] Schwarz JA., "Methods for preparation of catalytic materials," *Chemical reviews,* vol. 95, p. 477, 1995.

[14] Strobel R., Stark WJ.,Madler L.,Pratsinis SE.,Baiker A., "Flame-made platinum/alumina: Structural properties and catalytic behaviour in enantioselective hydrogenation," *Journal of Catalysis,* vol. 213, no. 2, p. 296, 2003.

[15] Strobel R.,Pratsinis SE.,Baiker A., "Flame-made Pd/La2O3/Al2O3 nanoparticles: Thermal stability and catalytic behavior in methane combustion," *Journal of Material Chemistry,* vol. 15, no. 5, p. 605, 2005.

[16] Madler L.,Stark WJ., Pratsinis SE., *Journal of Material Research,* vol. 17, p. 1356, 2002.

[17] Pfromm PH., Amanor-Boadu V., Nelson R., Vadlani P., Madl R., "Bio-butanol vs. bio-ethanol: A technical and economic assessment for corn and switchgrass fermented by yeast or Clostridium acetobutylicum," *Biomass and Bioenergy,* vol. 34, no. 4, pp. 515-524, 2010.

[18] Turns SR., An Introduction to Combustion: Concepts and Applications, 2nd edition ed., McGraw Hill, 2000.

[19] Puri I., Seshadri K., Smooke M., Keyes D., "A comparison between numerical calculation and experimental measurements of the structure of a counterflow methane-air diffusion flame," *Combustion Science and Technology,* vol. 56, pp. 1-22, 1987.

[20] Khanna V., Goel R., Ellzey J., "Measurements of emissions and radiations for methane

combustion within a porous medium burner," *Combustion Science and Technology,* vol. 99, pp. 133-142, 1994.

[21] Glarborg P., Kee RJ.,Grcar JF.,Miller JA.,, "PSR: A fortran program for modeling well-stirred reactors," Sandia National Laboratories SAND86-8209, 1986.

[22] Peters N., Kee RJ., "The computation of stretched laminar methane-air diffusion flames using a reduced four-step mechanism," *Combustion and Flame,* vol. 68, pp. 17-29, 1987.

[23] C. HJ., "Detailed Chemical inetic modeling;Is there life after GRI Mech 3.0?," *Preprint of papers- American Chemical Society, Division of Fuel Chemistry,* vol. 49, no. 1, p. 264, 2004.

[24] Smith GP., Golden DM., Frenklach M., Moriarty NW., Eiteneer B.,l Goldenberg M., Bowman CT., Hanson RK.,Song S.,Gardiner Jr. WC., Lissianski VV., Qin Z., "GRI Mech 3.0," [Online]. Available: http://www.me.berkeley.edu/gri-mech/version30/text30.html. [Accessed 12 July 2014].

[25] Saxena P., Williams FA. , "Testing a small detailed chemical-kinetic mechanism for the combustion of hydrogen and carbon monoxide," *Combustion and Flame,* vol. 145, no. 1-2, pp. 316-323, 2006.

[26] Waly MMY., Li SC., Williams FA., "Experimental and Numerical Studies of Two-Stage Ethane-Air Flames," *Journal of Engineering for Gas Turbines and Power* , vol. 122, no. 4, pp. 651-658, 2000.

[27] Varatharajan B., Williams FA., "Ethylene Ignition and Detonation Chemistry, Part 1: Detailed Modeling and Experimental Comparison," *Journal of Propulsion and Power,* vol. 18, no. 2, pp. 344-351, 2002.

[28] Waly MMY., Li SC., Williams FA., "Structures of non-sooting counterflow diluted acetylene-air flames," *Proceedings of the Combustion Institute,* vol. 28, no. 2, pp. 2005-2012, 2000.

[29] Petrova MV., Williams FA., "A small detailed chemical-kinetic mechanism for hydrocarbon combustion," *Combustion and Flame,* vol. 144, no. 3, pp. 526-544, 2006.

[30] Li SC., Williams FA., *Proceedings of Combustion Institute ,* vol. 26, pp. 1017-1024, 1996.

[31] Li SC., Williams FA., "NOx formation in two-stage methane–air flames," *Combustion and Flame,* vol. 118, no. 3, pp. 399-414, 1999.

[32] Li J., Kazakov A., Dryer FL., "Experimental and Numerical Studies of Ethanol chemical kinetics," *Journal of Physical Chemistry A,* vol. 108, no. 38, pp. 7671-7680, 2004.

[33] Saxena P.,Williams FA., "Numerical and Experimental studies of ethanol flames," *Proceedings of the combustion institute,* vol. 31, no. 1, pp. 1149-1156, 2007.

[34] "The Particle Pollution Report," United States Environmental Protection Agency: Current Understanding of Air Quality and Emissions through 2003, 2003.

[35] Drake MC.,Blint RJ., "Calculations of NOx formation pathways in propagating laminar, high pressure premixed CH4/Air flames," *Combustion Science and Technology,* vol. 75, pp. 261-285, 1991.

[36] Drake MC.,Blint RJ., "Relative Importance of Nitric Oxide formation mechanisms in laminar opposed flow diffusion flames," *Combustion and Flame,* vol. 83, pp. 185-203, 1991.

[37] Correa SM., "A review of NOx formation under gas-turbine combustion conditions," *Combustion Science and Technology,* vol. 87, pp. 329-362, 1992.

[38] Fenimore CP., "Formation of Nitric Oxide in Premixed Hydrocarbon flames," in *Thirteenth Symposium (International) on Combustion, The Combustion Institute*, Pittsburgh, 1970.

[39] Miller JA., Bowman CT., "Mechanism and modeling of nitrogen chemistry in combustion," *Progress in Energy and ombustion Science ,* vol. 15, pp. 287-338, 1989.

[40] Bowman CT., "Control of combustion generated nitrogen oxide emissions:Technology Driven by Regulations," in *Twenty Fourth symposium (International) on combustion*, The combustion Institute, Pittsburgh, 1992.

[41] Fahr A., Stein SE., *Proceedings of Combustion Institute* , vol. 22, pp. 1023-1029, 1988.

[42] Krestinin AV., "Detailed modeling of soot formation in hydrocarbon pyrolysis," *Combustion and Flame,* vol. 121, no. 3, pp. 513-524, 2000.

[43] Indarto A., "Soot Growth Mechanisms from Polyynes," *Environmental Engineering Science,* vol. 26, pp. 1685-1691, 2009.

[44] Glassman I.,Yetter R., Combustion, Academic Press 2008.

[45] Rubino L., "The effect of oxygenated additives on soot precursor formation," 2001.

[46] Sarathy SM., "Using an opposed flow diffusion flame to study the oxidation of C4 fatty acid methyl esters," 2006.

[47] Frenklach M, Wang H, "Detailed mechanism and modeling of soot particle formation.," *Springer-Verlag GmbH & Company KG,* 1994.

[48] D'Anna A, Violi A, D'Alessio A, Sarofim AF., "A reaction pathway for nanoparticle formation in rich premixed flames," *Combustion and Flame,* vol. 127, no. 1-2, pp. 1995-2003, 2001.

[49] Friedlander SK., Smoke, dust, and haze : fundamentals of aerosol dynamics, New York, 2000.

[50] Megaridis CM, Dobbins RA., "Soot aerosol dynamics in a laminar ethylene diffusion flame," in *Intenational Symposium of Combustion*, 1989.

[51] Dobbins RA., Fletcher RA., Lu W., " Laser microprobe analysis of soot precursor particles and carbonaceous soot," *Combustion and Flame,* vol. 100, no. 1-2, pp. 301-309, 1995.

[52] Appel J., Bockhorn H., Frenklach M., "Kinetic modeling of soot formation with detailed chemistry and physics: laminar premixed flames of C2 hydrocarbons,"

Combustion and Flame, vol. 121, pp. 122-136, 2000.

[53] Yetter RA., Risha GA., Son SF., "Metal particle combustion and nanotechnology," *Proceedings of Combustion Institute ,* vol. 32, pp. 1819-1838, 2009.

[54] Granier JJ., Pantoya ML., "Laser ignition of nanocomposite thermites," *Combustion and Flame,* vol. 138, pp. 373-383, 2004.

[55] Dreizin EL., "Metal-based reactive nanomaterials," *Progress in Combustion Science,* vol. 35, pp. 141-167, 2009.

[56] Marinov N.,Pitz W.,Westbrook C.,Lutz A., Vincitore A., Senkan A., "Chemical kinetic modeling of a methane opposed-flow diffusion flame and comparison to experiments," *Symposium (International) on Combustion ,* vol. 27, no. 1, pp. 605-613, 1998.

[57] Smyth KC., Miller JH., Dorfman RC., Mallard WG., Santoro RJ., "Soot inception in a methane/air diffusion flame as characterized by detailed species profile," *Combustion and Flame,* vol. 62, no. 2, pp. 57-181, 1985.

[58] Hahn W., Wendt J., "NOx formation in flat, laminar, opposed jet methane diffusion flames," *Symposium (International) on Combustion ,* vol. 18, no. 1, pp. 121-131, 1981.

[59] Blevins LG., Gore JP., "Computed structure of low strain rate partially premixed CH4/air counterflow flames:implications for NO formation," *Combustion and Flame ,* vol. 116, no. 4, pp. 546-566, 1999.

[60] Beltrame A., Porshnev P., Merchan-Merchan W., Saveliev A., Fridman A., Kennedy L., "Soot and NO formation in methane-oxygen enriched diffusion flames," *Combustion and Flame,* vol. 124, no. 1, pp. 295-310, 2001.

[61] Dupont V., Williams A., "NOx mechanisms in rich methane-air flames," *Combustion and Flame ,* vol. 114, no. 1, pp. 103-118, 1998.

[62] Bechtold RL., Timbario TJ., Miller MT., Urban C., "Performance andemissions of a DDC 8V-71 transit bus engine using ignition-improved methanol and ethanol," *SAE Technical Paper Series,* vol. 912356, 1991.

[63] Spreen K., "Evaluation of oxygenated diesel fuels.," South West Research Institute, San Antonio, Texas, 1999.

[64] Cole RL., Poola B., Sekar R., Schaus JE., McPartlin P., "Effects of ethanol additives on diesel particulates and NOx emissions," *SAE Technical paper series* , Vols. 2001-01-1937, 2001.

[65] Gjirja S., Olsson E., Karistrom, A., "Considerations on engine design and fuelling technique effects on qualitative combustion in alcohol diesel engines," *SAE Technical paper series* , vol. 982530, 1998.

[66] Hansdah D., Murugan S., "Bioethanol fumigation in a DI diesel engine," *Fuel,* vol. 130, pp. 324-333, 2014.

[67] Jamuwa DK., Sharma D., Soni SL., "Performance, emission and combustion analysis of an ethanol fuelled stationary CI engine," *Biofuels,* vol. 10.1080/17597269.2016.1163213, pp. 1-14, 2016.

[68] Abdelouahab-Reddam Z., ElMail R., Coloma F., Sepúlveda-Escribano A., "Effect of the metal precursor on the properties of Pt/CeO2/C catalysts for the total oxidation of ethanol," *Catalysis Today,* vol. 249, pp. 109-116, 2015.

[69] Lee JH. , Trimm DL., "Catalytic combustion of methane," *Fuel Processing Technology,* vol. 42, no. 2, pp. 339-359, 1995.

[70] Baldi M., Escribano VS., Amores JMG.,Milella F., "Characterization of manganese and iron oxides as combustion catalysts for propane and propene," *Aplied catalysis B:Environmental,* vol. 17, no. 3, pp. L175-L182, 1998.

[71] Sazonov V.,Ismagilov Z., Prokudina N., "Catalytic combustion of lean methane- air mixtures," *Catalysis Today,* vol. 47, no. 1, pp. 149-153, 1999.

[72] Kannan GR., Karvembu R.,Anand R., "Effect of metal based additive on performance emission and combustion characteristics of diesel engine fuelled with biodiesel," *Applied Energy,* vol. 88, pp. 3694-3703, 2011.

[73] Fazliakmetov R., Shpiro G., "Selection and manufacture technology of antismoke additives for diesel fuel and boiler fuels oils," *Izdetal Stvo Neft I Gaz,* vol. 4, p. 43, 1995.

[74] Skillas G., Qian Z., Baltensperger U., Matter U., & Burtscher H., "The influence of additives on the size distribution and composition of particles produced by diesel engine," *Combustion Science and Technology,* vol. 154, p. 259–273, 2000.

[75] Miller A., Ahlstrand G., Kittelson D., Zachariah M. , "The fate of metal (Fe) during diesel combustion: Morphology, chemistry, and formation pathways of nanoparticles," *Combustion and Flame,* vol. 149, no. 1-2, pp. 129-143, 2007.

[76] Gonzalez-Carreno T., Morales MP.,Gracia M.,Serna CJ, "Preparation of uniform Y-Fe203 particles with nanometer size by spray pyrolysis," *Materials Letters,* vol. 18, pp. 151-155, 1993.

[77] Grimm S., "Flame pyrolysis – a preparation route for ultrafine pure c-Fe2O3 powders and the control of their particle size and properties," *Journal of Material Science,* vol. 32, pp. 1083-1092, 1997.

[78] Kagawa M.,Honda F.,Onodera H. , Nagae T., *Materials research Bulletin ,* vol. 18, p. 1087, 1983.

[79] Janzen C., Roth P., "Formation and Characteristics of Fe2O3 Nano-Particles in Doped Low Pressure H2/O2/Ar Flames," *Combustion and Flame,* vol. 125, no. 3, pp. 1150-1161, 2001.

[80] Yu F.,Wang JN., Sheng ZM.,Su LF, "Synthesis of carbon-encapsulated magnetic nanoparticles by spray pyrolysis of iron carbonyl and ethanol," *Carbon,* vol. 43, pp. 3002-3039, 2005.

[81] Lu Y, Zhu ZP, Liu ZY, "Carbon-encapsulated Fe nanoparticles from detonation-induced pyrolysis of ferrocene," *Carbon ,* vol. 43, no. 2, pp. 369-374, 2005.

[82] Ma Y., Zhu M., Zhang D., "The effect of a homogeneous combustion catalyst on

exhaust emissions from a single cylinder diesel engine," *Applied Energy,* vol. 102, pp. 556-562, 2013.

[83] P. I. E. E. A. A. J. Marsh ND., "Evaluation of organometallic fuel additives for soot suppression," *Combustion Science Technology,* vol. 179, pp. 987-1001, 2007.

[84] Song J., Wang J., Boehman AL., "The role of fuel borne catalyst in diesel particulate oxidation behavior," *Combustion and Flame,* vol. 146, pp. 73-84, 2006.

[85] Pivkina A., Ulyanova P., Frolov Y., Zavyalov S.,Schoonman J., "Nanomaterials for heterogeneous combustion," *Propellents, Explos, Pyrotech,* vol. 29, pp. 39-48, 2004.

[86] Jayaraman K., Anand K., Chakravarthy S., Sarathi R., "Production and characterization of nano-aluminum and its effects in solid propellant combustion," *45th AIAA aerospace sciences meeting and exhibit* , p. 1430, 2008.

[87] Selvan VAM., Anand R., Udayakumar M., "Effects of cerium oxide nanoparticle addition in diesel and diesel-biodiesel-ethanol blends on the performance and emission characteristics of a CI engine," *Journal of Engineering and Applied Sciences,* vol. 4, p. 1819, 2009.

[88] Reichert D., Bockhorn H., Kureti, S. , "Study of the reaction of NOx and soot on Fe2O3 catalyst in excess of O2.," *Applied Catalysis B: Environmental* , vol. 80, pp. 248-259, 2008.

[89] Fennel PS., Hayhurst AN., "The kinetics of the reduction of NO to N2 by reaction with particles of Fe," *Proceedings of the Combustion Institute,* vol. 29, pp. 2179-2185, 2002.

[90] Reinelt D., Linteris G., "Experimental study of the inhibition of premixed and diffusion flames by iron pentacarbonyl," in *26th Symposium (International) on Combustion, The Combustion Institute.*, Pittsburgh, 1996.

[91] Rumminger MD.,Reinelt D., Babushok V., Linteris GT., "Numerical study of the inhibition of premixed and diffusion flames by iron pentacarbonyl," *Combustion and Flame,* vol. 116, no. 1-2, pp. 207-219, 1999.

[92] Linteris GT.,Babushok VI.,, "Promotion or inhibition of hydrogen-air ignition of iron containing compounds," *Proceedings of Combustion Institute,* vol. 32, no. 2, pp. 2535-2542, 2009.

[93] Park K., Bae GT., Shin KS., *Bulletin of Korean Chemical Society* , vol. 23, no. 2, 2002.

[94] Celnik M.,West R., Morgan N.,Kraft M.,Moisala A.,Wen J.,Green W.,Richter H., "Modelling gas-phase synthesis of single-walled carbon nanotubes on iron catalyst particles," *Carbon,* vol. 46, pp. 422-433, 2008.

[95] Kim KB., Masiello KA., Hahn DW., "Reduction of soot emissions by iron pentacarbonyl in isooctane diffusion flames," *Combustion and Flame,* vol. 154, pp. 164-180, 2008.

[96] Kim K., Hahn DW., "Interaction between iron based compound and soot particles in diffusion flame," *Energy,* vol. 116, pp. 933-941, 2016.

[97] Zhang J.,Megaridis CM., "Soot suppression by ferrocene in laminar ethylene/air non-premixed flames.," *Combustion and Flame,* vol. 105, no. 4, pp. 528-540, 1996.

[98] Rumminger MD., Linteris GT., *Combustion and Flame* , vol. 128, pp. 145-164, 2002.

[99] Giesen A.,Herzler J.,Roth P., *Journal of Physical Chemistry A,* vol. 107, p. 5202, 2003.

[100] Krestinin AV., Smirnov VN., Zaslonko IS.,, *Soviet Journal of Chemical Physics,* vol. 8, p. 689, 1991.

[101] Jensen DE.,Jones GA., "Catalysis of radical recombination in flames by iron," *The Journal of Chemical Physics,* vol. 60, p. 3421, 1974.

[102] Wen JZ.,Goldsmith CF., Ashcraft RW.,Green WH., "Detailed Kinetic Modeling of Iron Nanoparticle Synthesis from the Decomposition of Fe(CO)5," *The Journal of Physical Chemistry C,* vol. 111, pp. 5677-5688, 2007.

[103] Kluge S., Deng L.,Feroughi O., Schneider F., Poliak M., Fomin A., Tsionsky V., Cheskis S., Wlokas I., Rahinov I., Drier T.,Kempf A.,Wiggers H., Schulz C., "Initial reaction steps during flame synthesis of iron oxide nanoparticles," *CrystEngCom,* vol.

17, no. 36, pp. 6930-6939, 2015.

[104] Poliak M., Fomin A., Tsionsky V.,Cheskis S., Wlokas I., Rahinov I., "On the mechanism of nanoparticle formation in a flame doped with iron pentacarbonyl," *Phys.Chem.Chem.Phys,* vol. 17, pp. 680-685, 2015.

[105] Wlokas I., Faccinetto A., Tribalet B., Schulz C., Kempf A., "Mechanism of iron oxide formation from iron pentacarbonyl doped low pressure hydrogen/oxygen flames," *International Journal of Chemical Kinetics,* vol. 45, no. 8, pp. 487-498, 2013.

[106] Peters N., "Laminar flamelet concepts in turbulent combustion," *21st symposium (international) on combustion* , pp. 1231-1250, 1986.

[107] Peters N., "Laminar diffusion flamelet models in non-premixed turbulent combustion," *Progress in Energy and Combustion Science,* vol. 10, pp. 319-339, 1984.

[108] Shengteng Hu, "PhD thesis: Measurements and modeling of non-premixed tubular flames: structure, extinction and stability," Graduate School of Vanderbilt University, 2007.

[109] Mani Sarthy S., Niemann U., Yeung C., Gehmlich R., Westbrook CK., Plomer M., Luo Z., Mehl M., Pitz WJ., Seshadri K., Thomson MJ., Lu T., "A counterflow diffusion flame study of branched octane isomers," *Proceedings of the Combustion Institute,* vol. 34, pp. 1015-1023, 2013.

[110] Tsuji H., "Counterflow diffusion flames," *Progress in Energy and Combustion Science,* vol. 8, no. 2, pp. 93-119, 1982.

[111] Pandya TP.,Weinberg, FJ., *Ninth symposium (international) on combustion,* pp. 587-596, 1963.

[112] Otsuka Y., Niioka, T., "Deviation of the flame from the stagnation point in opposed jet diffusion flame," *Combustion and Flame,* vol. 19, no. 2, pp. 171-179, 1972.

[113] Yi X., Lee CFF., "Forward-illumination light-extinction technique for soot measurement," *Applied Optics,* vol. 5, no. 9, pp. 2046-2057, 2006.

[114] Yang B., Hu B., Koylu UO., "Mean soot volume fractions in turbulent hydrocarbon flames: A comparison of sampling and laser measurements," *Combustion Science and Technology,* vol. 177, no. 8, pp. 1603-1626, 2005.

[115] Sipkens TA.,Mansmann R.,Daun KJ.,Petermann N., Titantah JT., Karttunen M.,Wiggers H.,Dreier T.,Schulz C., "In situ nanoparticle size measurements of gas-borne silicon nanoparticles by time-resolved laser-induced incandescence," *Applied Physics B Laser and Optics,* vol. 116, no. 3, pp. 623-636, 2014.

[116] Sipkens T.,Joshi G.,Daun KJ.,Murakami Y., "Sizing of Molybdenum Nanoparticles Using Time-Resolved nanoparticles by time-resolved laser-induced incandescence," *Journal of Heat Transfer,* vol. 135, no. 5, 2013.

[117] Sipkens TA.,Mansmann R.,Daun KJ.,Petermann N., Titantah JT., Karttunen M.,Wiggers H.,Dreier T.,Schulz C., "In situ nanoparticle size measurements of gas-borne silicon nanoparticles by time-resolved laser-induced incandescence," *Applied Physics B Laser and Optics,* vol. In Press, no. DOI 10.1007/s00340-013-5745-2, 2014.

[118] Tribalet B., Faccinetto A., Dreier T., Schulz C., "Evaluation of particle size of iron oxide nano particles in a low pressure flame synthesis reactor by simultaneous application of TiRe-LII and PMS," in *5th International Workshop on Laser-Induced Incandescence*, Le Touquet, france, 2012.

[119] Krishnan SS., Lin KC., Faeth GM., "Optical properties in the visible of overfire soot in large buoyant turbulent diffusion flames.," *Optical properties in the visible of overfire soot in large buoyant turbulent diffusion flames.*, vol. 122, no. 3, pp. 517-524, 2000.

[120] Chang H., Charalampopoulos T T., "Determination of the wavelength dependence of refractive indexes of flame soot.," *Proceedings of the Royal Society of Mathematical and Physical Sciences,* vol. 430, no. 1880, pp. 577-591, 990.

[121] Chowdhury S., Boyette WR., Roberts WL., "Time-averaged probability density functions of soot nanoparticles along the centerline of a piloted turbulent diffusion flame using a scanning mobility particle sizer," *Journal of aerosol science,* vol. 106,

pp. 56-67, 2017.

[122] Santoro RJ., Shaddix CR., Laser-induced incandescence, New York: Taylor and Francis, 2002.

[123] Stirn R. , Baquet TG. , Kanjarkar S. , Meier W. , Geigle KP., Grotheer HH., "Comparison of Particle Size Measurements with Laser-Induced Incandescence, Mass Spectroscopy, and Scanning Mobility Particle Sizing in a Laminar Premixed Ethylene/Air Flame," *Combustion Science and Technology,* vol. 181, no. 2, pp. 329-349, 2009.

[124] Grotheer HH., Pokorny H., Barth KL., Thierley M., Aigner M., " Mass spectrometry up to 1 million mass units for simultaneous detection of primary soot and of soot precursors (nanoparticles) in flames," *Chemosphere,* vol. 57, p. 1335, 2004.

[125] Zhao B., Yang Z., Johnston MV., Wang H., Wexler AS., Balthasar M.,Kraft M., "Measurement and numerical simulation of soot particle size distribution functions in a laminar premixed ethylene-argon flame," *Combustion and Flame,* vol. 133, pp. 173-188, 2003.

[126] Abid AD., Heinz N., Tolmachoff ED., Phares DJ., Campbell CS., Wang H., "On evolution of particle size distribution functions of incipient soot in premixed ethylene–oxygen–argon flames," *Combustion and Flame,* vol. 154, pp. 775-788, 2008.

[127] Cain JP., Gassman PB., Wang H., Laskin A., "Micro-FTIR study of soot chemical composition—evidence of aliphatic hydrocarbons on nascent soot surfaces," *Physical Chemistry Chemical Physics,* vol. 12, no. 20, pp. 5173-5488, 2010.

[128] Cain JP., Camacho J.,Phares DJ., Wang H., Laskin A., "Evidence of aliphatics in nascent soot particles in premixed ethylene flames," *Proceedings of the Combustion Institute,* vol. 33, pp. 533-540, 2011.

[129] Burtscher H., Matter D., Siegmann HC., "Measurement of size distribution and photoelectric activity of particles in a gas diffusion flame," *Atmospheric environment,* vol. 27A, no. 8, pp. 1255-1259, 1993.

[130] Hepp H., Siegmann K., "Mapping of Soot Particles in a Weakly Sooting Diffusion Flame by Aerosol Techniques," *Combustion and Flame ,* vol. 115, pp. 275-283, 1998.

[131] Kasper M., Siegmann K., Sattler K., "Evaluation of an in situ Sampling Probe for its Accuracy in Determining Particle Size Distributions from Flames," *Journal of Aerosol Science,* vol. 28, pp. 1569-1578, 1997.

[132] Lasher SW., "Ultrafine Soot Investigation in Flames," Massachussets Institute of Technology, 1999.

[133] Maricq MM., Harris SJ.,Szent J., "Soot Size Distribution in Rich Premixed Ethylene Flames," *Combustion and Flame ,* vol. 132, no. 3, pp. 328-342, 2003.

[134] Siegmann K., Hepp H., Sattler K., "Reactive dimerization: a new PAH growth mechanism in flames," *Combustion Science and Technology,* vol. 109, pp. 165-181, 1995.

[135] Kazemimanesh M., Moallemi A., Olfert JS., Kostiuk LW., "Probe sampling to map and characterize nanoparticles along the axis of a laminar methane jet diffusion flame," *Proceedings of combustion institute,* vol. 36, no. 1, pp. 881-888, 2017.

[136] Burner diagram, www.flatflame.com. [Online]. Available: http://www.flatflame.com/bronze.htm.

[137] Gilbert AG.,Sulzmann KGP., "The Vapor Pressure of Iron Pentacarbonyl," *Journal of Electrochemical Society:Solid state science and Technology*, vol. 121, no. 6, 1974.

[138] Seshadri K., Lu T., Herbinet O., Humer S., Niemann U., Pitz WJ., Seiser R., Law CK., "Experimental and kinetic modeling study of extinction and ignition of methyl decanoate in laminar non-premixed flows," *Proceedings of Combustion Institute,* vol. 32, no. 1, pp. 1067-1074, 2009.

[139] Frenklach M., "Reaction mechanism of soot formation in flames.," *Physical Chemistry Chemical Physics*, vol. 4, no. 11, pp. 2028-2037, 2002.

[140] Roberts IL.; Coney JER., Gibbs BM. , "Estimation of radiation losses from sheathed

thermocouples," *Applied Thermal Engineering* , vol. 31, no. 14-15, pp. 2262-2270 , 2011.

[141] Sarthy SM., Oßwald P., Hansen N., Kohse-Hoinghaus K. , "Alcohol combustion chemistry," *Progress in Energy and Combustion Science* , vol. 44, pp. 40-102, 2014.

[142] Feroughi OM., Hardt S., Wlokas I, Hulser T., Wiggers H., Dreier T., Schulz C., "Laser-based in situ measurement and simulation of gas-phase temperature and iron atom concentration in a pilot-plant nanoparticle synthesis reactor," *Proceedings of the Combustion Institute* , vol. 35, pp. 2299-2306, 2015.

[143] Lee JH., Trimm DL. , "Catalytic combustion of methane," *Fuel Processing Technology,* vol. 42, no. 2, pp. 339-359, 1995.

[144] Park J. , Zhu RS., Lin MC., "Thermal decomposition of ethanol. I. Ab Initio molecular orbital/Rice–Ramsperger–Kassel–Marcus prediction of rate constant and product branching ratios," *Journal of Chemical Physics*, vol. 117, no. 7, p. 3224, 2002.

[145] Bufferand, H.; Tosatto, L.; La Mantia, B.; Smooke, M.D.; Gomez, A., "Experimental and computational study of methane counterflow diffusion flames perturbed by trace amounts of either jet fuels or a 6-component surrogate under non-sooting conditions," *Combustion and Flame,* vol. 156, no. 8, pp. 1594-1603, 2009.

[146] Sahu AB., Ravikrishna RV., "A detailed numerical study of NOx kinetics in low calorific value H2/CO syngas flames," *International Journal of Hydrogen Energy,* vol. 39, no. 30, pp. 17358-17370, 2014.

[147] Smooke MD., Puri IK., Seshadri K., "A comparison between numerical calculations and experimental measurements of the structure of a counterflow diffusion flame burning diluted methane in diluted air.," *International Symposium on Combustion,* vol. 2, no. 1, pp. 1783-1792, 1988.

[148] Bufferand H., Tosatto L., La Mantia B., Smooke MD., Gomez A., "Experimental and computational study of methane counterflow diffusion flames perturbed by trace amounts of either jet fuel or a 6-component surrogate under non-sooting conditions,"

Combustion and Flame, vol. 156, pp. 1594-1603, 2009.

[149] Weitz.E, "Transient Infrared Spectroscopy as a Probe of Coordinatively Unsaturated Metal Carbonyls in the gas phase," *Journal of Physical Chemistry,* vol. 98, pp. 11256-11264, 1994.

[150] Som S., Ramirez AI., Hagerdorn J.,Saveliev A., Aggarwal SK., "A numerical and experimental study of counterflow syngas flames at different pressures," *Fuel* , vol. 87, no. 3, pp. 319-334, 2008.

[151] Gerasimov IE.,Knyazkov DA., Shmakov AG., Paletsky AA.,Shvartsberg VM., Bolshova TA.,Korobeinichev OP., "Inhibition of hydrogen-oxygen flames by iron pentacarbonyl under atmospheric pressure," *Proceedings of Combustion Institute,* vol. 33, no. 2, pp. 2523-2529, 2011.

[152] Yetter RA., Risha GA., Son SF., "Metal particle combustion and nanotechnology," *Proceedings of Combustion Institute,* vol. 32, pp. 1819-38, 2009.

[153] Isaifan RJ., Ntais S., Baranova EA., "Particle size effect on catalytic activity of carbon-supported Pt nanoparticles for complete ethylene oxidation," *Applied Catalysis A:General,* Vols. 464-465, pp. 87-94, 2013.

[154] Bond GC., "The origin of particle size effects in heterogeneous catalysis," *Surface Science,* vol. 156, pp. 966-981, 1985.

[155] Keck, L., Spielvogel, J., Grimm, H., "From Nanoparticles to Large Aerosols: Ultrafast Measurement Methods for Size and Concentration.," *Nanosafe 2008: International Conference on Safe Production and use of Nanomaterials,* vol. 170, no. 1, 2009.

[156] Chowdhury S., Boyette WR., Roberts WL., "Time-averaged probability density functions of soot nanoparticles along the centerline of a piloted turbulent diffusion flame using a scanning mobility particle sizer," *Journal of Aerosol Science,* vol. 106, pp. 56-67, 2017.

[157] TSI Incorporated, "Aerosol statistics lognormal distribution and dN/d log Dp,"

Application Note PR-001, 2012.

[158] Hinds WC., Aerosol Technology: Properties, Behavior and measurement of airborne particles. Second edition, Wiley, 1999.

[159] Okyay G., Héripré E., Reiss T., Haghi-Ashtiani P.,Auger T.,Enguehard F., "Soot aggregate complex morphology: 3D geometry reconstruction by SEM tomography applied on soot issued from propane combustion," *Journal of Aerosol Sciences* , vol. 93, pp. 63-79, 2016.

[160] Raj A., Pan K., Qi H., Zhu H., Wen J.Z., Croiset E., "Effects of an Iron Pentacarbonyl Additive on Counterflow Natural Gas and Ethanol Flames," *Energy & Fuels*, vol. 29, no. 8, pp. 5361-5371, 2015.

[161] Mitchell P.,Frenklach M., "Monte Carlo simulation of soot aggregation with simultaneous surface growth-why primary particles appear spherical," in *Twenty seventh symposium on Combustion /The Combustion Institute*, 1998.

[162] Mitchell P. Frenklach M., *Phys. Rev. E.*, vol. 67, p. 61407, 2003.

[163] Yuan L., Li TX., Saito K., "Synthesis of multiwalled carbon nanotubes using methane/air diffusion flames," *Proceedings of Combustion Institute* , vol. 29, no. 1, pp. 1087-1092, 2002.

[164] Wang BY., Liu YX., Weng JJ., Glarborg P., Tian ZY., "New insights in low temperature oxidation of acetylene," *Proceedings of Combustion Institute*, vol. 36, no.1, pp. 355-363, 2017.

[165] Julien P., Whiteley S., Goroshin S., Soo MJ., "Flame structure and particle-combustion regimes in premixed methane–iron–air suspensions," *Proceedings of Combustion Institute*, vol. 35, pp. 2431-2438, 2015.

Appendix A

A. Numerical Modeling of the iron pentacarbonyl assisted counterflow methane diffusion flame

Mesh independence testing results are shown in Figure A-1. The mesh size is gradually decreased from Mesh A till Mesh D till the point where the change is result is insignificant with respect to the computation time. The details of meshes A-D are given in Table A-1. Mesh D, with the size of 2.645 x 10^{-4} m^2 along with 7147 cells, 7600 nodes and 14741 faces is incorporated in the developed model for prediction.

Table A-1: Description of various meshing parameters

	Cells	**Faces**	**Nodes**	**Minimum face area (m^2)**
Mesh A	5352	10232	6432	3.1 x 10^{-4}
Mesh B	6102	12195	6884	2.89 x 10^{-4}
Mesh C	6839	13364	7293	2.73 x 10^{-4}
Mesh D	7147	14741	7600	2.65 x 10^{-4}

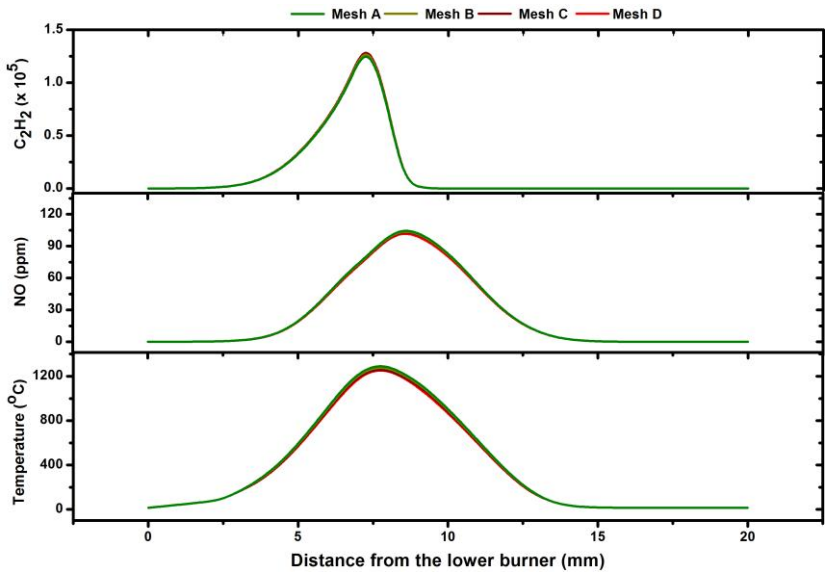

Figure A-1: Mesh independence details

Figure A-2 depicts the location of the stagnation plane under the non-catalytic and catalytic conditions as calculated from the numerical modeling results.

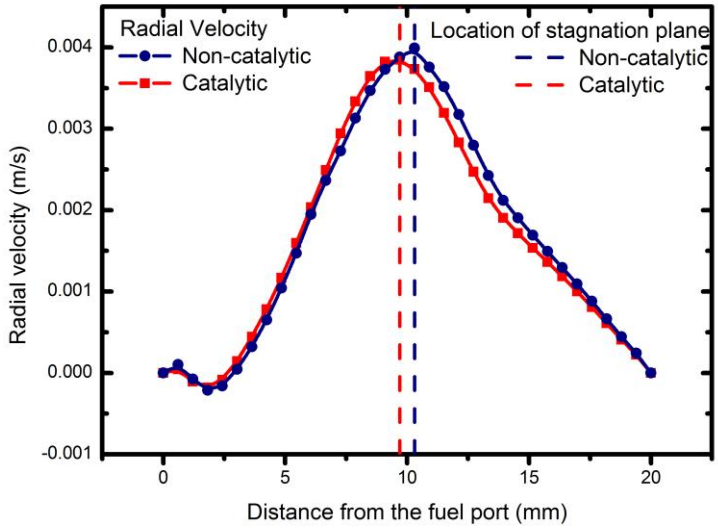

Figure A-2: Location of stagnation planes under non-catalytic and catalytic conditions

Parts (a)-(d) of Figure A-3 depict net reaction rates of key reactions contributing to evolution of C_2H_2, C_2H_2 and C_2H_6 and CO species under various methane fractions.

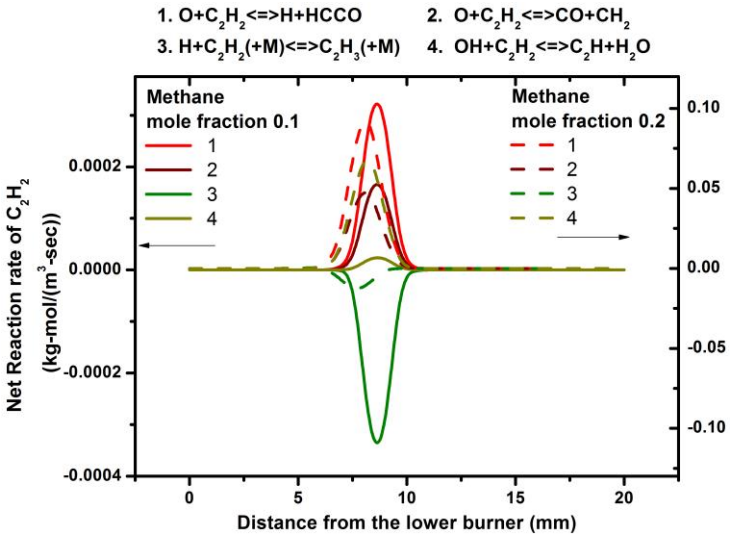

Figure A-3 (a): Reaction rates of key individual reactions affecting C_2H_2

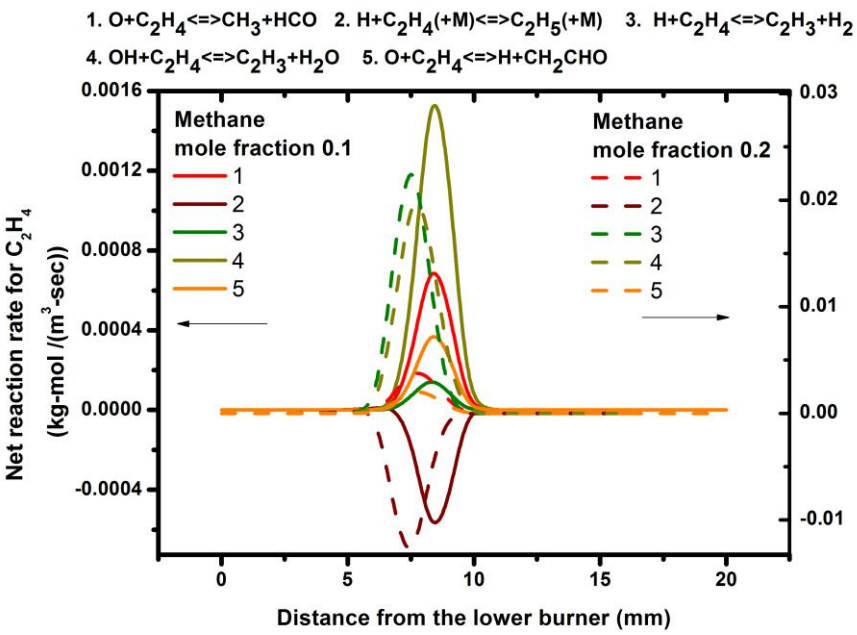

Figure A-3(b): Reaction rates of key individual reactions affecting C_2H_4

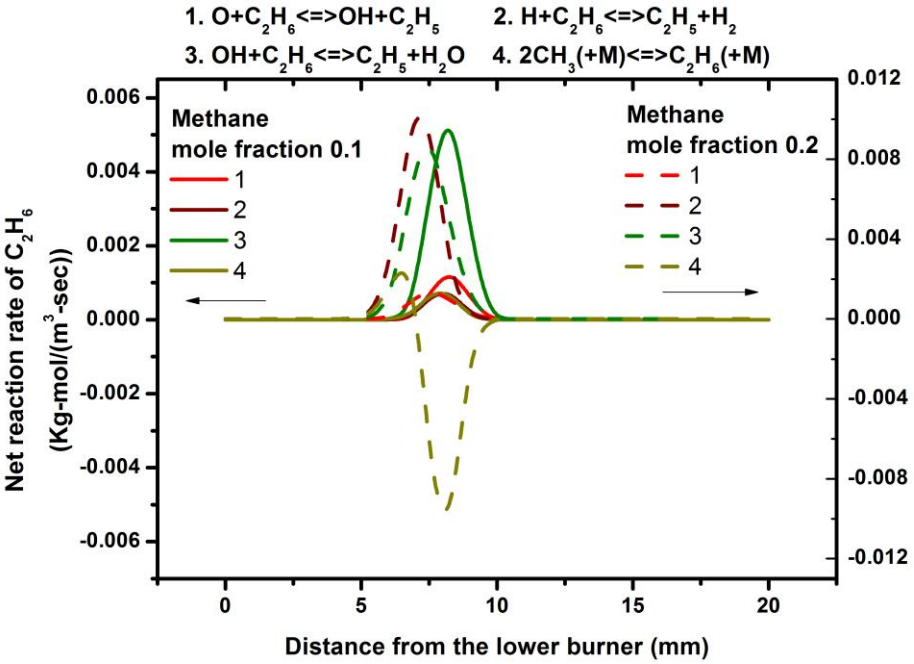

Figure A-3(c): Reaction rates of key individual reactions affecting C_2H_6

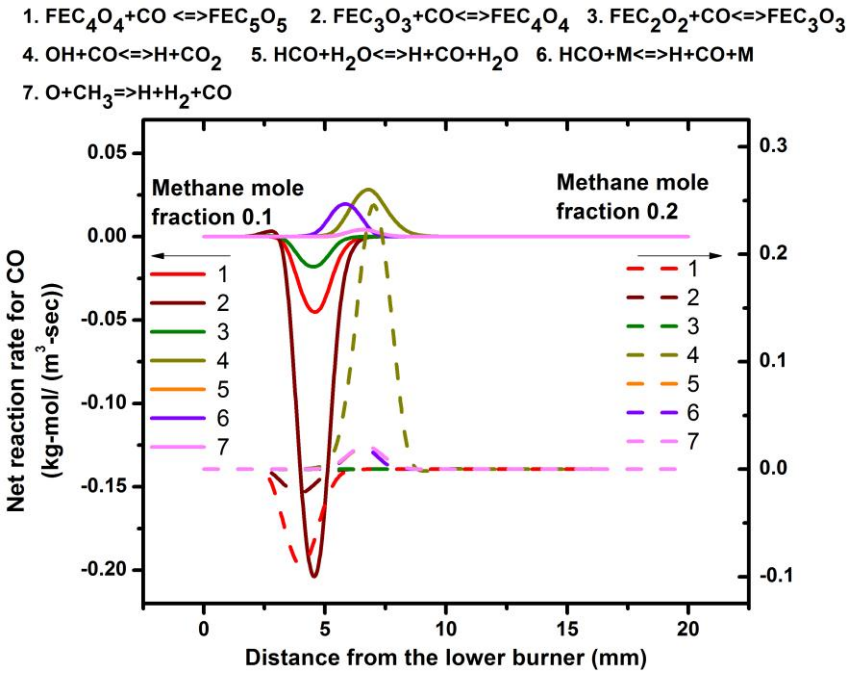

Figure A-3 (d): Reaction rates of key individual reactions affecting CO

Appendix B

1. Comparison of non-catalytic particle size and concentration using orifice diameters of 0.1 mm and 1 mm

At both radial locations, the particle concentration at orifice size of 0.5 mm is higher than that seen at the orifice size 1 mm between axial distances of 3-5 mm from fuel port. This is due to the fact that the concentric tube used solely for precursor injection lies at the centre (radial distance 0 mm) of the fuel port and no methane in injected through that tube during experimentation. Beyond that the difference between the values from the two different orifice sizes, shown in Figures B-1 and B-2, is not much significant.

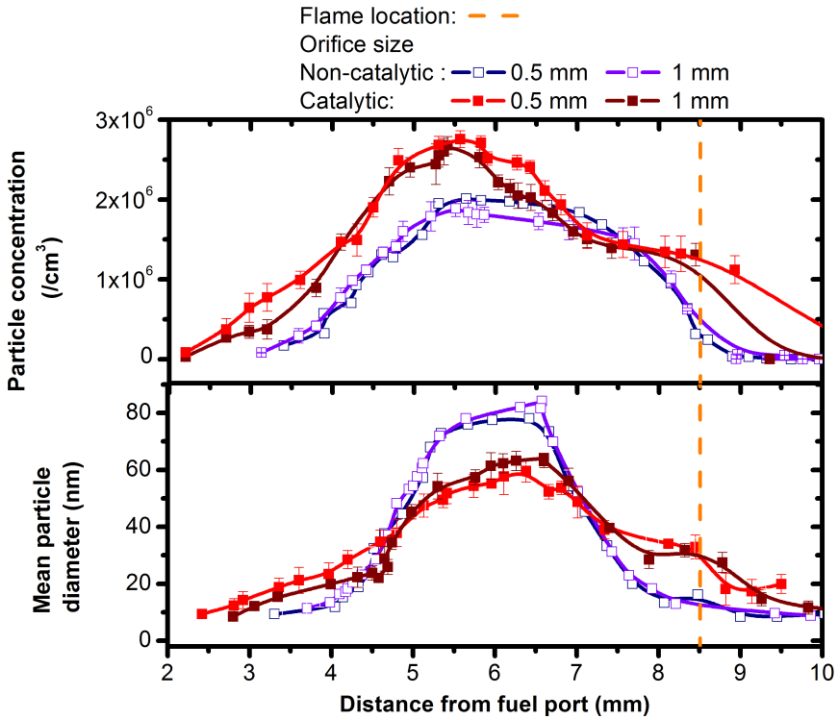

Figure B-1: Total particle concentration and geometric mean particle size at radial location of 0 mm under different orifice sizes

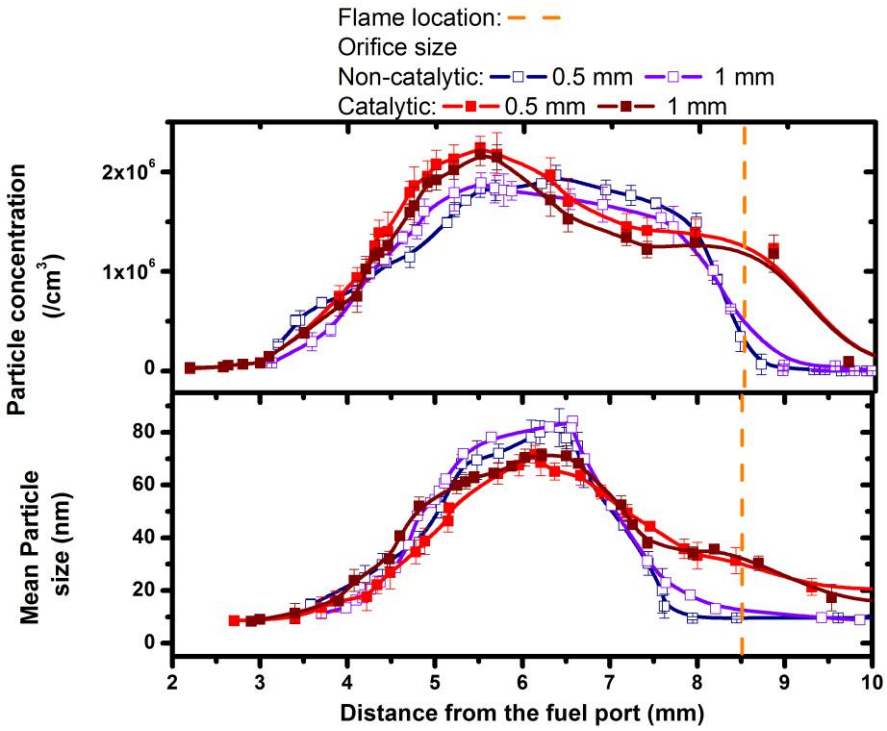

Figure B-2: Total particle concentration and geometric mean particle size at radial location of 5 mm under different orifice sizes

2. Particle sampling from iron pentacarbonyl assisted counterflow methane diffusion flame

Figure B-3 shows the SEM and EDAX images of the sample collected from the burner surface under catalytic conditions. Under the counterflow configuration, the highest radial velocity is located at the stagnant plane location as shown in Figure A-2 which is also close to the flame location. This causes most of the carbon content in the sample to get oxidized as seen from the elemental mapping results from EDAX in Figure B-3(b) which indicate the presence of unburnt carbon to an extent of only 10% of the whole sample.

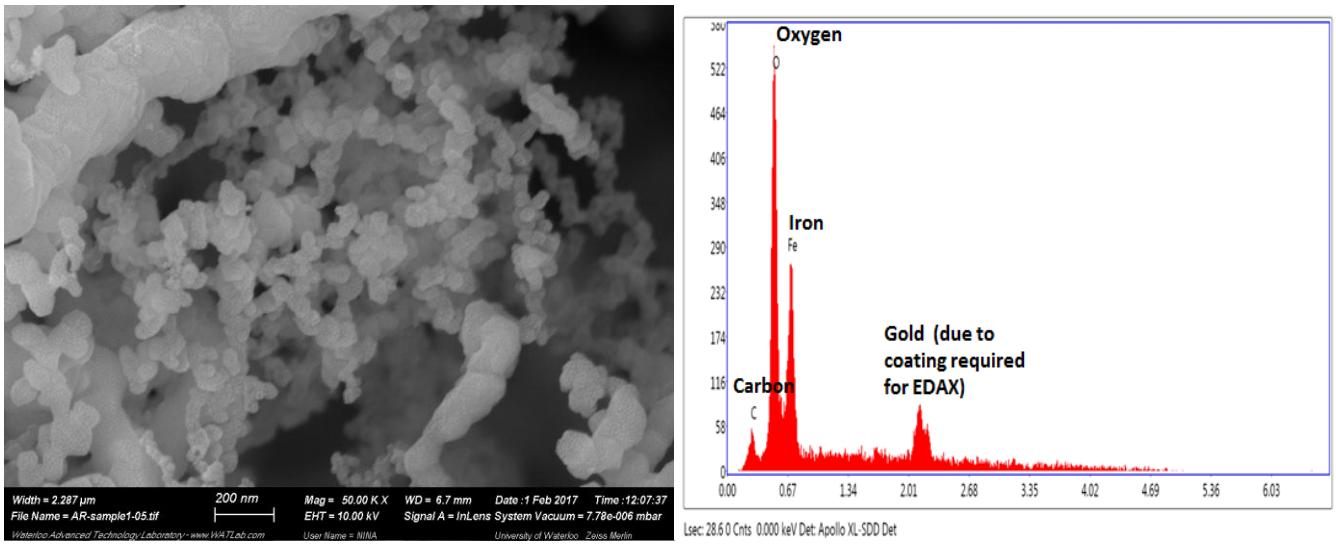

Figure B-3: (a) SEM images and; (b) EDAX signal of the collected particle sample